UNIVERSITÀ DEGLI STUDI DI PADOVA

UNIVERSITÀ DEGLI STUDI DI PADOVA
Centro di Ateneo di Studi e Attività Spaziali, CISAS "G. Colombo"

SCUOLA DI DOTTORATO DI RICERCA IN SCIENZE TECNOLOGIE E MISURE SPAZIALI
INDIRIZZO DI MISURE MECCANICHE PER L'INGEGNERIA E LO SPAZIO
CICLO XXVI

Numerical and Experimental Characterization of Throttleable Hybrid Propulsion Systems

*

Caratterizzazione Numerica e Sperimentale di Sistemi Propulsivi Ibridi a Spinta Variabile

Direttore della Scuola: Ch.mo Prof. Giampiero Naletto
Coordinatore d'indirizzo: Ch.mo Prof. Stefano Debei
Supervisore Ch.mo Prof. Daniele Pavarin
Co-supervisore Ph.D. Ing. Federico Moretto

Dottoranda: Martina Faenza

«Full many a gem of purest ray serene
The dark unfathom'd caves of ocean bear:
Full many a flower is born to blush unseen,
And waste its sweetness on the desert air.»

Elegy Written in a Country Churchyard
Thomas Gray

Abstract

The 1960s have been flourishing years for hybrid rocket propulsion: the thirst for knowledge pushed the engineers of those years to design and test any kind of motor configuration, and for several possible applications. Many projects of those years are fascinating and outstanding still nowadays.

The cold war era had extinguished any enthusiasm and interest for hybrids for years. It is approximately at the beginning of the '90s that a renew interest for hybrids has come alive, since, besides the pure performance, affordability and safety have become a must.

Hybrids are safe, simple, reliable, low cost and throttleable. All these characteristics make them suitable for several applications, not necessarily in replacement of solids and liquids, but possibly complementary. The TRL of hybrids has still to be improved in order to put hybrids on the market.

Among the aforementioned peculiarities of hybrids, their throttleability is the object of the present research.

This work is focused on the investigation of a high performing throttleable hybrid motor, conceived for soft-landing applications.
The main purpose of the research is to develop and characterize a motor in the 1kN-class, with characteristics like: high performance at different operative conditions, both in terms of regression rate and combustion efficiency enhancement, safety and simplicity, reliability.

The research is part of a wider framework: a EU FP7 granted project, called "SPARTAN", leaded by Thales Alenia Space, and aimed at developing a soft-lander demonstrator for planetary exploration, provided by a hybrid propulsion system. The University of Padova is partner of the project, so the preliminary design guidelines of the motor have been defined according to the requirements of the SPARTAN consortium.

The motor considered burns HTPB as fuel and 87.5%H2O2. High performance is expected to be achieved by means of vortex injection. The selection of H2O2 as oxidizer has been made to take advantage from its many qualities, like high density and high OF ratio, non-toxicity, possibility to decompose it through a catalyst. Thanks to this last aspect, fuel ignition is expected to be accomplished thanks to the hot gases resulting from oxidizer decomposition.

The doctoral research has been conducted combining several tools in synergy: analytic models, CFD simulations and experimental tests. The analytic models have supported the comprehension of the physical processes involved. The numerical simulations have been useful tools both to provide indications for final design purposes and to investigate in detail aspects of the internal ballistic of the motor, which were difficult to be observed in experimental tests. Finally, experimental tests have been conducted to validate the

numerical prediction and assess the achievement of the desired and expected results.

As a first step, once defined the preliminary design of the motor according to the SPARTAN requirements, a deep CFD investigation has been performed, in order to finalize the design. Chapter 2 describes this investigation.

Preliminary CFD simulations have been carried out on a motor configuration already developed and tested at UPD, in order to study and characterize the physics beyond vortex injection, and thus assess its effectiveness in enhancing the hybrid motor performance. The numerical results have been compared with an analytic model of the vortex flowfield. The outcome of this phase has been compared with the experimental data available.

In a second phase, the preliminary design produced within SPARTAN has been simulated to predict its performance and its sensitivity to some changes in the motor configuration and operative conditions. A prediction of the expected performance and some useful indications for the experimental tests are the main output of this second phase.

Then experimental tests of the motor have been performed to evaluate the actual performance at different throttling levels.

In order to overcome the issues related to handle and store hydrogen peroxide in high concentration, the design of the experimental test-bed foresaw the integration of the hybrid motor with a gas generator, responsible of reproducing 87.5% H2O2 in decomposed condition, as it would be passing through a catalyst. The mixture produced inside the gas generator is then injected as oxidizer into the combustion chamber of the hybrid motor. A description of the experimental test-bed is reported in chapter 3.

The experimental test-bed has been integrated and a preliminary phase of calibrations has been required to assess the correct functioning of the feed lines.

Moreover a complete diagnostic system has been defined and installed, in order to have a full and accurate monitoring of the interesting parameters. Chapter 4 describes the measurement system with its characteristic uncertainties.

Many tests have been performed at the beginning, to optimize the functioning of each subsystem composing the test-bed, and in order to obtain the correct oxidizer mixture and to assure HTPB ignition.

Finally, the hybrid motor has been successfully tested at three different fixed throttling levels: full thrust, 75% thrust and 50% thrust.

Fuel ignition has been achieved at each throttling level, and the dependency of the ignition delay from the throttling level has been considered.

The performance of the motor has been analyzed at each level, in terms of: resulting regression rate, as a function of the oxidizer flux; combustion efficiency; combustion stability. A comparison between the performance obtained at each level has been performed.

Any possible evidence of nozzle throat erosion has been monitored.

Finally, the results have been compared with the reference regression rate law, proper of 87.5%H2O2-HTPB, in order to demonstrate the effectiveness of the gas generator in simulating decomposed hydrogen peroxide in high concentration.

The actual mixture composition has also been estimated. Chapter 5 describes all the experimental tests performed, once the experimental test-bed has been properly set.

Sommario

Gli anni '60 sono stati eccezionalmente produttivi per la propulsione ibrida: la sete di conoscenza spinse gli ingegneri di quegli anni a progettare e testare le più disparate, per svariate possibili applicazioni. Molti progetti di allora sono considerati tuttoggi affascinanti e fuori dal comune.

L'era della guerra fredda ha assopito ogni entusiasmo e interesse per l'ibrido per molti anni.

Un rinnovato interesse si è manifestato all'inizio degli anni '90, quando accanto alla pura prestazione propulsiva, la convenienza economica e la sicurezza sono diventati elementi imprescindibili.

I motori ibridi sono sicuri, semplici, affidabili, a basso costo e modulabili in spinta. Tutte queste caratteristiche li rendono adatti a molteplici applicazioni, non necessariamente in contrasto con i motori solidi e liquidi, ma piuttosto ad essi compllementari. Il livello di sviluppo tecnologico dell'ibrido necessita ancora di un intenso miglioramento, affinchè l'ibrido possa essere competitivo sul mercato.

Tra le peculiarità appena citate, la modulabilità della spinta è stata oggetto di questa ricerca.

Il progetto è incentrato sull'investigazione di un motore ibrido ad alte prestazioni, concepito per applicazioni di esplorazione spaziale che richiedano atterraggio planetario controllato.

Il principale fine della ricerca è lo sviluppo e la caratterizzazione di un motore di classe 1 kN, con caratteristiche quali: elevate prestazioni in diverse condizioni operative, sia in termini di *regression rate* che di efficienza di combustione, sicurezza e semplicità, affidabilità.

La presente ricerca rientra in un contesto più ampio: il progetto europeo SPARTAN, coordinato da Thales Alenia Spazio, e volto allo sviluppo di un dimostratore tecnologico per atterraggio planetario controllato, dotato di un sistema propulsivo a razzo ibrido. L'Univeristà di Padova è partner del progetto; pertanto le linee guida del progetto preliminare sono state definite sulla base dei requisiti del progetto SPARTAN.

Il motore considerato utilizza HTPB come combustibile e 87.5%H2O2 come ossidante. Al fine di ottenere elevate prestazioni è stato adottata un'iniezione di tipo vortex. La scelta del'H2O2 come ossidante deriva dai sui vantaggi intrinseci: elevata densità, elevato rapporto OF, non tossicità, possibilità di decomporlo mediante un catalitico. Grazie a quest'ultimo aspetto, l'accensione del combustibile avviene grazie ai gas caldi derivanti dalla decomposizione dell'ossidante.

La ricerca di dottorato è stata condotta combinando in sinergia diversi strumenti stru-

menti: modelli analitici, simuazioni CFD e test sperimentali. I modelli analitici hanno favorito la comprensione dei processi fisici coinvolti. Le simulazioni numeriche hanno fornito sia utili indicazioni per il design finale del motore che informazioni dettagliate sulla balistica interna del motore, difficilmente osservabili dai test sperimentali. Infine, una campagna di test è stata svolta, allo scopo di validare i modelli numerici e verificare l'ottenimento delle prestazioni attese.

Come primo passo, una volta definito il design preliminare del motore, sulla base dei requisiti del progetto SPARTAN, è stata compiuta una dettagliata indagine numerica, allo scopo di finalizzare la progettazione. Il capitolo 2 descrive questa fase del progetto.

Simulazioni CFD preliminari sono state realizzate, considerando una configurazione di motore già sviluppata e testata presso l'Università di Padova; il fine è stato quello di investigare la fisica di base dell'iniezione vortex, per verificare l'efficacia di questa tecnologia nell'incrementare le prestazioni di un motore ibrido. I risultati numerici sono stati confrontati con una modellazione analitica e con i dati sperimentali disponibili.

In una seconda fase, la configurazione preliminare del motore identificato nell'ambito del progetto SPARTAN è stata simulata, per prevederne le prestazioni e determinare la sensibilità del funzionamento del motore a cambiamenti sia di geometria che di condizioni operative.

Successivamente, le effettive prestazioni del motore sono state caratterizzate per mezzo di test sperimentali a diversi livelli di spinta.

Al fine di ovviare alle problematiche di gestione e immagazzinamento dell'acqua ossigenata ad alta concentrazione, il design dell'esperimento ha previsto l'integrazione del motore ibrido con un *gas generator*, responsabile di riprodurre H2O2 all'87.5% decomposta, come se derivasse da un catalitico. La miscela di gas prodotta nel *gas generator* viene dunque iniettata come ossidante nella camera di combustione del motore. L'apparato sperimentale viene descritto nel capitolo 3.

L'intero apparato sperimentale è stato integrato e le linee idrauliche sono state calibrate.

Inoltre è stato definito un apparato diagnostico completo, allo scopo di monitorare in maniera completa e accurata i parametri di interesse. Il capitolo 4 descrive il sistema di misura con le relative incertezze.

Numerosi test preliminari sono stati necessari, per mettere a punto ogni sottosistema e ottenere la corretta miscela ossidante, che assicuri l'accensione dell'HTPB.

Infine il motore ibrido è stato testato con successo a tre livelli di spinta: spinta nominale, 75% della spinta nominale, 50% della spinta nominale.

L'accensione dell'HTPB è stata ottenuta ad ogni livello di spinta ed è stata valutata la dipendenza del ritardo di accensione dal livello di spinta considerato.

Le prestazioni del motore sono state analizzate ad ogni livello, in termini di *regression rate* in funzione del flusso di ossidante, di efficienza di combustione e di stabilità della combustione. I risultati ottenuti a ciascun livello sono stati confrontati tra loro.

Qualsiasi possibile insorgenza di erosione della gola dell'ugello è stata monitorata.

Un confronto finale è stato fatto tra i risultati sperimentali e la legge del *regression rate* di riferimento, propria di 87.5%H2O2-HTPB, con lo scopo di dimostrare l'efficacia del *gas generatore* nel simulare acqua ossigenata decomposta ad alta concentrazione.

L'effettiva composizione della miscela ossidante è stata infine stimata. Il capitolo 5 descrive tutta la campagna di test condotta.

Contents

List of Figures

List of Tables

Nomenclature

ΔM_{fuel}	Burned fuel mass
$\dot{m}_{fuel}$	Fuel mass flow rate
$\dot{m}_{ox}$	Oxidizer mass flow rate
$\dot{r}$	Regression rate
ϵ	Seebeck coefficient
η	Combustion efficiency
ω	Angular velocity
ϕ_{th}	Nozzle throat diameter
ρ	Density
A_{burn}	Burning area
A_p	Grain port section
A_{th}, A_{so}, A_{cv}	Nozzle throat section
C_d	Discharge coefficient
D_p	Grain port diameter
$e.m.f.$	Electromotive field
f_s	Sampling frequency
f_{Ny}	Nyquist frequency
L_{grain}	Grain length
M_m	Molar mass
p_0	Total pressure
p_i	Inlet/upstream pressure
p_c	Combustion chamber pressure

p_{sat}	Vapor pressure
R_0	Resistance at temperature 0 °C
R_g	Real gas constant
R_t	Resistance at temperature t
R_u	Universal gas constant
SN_g	Geometrical Swirl Number
T	Temperature
T_0	Total temperature
t_b	Burning time
G_{ox}	Oxidizer specific mass flow rate
a, n	Regression rate law coefficients
c	Specific heat capacity
k	Heat capacity ratio
m	Mass
p	Pressure
q	Thermal flux
R	Thermal resistance
SN	Swirl Number
t	Time
CAD	Computer Aided Design
CC	Combustion Chamber
CEA	Chemical Equilibrium with Applications, thermo-chemical software by NASA
CFD	Computational Fluid Dynamics
EDM	Electric discharge machining
GG	Gas Generator
GOX	Gaseous OXygen
GOX	Gaseous oxygen
HDPE	High Density PolyEthylene

HP Hydrogen Peroxide

HT Hybrid Torch

RTD Resistance thermometer

UPD University of Padova

Chapter 1

Research Background

1.1 Hybrid Propellant Rockets Overview

As far as rocket propulsion is concerned, several categories of engines can be identified, basically distinguished by the technique they adopted to produce energy; in this perspective, the main categories are:

- chemical;
- nuclear;
- electric.

Each category has its own main features, which make it suitable for specific application; for example: booster stage, sustainer, attitude control, orbit station keeping.

Typical values of representative performance parameters for different types of rocket propulsion are shown in figure 1.1 and 1.2. [1]

Chemical rockets have relatively low values of specific impulse, relatively light machinery (i.e., low engine weight), a very high thrust capability, and therefore high acceleration and high specific power. At the other extreme, the ion propulsion devices have a very high specific impulse, but they must carry a heavy electrical power source with them to deliver the power necessary for high ejection velocities. The very low acceleration potential for the electrical propulsion units and those using solar radiation energy usually requires a long period for accelerating and thus these systems are best used for missions where the flight time is long. The low thrust values of electrical systems imply that they are not useful in fields of strong gravitational gradients (for takeoff or landing) but are best used in a true space flight mission [1].

As far as the chemical rockets are concerned, a high-pressure combustion reaction involves the propellant chemicals, usually a fuel and an oxidizing chemical; thus a high temperature mixture (2500 to 4100 °C) is produced, and its thermal energy is converted to kinetic energy through an expansion nozzle.

Three main types of rockets can be identified, which are basically distinguished by the phase, which the propellants are stored in:

1. liquid: both the oxidizer and the liquid are stored in liquid phase, in separated tanks, from which they are fed to the combustion chamber;

Engine Type	Specific Impulse[a] (sec)	Maximum Temperature (°C)	Thrust-to-Weight Ratio[b]	Propulsion Duration	Specific Power[c] (kW/kg)	Typical Working Fluid	Status of Technology
Chemical—solid or liquid bipropellant	200–410	2500–4100	10^{-2}–100	Seconds to a few minutes	10^{-1}–10^{3}	Liquid or solid propellants	Flight proven
Liquid monopropellant	180–223	600–800	10^{-1}–10^{-2}	Seconds to minutes	0.02–200	N_2H_4	Flight proven
Nuclear fission	500–860	2700	10^{-2}–30	Seconds to minutes	10^{-1}–10^{3}	H_2	Development was stopped
Resistojet	150–300	2900	10^{-2}–10^{-4}	Days	10^{-3}–10^{-1}	H_2, N_2H_4	Flight proven
Arc heating—electrothermal	280–1200	20,000	10^{-4}–10^{-2}	Days	10^{-3}–1	N_2H_4,H_2,NH_3	Flight proven
Electromagnetic including Pulsed Plasma (PP)	700–2500	—	10^{-6}–10^{-4}	Weeks	10^{-3}–1	H_2 Solid for PP	Flight proven
Hall effect	1000–1700	—	10^{-4}	Weeks	10^{-1}–5×10^{-1}	Xe	Flight proven
Ion—electrostatic	1200–5000	—	10^{-6}–10^{-4}	Months	10^{-3}–1	Xe	Several have flown
Solar heating	400–700	1300	10^{-3}–10^{-2}	Days	10^{-2}–1	H_2	In development

[a]At $p_1 = 1000$ psia and optimum gas expansion at sea level ($Ip_2 = p_3 = 14.7$ psia).
[b]Ratio of thrust force to full propulsion system sea level weight (with propellants, but without payload).
[c]Kinetic power per unit exhaust mass flow.

Figure 1.1: Ranges of typical performance parameters for various rocket propulsion systems

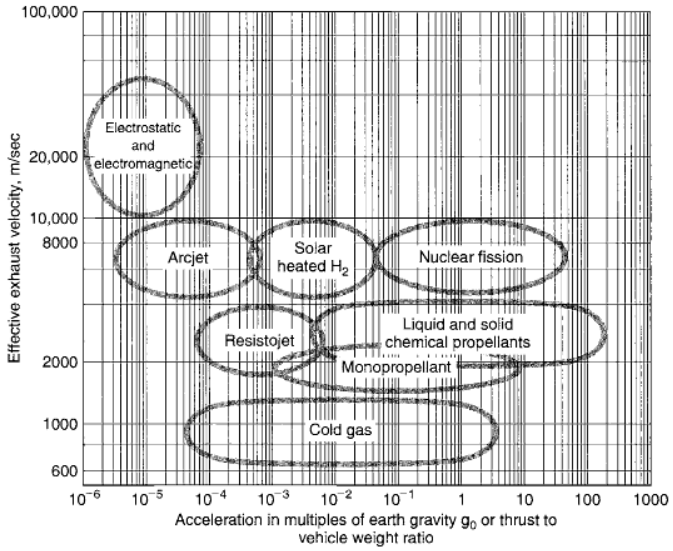

Figure 1.2: Exhaust velocities as a function of typical vehicle accelerations. Regions indicate approximate performance values for different types of propulsion systems. The mass of the vehicle includes the propulsion system, but the payload is assumed to be zero

2. solid: oxidizer and fuel are already mixed together in a solid matrix, which is stored directly in the combustion chamber; the solid propellant charge, called grain, contains all the chemical elements for a complete burning;

3. hybrid: oxidizer and fuel are stored in different phases, usually the oxidizer is liquid and the fuel is solid; the solid propellant is stored directly in the combustion chamber, while the liquid one in a separate tank.

The previous description represents a baseline; some specific variation can be identified: jellified propellants or premixed liquid decomposed through a catalyst or gaseous oxidizers,

to make some examples.

The advantages and disadvantages of each one of the listed types are a direct consequence of the storing and feeding method they require.

Figure 1.3 reports schematic representations of these categories.

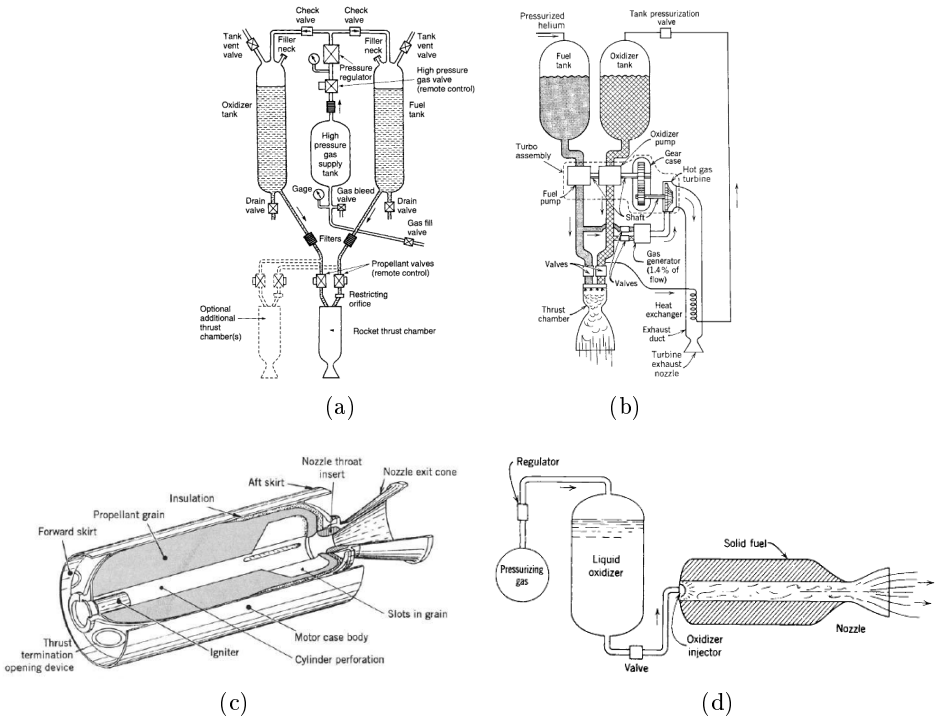

Figure 1.3: Schematics of the main types of chemical rocket systems: pressure fed liquid rocket (a), liquid rocket with a turbopump feed system (b), solid rocket (c), hybrid rocket (d)

The strongest effort in developing chemical propulsion has been made in the 1950s and 1970s: basically, every new concept had been designed and tested. After an initial assessment only the most promising technology had been chosen for extensive further work. Hybrids were excluded from this selection, because seemed to be less promising than the other two categories, and, moreover, presented some issues not solved.

Solid rocket are very simple, ready to launch and could reach the highest value of impulse density, making them ideal for volume constrained applications such as military weapons, sounding rockets and boosters.

Liquids can reach the highest specific impulse; they can be stopped and started multiple times in flight, making them ideal for launchers and spacecraft.

Hybrids had been considered an intermediate case between the two, so not showing a clear advantage respect to both extremes in a performances oriented environment.

Hybrids maturity still suffer nowadays for the choices of those years; but some of their peculiarities are becoming appreciated, in the perspective of a safe, reliable, low cost, and environmentally friendly propulsion system.

The combustion process of a hybrid motor is strongly different from that of solids and liquids.
In solids, oxidizer and fuel are intimately mixed together, in the respective quantities required to work at the desired and fixed OF ratio: in the pyrolysis process, the quantity of each reactant respect to the total mass produced, is a predetermined and prefixed quantity. The total amount of mass flow rate produced depends uniquely on the linear regression of the grain surface, which in turns depends on the operative combustion chamber pressure. The flame in solids is very thin and close to the grain surface (i.e. in the order of few μm).
In liquids, the oxidizer and fuel mass flow rate are controlled by separated feed lines, and thus the OF ratio can be controlled almost perfectly. The reactants are intimately mixed in the vicinity of the injector to form a combustible mixture.
In hybrids, just the oxidizer mass flow rate is directly controlled, while the fuel mass flow rate directly depends on the regression of the grain surface, which in turn depends on the convective heat transfer from the flame to the surface; thus the total mass flow rate and the OF ratio are correlated. The OF ratio is not constant in hybrids, nor spatially (it changes along the grain) neither in time (it changes during the burning time). Moreover, since the reactants are injected from different sides, the combustion process depends on their reciprocal diffusion and mixing; as a consequence, hybrids are characterized by a diffusion flame.

Hybrids present several *advantages*, in comparison with the other two categories. Hereafter a brief description is provided.

- *Safety.* The fuel is inert, so it can be manufactured, transported and handle as a standard commercial product. Oxidizer and fuel are stored separately, so an accidental ignition of the engine is not possible. The burning can be aborted at any time, just shutting down the oxidizer valve. Fuel cracks are not catastrophic: combustion takes place just if the fuel encounters the oxidizer flow. Moreover, hybrid combustion is usually not pressure sensitive, since it is diffusion controlled. So in general, hybrid failures are usually benign in nature.

- *Reliability.* An hybrid rocket requires roughly only half of the components of a liquid engine. Respect to solids the grain is much more insensitive to defects.

- *Mass flow control.* Oxidizer can be modulated, in order to throttle the thrust produced, and the total mass flow rate changes accordingly. If a suitable ignition system is foreseen, the engine can be multiply started and stopped.

- *Propellant versatility.* The selection of propellants is much greater than with either solids or liquids even if the great part of the attention has been focused on a narrower band of combinations.

- *Temperature insensitivity.* The temperature effect on the burning rate is small (as in liquids), thues ambient launch temperature variations have little effect on operating chamber pressure.

- *Specific impulse.* Hybrids have specific impulses that are higher than solids and comparable with solids, if the cryogenic category is excluded (see figure 1.4). The density impulse is lower than solids but nominally higher than liquids.

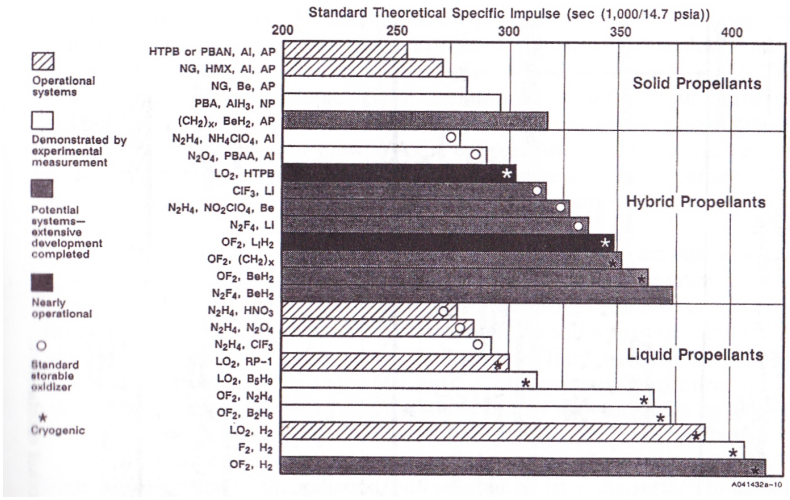

Figure 1.4: Theoretical specific impulse for chemical rocket systems

- *Low cost.* In terms of cost of components, hybrids are placed between the more complex and more expensive liquids, and the simpler and cheaper solids. But in addition, hybrids benefit of lower operational costs, since they take the advantage of their intrinsic safety.

- *Environmental friendliness.*

It has to be said that often these advantages tend to be counteracting, and so it is hard to satisfy most of them all together. On the other hand, hybrid rockets present also some *disadvantages*; the main are highlighted in the following.

- *Low regression rate.* With a low regression rate, a large burning area is required to produce the desired thrust; this in turn means lengthening the fuel grain or using a multiport grain. The latter solution has its own problems: high residuals, no uniformity of regression rate between the ports, port shape change during the burn, to make some examples. Moreover, the required web thickness is small, causing a poor volume loading of the combustion chamber. The problem is increased with scale-up.

- *Combustion efficiency.* Combustion in hybrids tends to be rougher and less complete, thus penalizing the achieved specific impulse, respect to the theoretical value.

- *OF shift.* OF ratio changes over time; in general a hybrid motor does not work always at the ideal OF ratio.

- *Packaging issues.* The liquid oxidizer can be easily packaged, shaping and locating opportunely the tank, but the combustion chamber shape is constrained by the fuel grain envelope. The geometry of the grain cannot be changed freely, since its shape strongly influence the combustion process.

- *Slower transients.* Ignition transients are usually slower for hybrids. And the response to throttling is slower too. this prevent the adoption of hybrid systems, when very accurate, repeatable and fast response is needed.

It is worth noting that some hybrid characteristics like safety and simplicity could lead indirectly to a performance advantage. For example a safe and simple propulsion system has more chances to exploit the advantages of air launch. Moreover a simpler, safer, cheaper system can be tested much more times in a smaller timeframe. This in turn allows the possibility to continuously upgrade, optimize and improve the system with new state of art technology. This fact is particularly significant during period of low investments like the current one [2].

1.1.1 Hybrids Fundamentals

In a typical hybrid rocket the oxidizer enters the combustion chamber from the head end and flows over the solid surface. After motor ignition, the combustion is self-sustained by the continuous pyrolysis of fuel due to flame, which heats up the fuel surface. Vaporized fuel and gaseous oxidizer encounter each other and react inside the boundary layer. In the boundary layer large gradients of the fluid variables occur.

It is possible to demonstrate that in a laminar boundary layer when the reaction rate approach an infinite value the flame thickness goes to zero and the flame occurs where the concentration corresponds to stoichiometric conditions. Mathematically it is possible to approximate the flame as a line where the reagents concentration goes to zero. This is the so called flame-sheet approximation. In a turbulent boundary layer the physics is more complex because of the local time and spatial fluctuations. However the flame-sheet hypothesis is considered a first acceptable approximation [2].

In hybrid rockets, typically, the chemical reaction rate is much faster than the diffusion rate of the reactants toward the flame; this means that the Damkohler number, $Da = \tau_c/\tau_k$, that is the ratio between the fluid dynamics time scale, τ_c, and the chemical reactions time scale, τ_k, is far greater than 1. Thus, it can be concluded that the hybrids combustion is diffusion limited, and so the chemical kinetics can be neglected, considering the chemical reactions to happen at infinite rate.

The basic fundamentals of hybrid physics were formulated in the '60s. In that period much work was done in the US, testing several propellants in many different conditions and configurations.

The first basis understood for hybrids is the fundamental correlation between fuel regression rate, $\dot{r}$, and oxidizer flux, G_{ox}, found experimentally considering spatial and temporal averaged regression rates:

$$\dot{r} = a\, G_{ox}^{n}\, L^{m} \tag{1.1}$$

where L represents the length, while a, n and m are empiric coefficients.

Usually the dependence from the length is incorporated in the a coefficient, since a single scale of motor is tested.

Moreover, Marxman and his coworkers developed the regression rate model, which describes the relation between regression rate and convective heat flux provided to the fuel surface by the turbulent diffusion flame. The result of the model was an equation for

the regression rate having the same structure of the experimentally developed correlations, confirming the understanding of the basic hybrid physics. The main outcomes of this correlation are summarized hereafter [2], [3].

- The regression rate depends on the local mass flux, and this tends to self-compensate grain consumption nonuniformities.
- A blocking effect characterizes hybrids combustion: the fuel regression produces pyrolyzed gases which blow from the surface towards the flame, pushing it aside from the fuel grain; as soon as the flame moves away from the fuel surface, the heat flux provided decreases, thus decreasing the fuel pyrolyzed, and then the blowing effect. These two counteracting effects, fuel blowing and oxidizer flux, reach an equilibrium finally, and here the location of the flame stabilizes.
- Regression rate varies along the grain length, because of two counteracting effects: the local increasing of mass flux due to fuel addition, and the boundary layer thickening.
- Regression rate is scale dependent: it decreases for larger motors, since the flame tends to settle farther from the grain surface.
- At low values of the oxidizer flux, the convective heat flux is small so the radiative term is no longer negligible compared to it (see figure 1.5). The radiation contribution tends to increase the total wall heat flux; its contribution is produced by soot made by incomplete burning of hydrocarbon, metal or other particles liberated from the pyrolysis of the solid fuel. Radiation contribution increases at higher pressures, because the emissivity of the gas phase increases.
- At very high oxidizer fluxes, the residence time becomes small and thus the chemical kinetics becomes no negligible (see figure 1.5). The chemical reaction rate increases with pressure.
- The fuel mass flow is proportional to both the regression rate and the burning area so the final fuel production would depend on the balance between the two. If the flux exponent, n, is 0.5 no O/F shift occurs: this happens because the reduction of regression rate is perfectly balanced by the increase of the burning area. For $n > 0.5$ the reduction of regression rate is larger, so the fuel mass flow, chamber pressure and motor thrust decrease with time. For $n < 0.5$ the regression rate variation is more flat so the increase of burning area prevails. Consequently the fuel mass flow, chamber pressure and motor thrust increase with time. Figure 1.6a shows what already described.
- The O/F ratio is dependent on the oxidizer mass flow with the $1 - n$ power. As expected for $n = 1$ no O/F shift occurs. In fact $n = 1$ represents a linear variation of the fuel flow with the oxidizer flow, that in turn produces an exact self-adjusting behavior. Typically, experimental values of n are found to be lower than 0.8: this means that the fuel rate variation as a function of oxidizer rate is sublinear, so the variation is lower than desired. Thus O/F shift occurs (see figure 1.6b). To limit it, in this case a with a high flux exponent is preferable, but this is in contrast with the

need for $n = 0.5$ to limit the O/F variation with time. A trade-off between the two is needed.

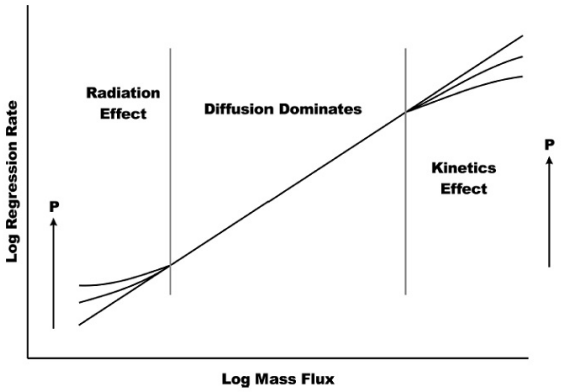

Figure 1.5: Typical regimes of functioning of an hybrid

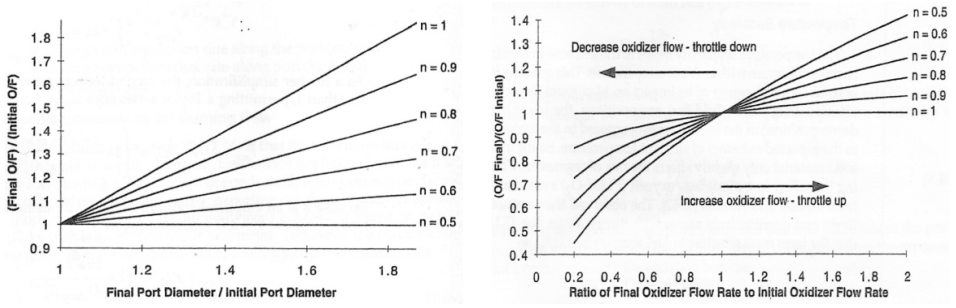

(a) (b)

Figure 1.6: OF shift in hybrids for different flux exponents as a function of port diameter(a), and throttling (b)

1.2 EU FP7 SPARTAN Project

The present research is part of a wider framework: a European Union project called "SPARTAN", funded in the 7th framework program (FP7-SPACE-2010-1), under grant agreement nÂ° 262837.

SPARTAN is a 3 years project, started in March 2011 and expected to be concluded in July 2014.

An international consortium is involved in this project (figure 1.7). The University of Padova is a partner.

The SPARTAN program ("SPAce exploration Research for Throttleable Advanced eNgine") is focused on developing a soft-landing demonstrator for space exploration. The innovation in this research program consists in the adopted propulsion system: the lander

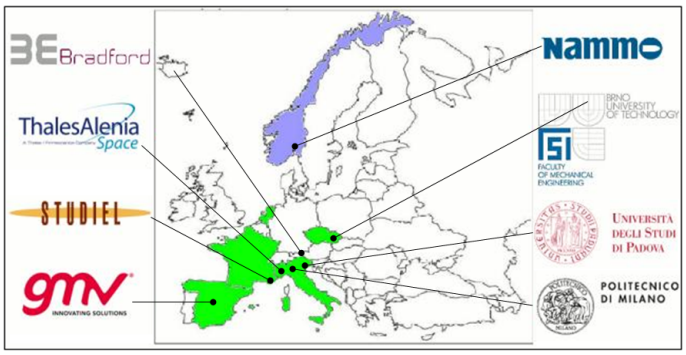

Figure 1.7: EU FP7 SPARTAN project: consortium members

will be provided by four highly throttleable (10:1) hybrid motors with 1,5 kN nominal thrust each [4].

The Nammo Raufoss company is responsible for developing and testing the engine for the flight prototype. It is a Norwegian/Finnish military industry manufacturer of ammunition, which has since 2004 invested and actively worked on the development of hybrid rocket propulsion systems.

The choice of hybrid motors is due to its intrinsic advantages, which fit well with the application considered: simplicity, reliability, safety, low cost, throttleability. Most of all, the latter represents a key feature.

Low combustion efficiency and regression rate have been two major drawbacks for years, but studies conducted in the last five years by several research groups have clearly affirmed the effectiveness of two main strategies to mitigate these aspects: vortex injection [5], [6], [7], [8] and turbulence-enhancement devices [9], [10]. Up to now, both these solutions have been tested at lab-scale (1 to 3 kN), but they could possibly represent a promising solution at larger scale, even because they allow a significant compactness of the overall dimension of the combustion chamber. In fact the use of post-combustion chambers is unneeded when vortex injection or diaphragms are adopted; moreover their installation inside the combustion chamber essentially does not require additional space respect to a more "standard" motor configuration.

The hybrid rocket motor selected for SPARTAN burns 87.5% H2O2 as oxidizer and HTPB/C as fuel and it is based on vortex injection. Motor ignition is accomplished thanks to H2O2 decomposition through a catalyst.
The selection of H2O2 as oxidizer has been made to take advantage from its many qualities, as the high density and high OF ratio, which keeps down the combustion chamber overall dimension. Furthermore it is considered to be a “green” and non-toxic substance, so development and testing costs are reduced. The possibility to decompose it through a catalyst makes ignition and eventual re-ignition feasible without any specific sub-system for that purpose. HP in high concentration has a typical vacuum Isp competitive with LOX and N2O. But, respect to LOX, it is a storable propellant, which requires less complexity of the feeding system and thus an overall diminishing of the bulk density. Respect to N2O, it can be pressurized to lower levels, and so volumes and weight are reduced.
On the other hand, hydrogen peroxide involves also some hazards for its handling, storage

and management; this is due to its corrosive capability, reactivity and instability at high concentration.

In the framework of the SPARTAN program, UPD is responsible of customizing a CFD tool to accurately simulate the hybrid motor functioning, thus supporting design and testing phases. Numerous studies have demonstrated the effectiveness of CFD tools in helping the physical understanding of the flow field behavior inside the combustion chamber [7], [10], [11], [12].

A forward step for UPD in numerical modeling of hybrid combustion consists in self-evaluating fuel regression rate as a function of wall heat flux [13], since, currently, regression rate represents a significant unknown variable in the motor operation until the motor is tested.

In order to validate numerical results, UPD developed its own engine to perform its own ground tests, and thus provide experimental data for numerical results validation. A complete and dedicated experimental setup has been designed, set up and calibrated to provide an effective instrument for validation of the CFD code and support to the final motor design.
Respect to the SPARTAN flight prototype, the UPD motor had to be representative in a series of aspects:

- thrust scale;
- possibility to work at different throttling levels;
- injection technology: fully tangential vortex;
- propellants selected: 87.5% H2O2 as oxidizer and HTPB as fuel;
- oxidizer phase at the injector: gaseous;
- grain sizes: initial port diameter and length;
- nominal OF ratio at full thrust.

UPD has overcome the issues related to handling and storing high concentration hydrogen peroxide integrating the main hybrid motor with a dedicated gas generator, to reproduce 87.5% H2O2 in dissociated condition. The mixture produced inside the gas generator is then injected as oxidizer into the combustion chamber of the hybrid motor.

Gas generators have been being used for many years in several space application and not only (i.e. airbags actuation). As far as the space applications are concerned, gas generators are commonly used as source of hot gas to power turbo-pumps in liquid rocket engines[1]. In general they are used wherever a large amount of thermal power is needed for a relatively short time, and storing it as a pressurized gas is undesirable or impractical. They are simpler and lighter than conventional short-duration power equipment. Typical applications are gas generators for driving torpedo turbines and gas generators for actuating airplane catapults. In a staged combustion cycle all of one propellant and a small portion of the other propellant (either fuel-rich or oxidizer-rich mixture) are burned to create the turbine drive gases. Gas generators can be also used for powering of auxiliary power units and emergency power units [1].

In the following sections a brief literature survey is reported about three main feature characterizing the hybrid motor tested in the present research:

1. hydrogen peroxide, as oxidizer for hybrid rockets;
2. vortex injection, as a performance enhancer in hybrids;
3. throttling in hybrids.

1.2.1 Hydrogen Peroxide as Oxidizer for Hybrids

HP is currently available in concentration up to 90%, 98%, which are suitable for rockets applications. The interest in low toxicity propellants has led to an increased interest in this oxidizer [14].

In many military and space applications, oxidizer storability is desired, if not required, under mission constraints. Thus efforts dating back over the past 40 years have included study of hybrid rocket using storable oxidizers, such HP.

The first use of hydrogen peroxide for hybrid motors is dated mid 1950s: two major research groups tested hydrogen peroxide with polyethylene; the first is from ONERA (France) and the second is from General Electric (USA).

Pugibet and Moutet from ONERA [15] injected HP in liquid phase into the combustion chamber, assuring motor ignition by means of hypergolic reactions. They investigated several compounds, finding potassium borohydride to be the best solution in term of ignition delay (2 ms). They tested several compounds as fuels to be combined with HP, comparing the resulting regression rate. They finally proposed carboxyl-polybutadiene as a particularly suitable fuel to be burned with HP. The tests were performed on two different micro-thrusters, for a resulting operative pressure of 10 to 28 bar and a total mass flux from 40 to 90 kg/m2/s.

Moore and other colleagues from General Electric tested 90% H2O2 with polyethylene [16]. Moore and Berman described their motor as an augmented hydrogen peroxide monopropellant thruster because it had very high oxidizer to fuel (o/f) ratios. During preliminary testing they noted that performance increased as more of the polyethylene fuel was added and the thruster became more of a true hybrid rocket by the end of the study [16]. They tested a motor with operative pressure between 24 and 40 bar, and with typical total mass flux between 230 and 700 kg/m2/s. Moore proposed the decomposition of H2O2 through a silver-based catalyst. An optimal OF ratio equal to 7 was suggested and a temperature of HP decomposition of 700 °C was expected. Moore patented his propellant system in 1957, with his colleague Cooper [18].

Although these first investigations provided successful results, the interest for HP as oxidizer grew dim, because the cold war era imposed other priorities: basically the research for more energetic propellants. Thus essentially no published work exists for a three decade period beginning at the end of the 1960s. Current requirements for lower costs and nontoxic propulsion systems have renewed interest for H2O2 [14].

Starting from the end of 1990s, in fact, several companies or research groups are demonstrating a renewed interest for HP. The academic work is basically in the scale of small-hybrids (up to 4 kN).

To make an example, Purdue University is testing intensively the use of 90% hydrogen peroxide, with many different fuels [14]: PE-based fuels, HTPB, and DCPD (dicyclopentadiene) even with metallic additives. Moreover, in 2004 the Purdue Hybrid Rocket Project was initiated by a group of graduate and undergraduate students in the School of Aeronautics and Astronautics in order to develop a sounding rocket. The first generation of these sounding rockets had flown successfully in 2009 to an altitude of 2000 m, with an average thrust of 3000 N and a burning time of 6 seconds [19]. A new generation is under development, with a design thrust of 3600 N and a burning time of 13 seconds.

Many other examples can be found of research groups using HP as oxidizer for hybrids. To mention some more examples, at ONERA a lab scale motor based on 85% hydrogen peroxide is used to study pyrolysis phenomena of PE, HTPB and GAP [20]; at Beijing University a lab scale motor burning 90%H2O2-HTPB has been tested, to provide experimental data for the self-consistent calculation of regression rate by means of CFD [21]; finally at the University of Naples, hydrogen peroxide has been being tested in order to optimize a novel catalytic system, custom-developed, based on ceramic honeycombs in yttria-stabilized zirconia, with manganese oxides as the active phase [22].

As far as industrial realities are concerned, it has to be mentioned Nammo.

Nammo started testing 87.5% HP with HTPB in 2010, when ESA engaged the company for a TRL improvement program about hybrid rocket propulsion. Actually Nammo is engaged in a three year technology maturation program within the ESA Future Launcher Preparatory Programme (FLPP). The program goal is to scale-up Nammo's current state-of-the art hybrid rocket propulsion technology to large-scale, a scale that may have a function and interest in the near future for particularly sounding rockets and micro-satellite launchers. Nammo successfully conducted an intensive experimental campaign on a 1 kN throttleable engine, provided by vortex injection, in a 4:1 throttling range, assuring always a combustion efficiency higher than 97% [5], [6].

On december 2013, Bloodhound Project announced a new partnership with Nammo, as the rocket propulsion specialists. The BLOODHOUND SSC Project is Britain's latest attempt on the World Land Speed Record with a car capable of 1,000mph. Nammo's role will be to supply its hybrid rocket technology for use in the BLOODHOUND Supersonic Car which is now being constructed in Bristol, UK. A combination of these motors will be used in BLOODHOUND SSC to provide circa 125 kN of thrust which are to be combined with 90 kN thrust from the car's EJ200 jet. The Car is a mix of car and aircraft technology, with the front half being a carbon fibre monocoque like a racing car and the back half being a metallic framework and panels like an aircraft [24], [23].

1.2.2 Vortex Injection in Hybrids

The definition of vortex or swirl injection is not univocally stated in literature. In general these terms indicate the imposition of a rotational path to the incoming oxidizer. Different effects are produced according to the method adopted to produce this rotation. The main aim might be a fine atomization of the liquid oxidizer before its injection into the combustion chamber, or on the other hand, an enhancement of mixing inside the combustion chamber.

The present work is focused on this second typology of effect.

In this case, the injector gives the oxidizer a tangential component of velocity, when entering the combustion chamber; thus the fluid passes through the grain port, preserving a rotational pattern. As will be described in chapter [?], this strong swirling flow inside the combustion chamber enhances the mixing of reactants, improving the efficiency. Moreover the higher local mass flux due to the tangential component of the velocity, the stronger generated turbulence, the flame position nearer to the fuel surface due to centrifugal forces all concur to a large increase of the heat transfer to the grain wall,leading to a noticeable improvement of the regression rate.

Several configurations have been proposed during the years; a basic distinction regard the location of the injector; it can be placed at the head end or at the aft end of the motor.

As far as a head end vortex injector is concerned, one of the first structured work to be published is from Tokyo Metropolitan Institute of Technology (TMIT), in 1999 [25] and then 2001 [26]. TMIT developed a vortex injection hybrid rocket motor that utilized gaseous oxygen as oxidizer and PMMA as fuel. The team successfully developed an operational motor and flew the motor in a small hybrid rocket. The motor realized increases in fuel regression rate of up to 2.7 times that without the vortex.

Several works can be identified in the following years, produced by different research groups, regarding different configurations of head end vortex injector: from Arizona State University in 2002 [27], to TMIT again with Shimada [28], and U.S. Naval Academy [29], and University of Padova itself [?], [7], [8], more recently.

Again Nammo Raufoss has to be mentioned for having applied the head end vortex injection on its H2O2-HTPB hybrid motor [5], [6].

It has to be cited also the branch of works regarding grains with helical shaped port perforation, particularly widespread in Korea, which have been proposed for head end swirl oxidizer injection [31]. Swirl oxidizer flow injection with helical grain configuration can provide significant regression rate increases, up to 80% with respect to standard flow tests. Nevertheless, during combustion helical geometry is consumed by combustion. Therefore helical geometry effects are lessened yielding to possible combustion irregularities during the combustion phase.

On the other hand, as far as the aft end vortex injection is concerned, in the 1990s Knuth et al. [51] tested at ORBITEC a swirl injector, mounted immediately upstream the convergin part of the nozzle. Thanks to visualization experiments and numerical simulations, they discovered a double coaxial, co-swirling, counter-flowing vortex flowfield; the outer vortex proceeds toward the head end of the motor, mixing and burning with the pyrolyzed fuel; then it bends inward to come back towards the nozzle. Thanks to this peculiar behavior of the flow, the mixing and residence time of the reactants are strongly enhanced.

This fluid pattern was also confirmed by the analytic treatment made by Majdalani [32].

1.2.3 Throttling

First investigation about throttling can be dated back into the 1960s, when both US and Europe study the use of hybrids for sounding rockets, aerial target drones, tactical missiles.

ONERA developed a sounding rocket, called LEX (Lithergol EXperimental); it was

based on a hypergolic red fuming nitric acid (RFNA) and metatoluene diamine/nylon propellant combination [33]. This rocket was provided by an air driven solenoid valve, actuated by means of a programmable timer, in order to throttle the thrust from a peak of 10 kN down to 2 kN. This throttling capability was developed to optimize the performance during flight. Eight LEX rockets flew successfully between 1964 and 1967, reaching altitudes above 100 km.

In the same years, in USA a throttleable hybrid rocket was developed for aerial target drone applications. It is called Sandpiper. It burnt a mixture of nitric oxide (25%) and nitrogen tetroxide (75%) as oxidizer and a mixture of 10% powdered magnesium and 90% PMMA as fuel. The motor was throttleable to an 8:1 turndown ratio, with a peak thrust of 2.3 kN [34], [35]. The oxidizer feed system consisted of two lines, initially operating in parallel, for the boost phase of flight. At cruise speed, one line is closed by means of a normally open squib valve, and the required oxidizer flow rate is provided by the other line, by means of a pre-set orifice with adjustable cross section. Three successful Sandpiper demonstration flights were performed in 1968.

A second USA project followed Sandpiper, called HAST (High Altitude Supersonic Target) [36]. This was a drone too, and an evolution of Sandpiper. IRFNA and a 80% polybutadiene-20% PMMA mixture were used as propellants. In this case a more structured throttling was conceived; oxidizer regulation was performed by a pintle valve actuated by a torque motor with a ball screw. For the boost phase of flight, the valve was programmed to open to 50% of peak thrust and ramp up to full throttle over 20 seconds. Following the boost phase, the valve position could be commanded manually by a remote operator. These motors were throttleable in a 10:1 range with a peak thrust of 5.3 kN. The HAST program concluded with a series of ground tests, but the HAST propulsion system was used again in the mid-1980s with a new airframe in an aerial target drone known as the Firebolt [37].

In the 1970s and early 1980s, no significant research was performed on hybrid rockets due to the operational success of solid and liquid rocket systems developed in the 1960s.

In the mid-1980s the increasing market for commercial satellites coupled with catastrophic failures of the Challenger and a Titan III launch vehicle created a renewed interest in hybrid rockets.

Both NASA first and Loockheed Martin after initiated a series of project oriented to the investigation of hybrids as a valuable option for both boosters and sounding rocket applications. All the produced designs and testing foresaw a turndown or step throttling, thanks to a splitting of the main feed line in independent lines controlled by dedicated valves [38], [39], [40].

More recently, several academic institutions have developed throttleable hybrid rockets.

To make an example, a series of static test fires performed at Purdue University demonstrated a throttle-down profile analogous to a powered descent/landing profile, in a 10:1 throttling ratio, and a square wave profile analogous to a boost/sustain/boost profile that would be used for a tactical missile flight [41]

Peterson et al. [42] developed and tested successfully a closed-loop throttle controller, for a N2O-HTPB hybrid motor. Thanks to feedback functioning, the nominal thrust of 800 N could be turned down to 12 N, maintaining stable and controlled combustion.

Finally, Nammo has demonstrated a 4:1 throttling capability of its 1 kN motor, burning

87.5%HP-HTPB, during the maturation program funded by ESA [6].

1.3 Objectives and Methodology

The present research is focused on the investigation of a high performing throttleable hybrid rocket motor. This motor has been developed in the frame of the SPARTAN project (see sec. 1.2). This kind of motor is conceived to be used for soft-landing application in order to perform planetary exploration.

Such a kind of motor has to:

- guarantee high performances in a wide range of oxidizer mass flow rates, both in terms of repeatable, stable and efficient functioning at each level;
- be safe and reliable;
- be simple;
- be compact.

Thus the present research has the aim of characterizing a motor with the aforementioned features, conducting a deep investigation of the motor behavior at different fixed operative conditions. The dynamic response of the motor to throttling actuation is out of the scope of this work.

The reference characteristics of the motor have been defined according to the final configuration of the SPARTAN propulsion system; thus its main features are:

- throttleability,
- vortex injection,
- high concentration hydrogen peroxide as oxidizer

The aforementioned advantages of HP (see section 1.2), make it a suitable and interesting choice for hybrids. Since, as said, hydrogen peroxide in high concentration denotes also some drawbacks, an alternative experimental test bed has been conceived, to investigate the use of hydrogen peroxide without the risks connected to its handling. In this regard, a strong effort has been made to develope and optimize the functioning of a gas generator, responsible of simulating decomposed hydrogen peroxide in high concentration. As in the case of decomposition of HP through a catalyst, fuel ignition is expected to take place thanks to the heat flux provided by the hot oxidizer itself.

Thus the expected output of this research work regards:

- ignition:
  - capability of the hot oxidizer to ignite the fuel at each throttling level;
  - dependency of the ignition delay on the throttling level;
  - capability of the combustion process to be self-sustained, after ignition;
- issues related to HP:

  - presence of nozzle throat erosion, caused by combustion;
  - dependency of possible erosion phenomena on the throttling level;

- performance at different throttling levels:
  - combustion stability;
  - vortex injection effectiveness in increasing the regression rate;
  - resulting combustion efficiency;
  - dependency of the combustion efficiency on the throttling level.

In order to analyze the problem in its full spectrum, several tools have been used in synergy:

- simplified analytic models, which support the comprehension of the physical processes involved;
- numerical simulations, both for design purposes and for detailed investigation of aspects difficult to be understood by analytic models or to be observed experimentally;
- experimental tests, to validate the prediction and to assess the performance achieved.

Each one of these tools have been developed and optimized in order to satisfy a series of predefined requirements:

- analytic models have to:
  - be simple;
  - be representative, thus based on correct assumptions and hypothesis, and validated by experimental evidence;
  - require a small computational effort (computational time in the order several minutes).
- numerical simulations have to:
  - be reliable, and thus validated;
  - provide detailed information about the internal ballistic of the motor, and the peculiarities of the flowfield;
  - satisfy a good compromise between accuracy and computational cost (results convergence achieved in 8-24 hours).
- experimental tests have to:
  - be safe and simple;
  - be low cost;
  - be repeatable;
  - provide accurate measurements of the main interesting parameters, thanks to accurate diagnostics and preliminary calibrations of the main test bed subsystems;

  - provide useful information about stability and efficiency of the combustion process;
  - guarantee fast operation, in order to make possible doing 2 test per day, possibly every day, if needed.

1.4 Thesis Outline

- Chapter 2 describes the preliminary investigation of the motor. A preliminary design of the motor is defined. Then the numerical investigation performed by means of CFD simulations is described and the main outcomes are reported. The purposes of this preliminary study have been:
  - to understand the physical peculiarities of a vortex flowfield;
  - to assess the performance of the motor in its preliminary design;
  - to evaluate the sensitivity of the motor performance to some changes in the configuration or the operating conditions;
  - to provide guidelines for the final design of the motor and the experimental test-bed.
- Chapter 3 describes the complete experimental setup developed and integrated to simulate decomposed hydrogen peroxide in high concentration and perform the throttling tests of the hybrid motor. The calibration of the feed lines is finally reported.
- Chapter 4 reports a detailed description of the measurement system. The diagnostic systems are described and their measurement uncertainty is analyzed.
- Chapter 5 illustrates the experimental tests performed on the complete engine, at three different throttling levels. The main results are reported and compared, both between each other and with the theoretical expectation.

Chapter 2

Motor Preliminary Investigation

As a partner of the SPARTAN project (see section 1.2), the University of Padova has had the role of supporting the final design and testing of the flight motor for the soft-lander demonstrator, by means of advanced numerical investigation.

In this framework, UPD developed its own engine, in order to perform its own ground tests, and thus provide experimental data for numerical results validation.

The motor investigated in the present research is that developed in the SPARTAN framework. The preliminary design guidelines of the motor have been defined according to the requirements of the SPARTAN consortium, and specifically thanks to indications from Nammo Raufoss, based on the experience that the company maturated in its TRL improvement program, funded by ESA [6].

As already said, the present research has been carried out combining the experimental investigation with the numerical (CFD) and theoretical one. So, once the preliminary design of the motor has been defined, a deep numerical investigation has been performed. The numerical investigation has several purposes:

- to understand the physical processes which regulate the internal ballistic of the motor;
- to predict the motor behavior and performance;
- to provide useful guidelines to finalize the design and proceed with the experimental campaign.

This said, the chapter is dedicated to illustrate the preliminary configuration of the motor, as resulting from requirements and specifications, and then to describe the main outcomes of the numerical investigation.

2.1 Motor Preliminary Design

The UPD motor had to satisfy the following requirements:

- to be representative of the flight motor, as designed and indicated by Nammo;
- to be versatile, in order to make possible and easy to change the internal configuration by:

  - adding or removing pre- or post- combustion chamber;
  - changing the length of the fuel grain;

- to be simple and safely operated.

Table 2.1 reports the specifications imposed to UPD in designing its own engine.

It has to be underlined that these design specification of the lab motor have been identified in the preparatory phase of the SPARTAN project, and have not been modified in further development phases.

Table 2.1: Motor design preliminary specifications

Parameter	Value
thrust scale, [N]	1000 N
throttling ratio	10:1
oxidizer	87.5% H2O2
m_{ox} temperature, [°C]	660
m_{ox} composition	0.588 H2O, 0.412 O2
fuel	HTPB/C
injection	fully tangential vortex
vortex injector maximum pressure drop [bar]	2
vortex injector SN_g	4.5
maximum m_{ox}, [kg/s]	0.4
minimum m_{ox}, [kg/s]	0.08
maximum pressure, [bar]	40
maximum G_{ox}, [kg/m^2/s]	400
minimum G_{ox}, [kg/m^2/s]	50
mean OF ratio at nominal thrust	6.5
n, rr law	0.62
a, rr law	0.07

According to the requirements and specifications described above, a preliminary design has been defined. A simplified schematic is reported in figure 2.1.

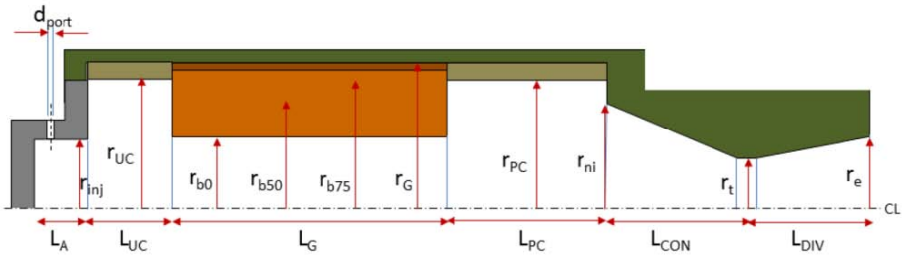

Figure 2.1: Motor preliminary configuration

The vortex injector configuration is based on specific indications provided by Nammo Raufoss AS [60]. It is a fully tangential vortex, defined by the parameters reported in table 2.2 (see figure 2.2 for nomenclature).

Parameter	Value
β, [deg]	90
θ, [deg]	90
r_{inj}, [mm]	31
r_{port}, [mm]	11.5
N_{port}	20
SN_g	4.82

Table 2.2: Motor preliminary design

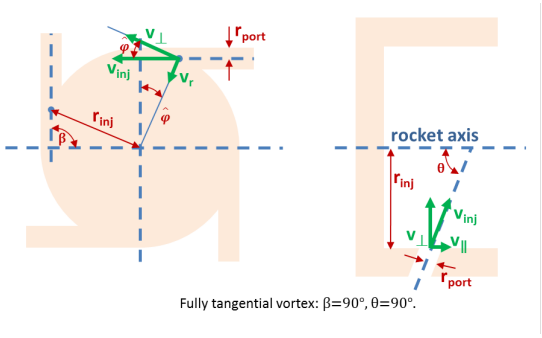

Figure 2.2: Vortex injector schematic with nomenclature

The parameter SN_g, in table 2.2 represents the geometrical swirl number, which, for a full-tangential vortex is calculated as:

$$SN_g = \frac{(r_{inj} - r_{port})\, r_{inj}}{N_{port} r_{inj}^2} \tag{2.1}$$

In the case of a mixed axial-tangential injector, the swirl number has to be multiplied by the sine of the injection angle.

The geometrical swirl number is a simplified representation of the intensity of the fluid vortex intensity at the inlet. As it can be seen by equation 2.1, it depends uniquely on geometrical parameters of the injector.

The effective swirl number is instead defined as the ratio between the axial fluxes of angular and linear momentum respectively, as reported in eq. 2.2 (see figure 2.2 for nomenclature). This parameter can give information about the relative intensity of the rotational flow and how it varies along the motor because of heating, friction, mass addition and section changes. Since the fluid field is not well known a priori, the formulation of eq. 2.1 has been used in preliminary design phases.

$$SN = \frac{\int \rho v_{\parallel} v_{\perp} r \, dA}{r_{inj} \int \rho v_{\parallel}^2 dA} \tag{2.2}$$

2.2 Vortex Injection Investigation

This section describes the main results of the numerical investigation performed.

The numerical analysis has been conducted in two phases:

1. a first cognitive phase, to understand the basic physics of vortex injection;
2. a detailed characterization of vortex injection's influence parameters.

In the first phase, preliminary simulations have been carried out on a motor configuration already developed and tested at UPD, in order to study and characterize the physics beyond vortex injection, and thus assess its effectiveness in enhancing the hybrid motor performance. The numerical results have been compared with an analytic model of the vortex flowfield. The outcome of this phase has been compared with experimental data already available.

In the second phase, the preliminary design produced within SPARTAN has been simulated to predict its performance and its sensitivity to some changes in the motor configuration and operative conditions. A prediction of the expected performance and some useful indications for the experimental tests are the main output of this second phase.

2.2.1 Vortex Modeling

The main aim of this theoretical and numerical analysis has been to study the main features which characterize vortex injection, thus comparing them with the peculiarities of a correspondent axial injector (i.e. a classical shower head).
CFD analysis has been combined with analytic model to explain the typical flowfield generated by vortex injection and understand the main causes of motor performance improvement.

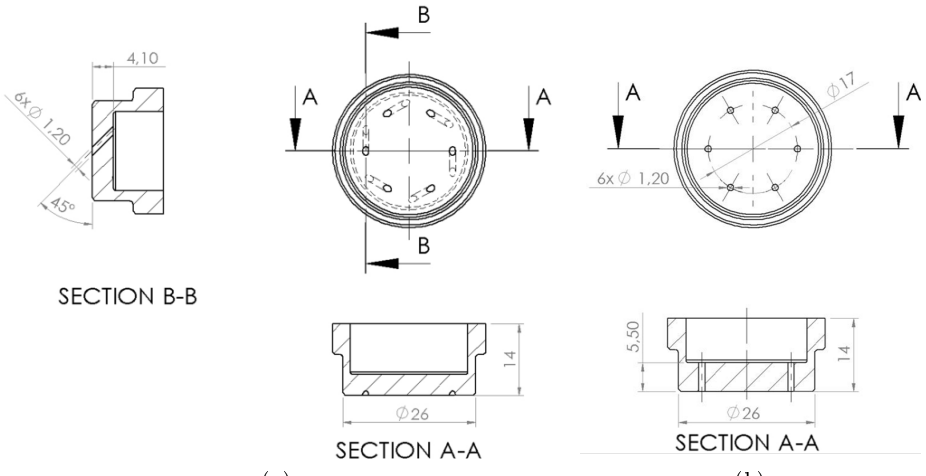

(a) (b)

Figure 2.3: Mixed axial-tangential vortex injector (a) compared to the corresponding axial one (b)

Several configurations of vortex injector can be identified, depending on the velocity components given to the flow at the inlet. In this specific case a mixed axial-tangential injector has been investigated, shown in figure 2.3, in comparison with a correspondent axial one, that is with the same holes diameter, same L/D ratio and same holes positioning. According to this design, the injection channels give the fluid both an axial and tangential component. The motor configuration simulated is representative of a true motor, actually tested by UPD [7]. The availability of experimental data has given the possibility: to provide the required input for the simulation setup; to tailor the numerical model, both in terms of settings and mesh; to verify the correctness and accuracy of the numerical results. Figure 2.4 shows the CAD drawing of the lab-scale experimentally tested, with the main dimensions reported.

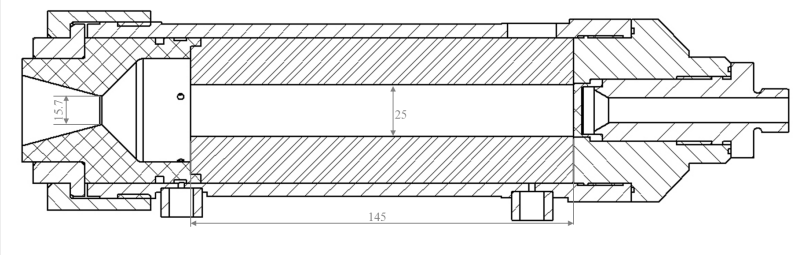

Figure 2.4: Lab-scale motor configuration tested with mixed axial-tangential vortex injector

CFD investigation has been carried on with a step by step approach, to analyze separately the effect of several factors on the oxidizer flowfield, and its development inside the combustion chamber. The different contributions considered have been:

1. pyrolyzed fuel injected from the grain surface, with no chemical reaction;
2. pyrolyzed fuel injected from the grain surface, with chemical reaction (i.e. combustion);
3. combustion with nozzle acceleration contribution;
4. comparison with axial injection.

According to what just listed, table 2.3 summarize the main feature of the simulations performed.

Analytic Model

Compressible Navier-Stokes equations, neglecting the gravity and normal viscous terms are considered.
In cylindrical coordinates, balance in tangential direction is the following:

$$\begin{aligned} \rho\left(\frac{\partial u_\theta}{\partial t}+u_r\frac{\partial u_\theta}{\partial r}+\frac{u_\theta}{r}\frac{\partial u_\theta}{\partial \theta}+u_z\frac{\partial u_\theta}{\partial z}+\frac{u_r u_\theta}{r}\right)= \\ -\frac{1}{r}\frac{\partial p}{\partial \theta}+\mu\left[\frac{1}{r}\frac{\partial}{\partial r}\left(r\frac{\partial u_\theta}{\partial r}+\frac{1}{r^2}\frac{\partial^2 u_\theta}{\partial \theta^2}+\frac{\partial^2 u_\theta}{\partial z^2}\right)-\frac{u_\theta}{r^2}+\frac{2}{r^2}\frac{\partial u_r}{\partial \theta}\right] \end{aligned} \tag{2.3}$$

Test case	Peculiarity				
	Injector	**Oxidizer injection**	**Fuel injection**	**Combustion**	**Nozzle**
Cold	vortex	y	n	n	n
Blowing	vortex	y	y	n	n
Hot	vortex	y	y	y	n
Nozzle	vortex	y	y	y	y
Axial	axial	y	y	y	y

Table 2.3: Mixed axial-tangential vortex: CFD configurations investigated

Some simplifications can be introduced:

- steady state flow, thus: $\frac{\partial}{\partial t} = 0$;
- axis-symmetry, thus: $\frac{\partial}{\partial \theta} = 0$;
- variation of tangential velocity in z can be neglected, thus: $\frac{\partial u_\theta}{\partial z} = \frac{\partial^2 u_\theta}{\partial z^2} \approx 0$;
- radial velocity is negligible respect to the other two components, thus: $u_r \approx 0$.

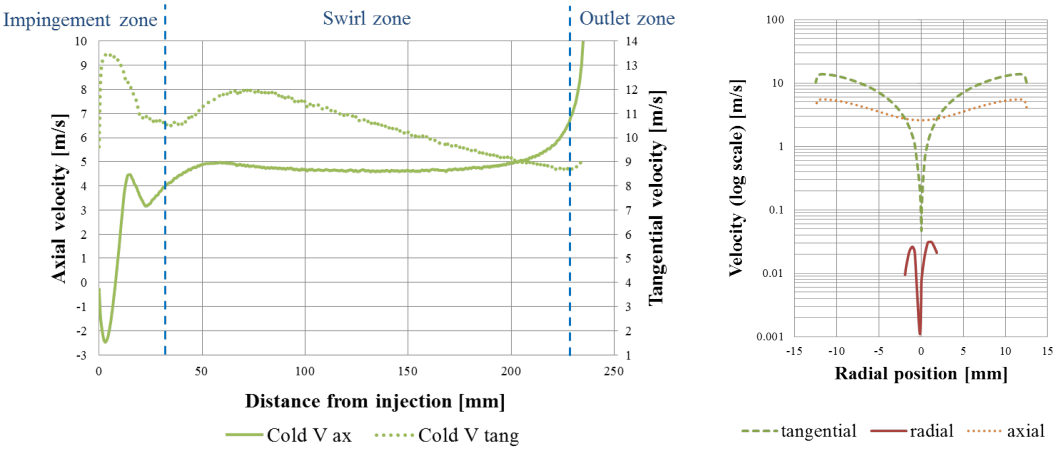

(a) (b)

Figure 2.5: Simplification of the Navier-Stokes equations: axial and tangential velocity components are shown along an axial line 1 mm apart from grain surface(a), and radial component is compared to the other along a radial line at the middle of the grain length (b)

Referring to *Cold case* configuration (see table 2.3), the last two statements have been confirmed credible through CFD simulations, as can be observed in figure 2.5. The axial and tangential velocity component are shown along an axial line, located 1 mm apart from

the grain surface (figure (a)): excluding dissipation effects due to impingement and outlet, the tangential velocity is subjected to a minor reduction due to friction, while in this case axial velocity is kept constant according to continuity equation. Moreover radial velocity is compared to the other components (figure (b)), in correspondence of a radial line, located 10 cm apart from the injection (and thus approximately in the middle of the grain): it can be seen that its contribution is negligible.

The simplifications introduced reduce eq. 2.3 to the form:

$$\frac{1}{r}\frac{\partial}{\partial r}\left(r\frac{\partial u_\theta}{\partial r}\right) - \frac{u_\theta}{r^2} = 0 \tag{2.4}$$

The solution for this equation is that of a forced vortex:

$$\omega\, r = u_\theta \tag{2.5}$$

where ω expresses the angular velocity.

This analytic result has been compared with the CFD results; figure 2.6 shows the tangential velocity, case by case (see table2.3 for nomenclature), along a radial line located 10 cm far from inlet. An almost linear trend of tangential velocity as a function of radial position can be observed in any case, thus suggesting the absence of sliding effects, and so confirming the theoretical prediction of forced vortex. A constant angular velocity, which makes tangential velocity proportional to radial position, is mathematically correct when only oxidizer is injected, but is empirically valid also for the other cases. Observing the curves in correspondence of the radial periphery, it can be seen that a border effect is present; the change in tangential velocity can be ascribed to:

- friction with walls in *cold case*;
- friction with fuel flow in *blowing case* (this is less effective, as suggested by the example of the no-friction table with air films);
- chemical reactions and flame development, in *hot* and *nozzle* cases.

In cylindrical coordinates, balance in radial direction is the following:

$$\begin{aligned}\rho\left(\frac{\partial u_r}{\partial t} + u_r\frac{\partial u_r}{\partial r} + \frac{u_\theta}{r}\frac{\partial u_r}{\partial \theta} + u_z\frac{\partial u_r}{\partial z} - \frac{u_r^2}{r}\right) = \\ -\frac{\partial p}{\partial r} + \mu\left[\frac{1}{r}\frac{\partial u_r}{\partial r} + \frac{1}{r^2}\frac{\partial^2 u_r}{\partial \theta_2} + \frac{\partial^2 u_r}{\partial z_2} - \frac{u_r}{r^2} - \frac{2}{r^2}\frac{\partial u_\theta}{\partial \theta}\right]\end{aligned} \tag{2.6}$$

Applying the same hypothesis assumed for the tangential direction equation, eq. 2.6 becomes:

$$\rho\frac{u_\theta^2}{r} = \frac{\partial p}{\partial r} \tag{2.7}$$

Some additional hypothesis can be considered:

- ideal gas;
- null chemical gradient in the radial direction;

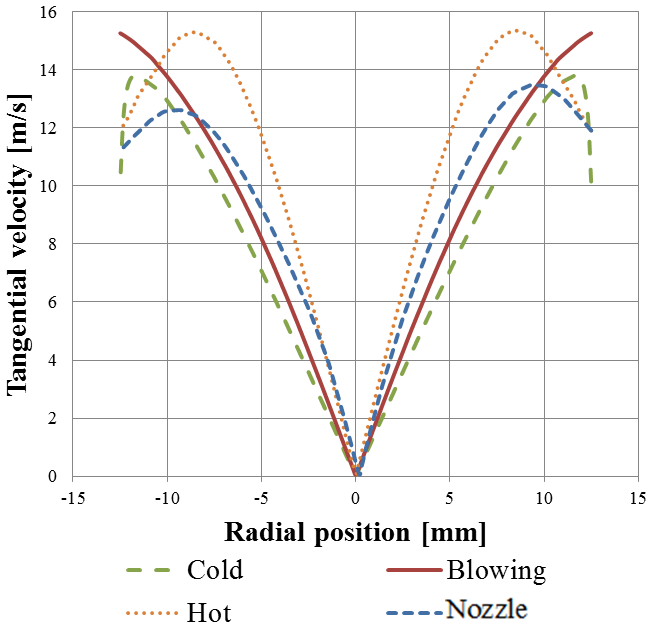

Figure 2.6: Tangential velocity along a radial line located at the middle of the grain

- null temperature gradient in the radial direction.

The first one listed, combined with the formulation of forced vortex lead to:

$$\rho \frac{u_\theta^2}{r} = \frac{\partial p}{\partial r} = \frac{\omega^2 r \, M_m p}{R_u T} \tag{2.8}$$

Finally considering the second and third hypothesis, eq. 2.8 can be integrated between the axis center of the motor ($r0 = 0$ and $p = p_{r0}$) and a generic position r, giving:

$$\frac{\omega^2 r^2 M_m p}{2\, R_u T} = ln\left(\frac{p}{p_{r0}}\right) \tag{2.9}$$

$$\frac{\omega^2 r^2 M_m p}{2\, R_u T} = ln\left(\frac{\rho}{\rho_{r0}}\right) \tag{2.10}$$

These equations highlight a centrifugal effect due to the rotation of the flow, pushing the fluid towards the external wall of the combustion chamber.
The analytic result has been compared with the CFD result in figure 2.7. There is a perfect correspondence between the theoretical solution and the cold simulation result (see figure 2.7a). Once again, increasing the complexity of the system, the actual solution deviates from the mathematical one: adding mass (blowing case) does not give any significant contribution, but, when combustion takes place, these formulas are no longer valid to predict the pressure distribution. However, the same trend is followed, and so its effect on the flow field: pressure increasing from center to walls (see figure 2.7b).

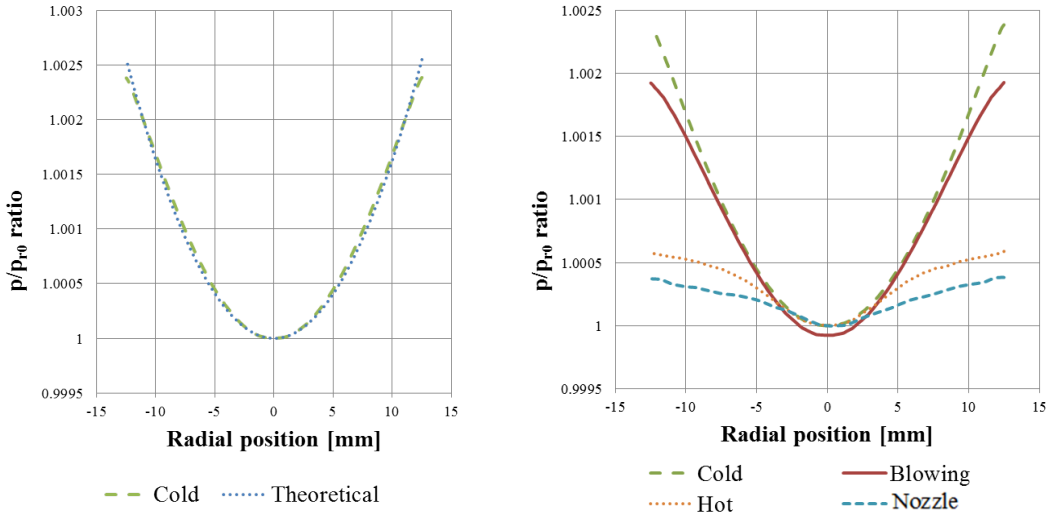

(a) (b)

Figure 2.7: Pressure ratio radial profiles: profiles are compared case by case along a radial line at the middle of the grain length in (a); (b) compares the theoretical profile with the *cold case* numerical one

In case of temperature or chemical composition gradients, this force acts as a mixer: the heaviest components (i.e. reactants) are pushed outwards, while the lighter (i.e. reaction products) are pulled towards the axis of the combustion chamber.

Numerical Setup

All the simulations have been performed at steady state, thus to simulate a specific instant of motor functioning.

Mesh is based on unstructured tetrahedral elements. Inflation layer has been set up at the fuel surface to better simulate fuel injection and flame attachment. Appropriate mesh refinement has been needed in correspondence of nozzle throat and injection channels. The final mesh settings is the result of a sensitivity study. Several mesh settings have been tempted and numerical results have been compared: axial and tangential velocity components have been evaluated at specific locations of the fluid volume, together with average temperature and pressure; convergence has been considered achieved when the previously mentioned variables have shown a variation below 3% from one mesh setting to the following one.

The total number of elements is $\approx 1.9 \cdot 10^6$, which required a reasonable computational cost (i.e. about 8 hours) with a standard PC (4 cores, 4 GB RAM). Table 2.4 summarizes the final mesh setup characteristics.

The $k - \epsilon$ turbulence model has been adopted, with scalable wall functions.

Figure 2.8 reports the fluid geometry, used for the case "Nozzle" (see table 2.3), with the correspondent boundary conditions.

Referring to figure 2.8a, the boundary conditions are:

Parameter	Value
Global maximum face size, [mm]	1
Global maximum element size, [mm]	1
First inflation layer thickness, [mm]	0.1
Number of inflation layers	5
Inflation layers growth rate	1.1
Nozzle throat element size, [mm]	0.5
Inlet surfaces element size, [mm]	0.3

Table 2.4: Preliminary numerical investigation about vortex: main mesh settings

(a) (b)

Figure 2.8: Numerical investigation about axial-tangential vortex: fluid volume with boundary conditions (a), with a zoom detail on the injection area (b)

- oxidizer inlet with fixed mass flow (cross sections of the inlet channels encircled in red);
- fixed fuel mass flow inlet at fixed temperature (blue surface);
- outlet at ambient pressure (1 bar) in correspondence of the nozzle exit section (orange surface);
- no slip wall with adiabatic condition for the other surfaces.

As far as the simulations without nozzle are concerned, a opening condition at 25 bar has been set at the end of the post-combustion chamber.

In the experimental tests it is expected that the oxidizer enters the injector in liquid phase. In the CFD model, the vortex injector channels have been enlarged respect to their actual diameter, since the simplification of gaseous oxidizer would have led to an unlikely inlet velocity. To oversize the channels, the following approach has been followed:

- mass flow rate has been extrapolated from experimental data, [7];
- density of the liquid phase has been derived from pressure and temperature information, interpolating NIST data;
- actual velocity of the liquid oxidizer has been calculated;

- hole diameter has been deduced, in order to have for the gaseous oxidizer the same inlet velocity as the liquid; density of the gaseous phase has been derived from CFD tool database.

Respect to the actual holes diameter, 1.3 mm, a corrected value of 4.95 mm has been calculated.

Considering the axial injection geometry, all the back surface has been set as inlet (green surface in figure 2.8b); this has been proved to be valid and more accurate than simulating each channel [46]. In fact, when oxidizer enters the combustion chamber in liquid state, it evaporates in a certain length; evaporation causes the fluid to slow down and expand, creating a more uniform advancing front.

Thermochemistry. The oxidizer in nitrous oxide, N2O, injected in gaseous phase at 298 K, normally to the inlet channels cross sections; fuel is paraffin wax, injected radially at 725 K [43],[44], as pyrolysis products according to the reaction:

$$C_nH_{2n+2} \rightarrow H_2 + (n/2)\, C_2H_4 \tag{2.11}$$

A sensitivity analysis has been performed about the value of the fuel inlet temperature, in the expected range, and a negligible influence on the results has been found.

The chemistry of the flame is treated with the eddy dissipation model. The reaction has been described with a single step, and balanced as follows:

$$\begin{aligned} 151\, N_2O + 1\, H_2 + 25\, C_2H_4 \rightarrow 148\, N_2 + 23\, CO_2 + 27\, CO + 40\, H_2O + 10\, O_2 + \\ + 6\, NO + 10\, OH + 2\, O + 5\, H2 + 2\, H \end{aligned} \tag{2.12}$$

The selection of the products comes from an analysis of the combustion with a thermochemical software (CEA), choosing only those chemical species that have a molar fraction higher than 10^{-3}.

The main simplifications adopted to describe the N2O-wax chemistry are:

- all the species involved are treated as ideal gases;
- oxidizer is injected in gaseous state;
- fuel is injected in gaseous state at fixed flow rate;
- fuel droplets entrainment (typical of liquefying propellants, ref. [47]) is not represented;
- simplified chemical reaction: one reaction, no backward reactions, no homogeneous decomposition of N2O due to temperature effect, and no kinetic effects.

Main Results

In case of vortex injection, considering the velocity profile, the fluid field can be divided in 3 sections, as illustrated in figure 2.9:

1. close to the injector, the flow is not fully stabilized: the oxidizer, ejected from the holes, impinges on the chamber surfaces; then it is forced to follow the curvature of the grain;

2. along the grain port, the motion is stabilized, the fluid follows an helical path; streamlines tend to stretch because of several factors;

3. through the nozzle, flow is heavily accelerated.

A strong impingement has been observed with this configuration of vortex injector. This has the effect of producing a not uniform consumption of fuel grain along its entire length: where the fluid impinges, heat flux is higher and thus regression rate. This consideration has been further confirmed by experimental tests performed by UPD [7], as can be seen in figure 2.16.

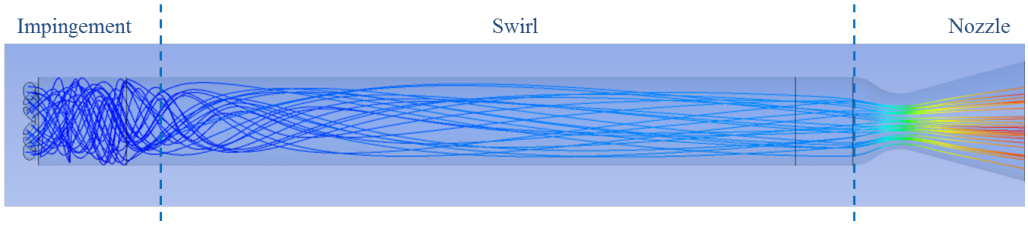

Figure 2.9: Typical vortex flowfield development

As deduced in section 2.2.1, because of vortex flowfield, centrifugal forces cause a pressure gradient in the radial direction, that is absent in the axial case (see equation 2.10 and figure 2.7). This gradient changes along the axis: near the injector, pressure gradient from outward to inward is steeper than downstream. This aspect can be explained considering equation eq. 2.10: given the same angular velocity, pressure gradient is higher where the fluid is colder, because of higher density, and where the molar mass is higher, because of inertial forces.

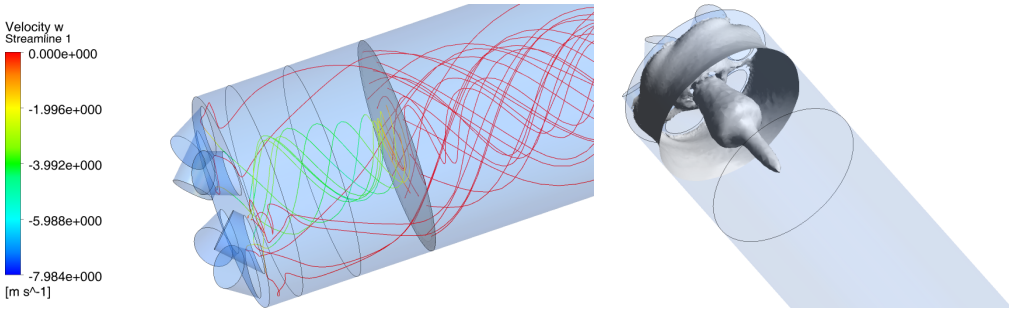

(a) (b)

Figure 2.10: Rip-tide effect in vortex injection: forward streamlines from a cross plane 2 mm apart from injector, (a), and iso-surface of null axial velocity (b)

A sort of suction, called *rip-tide effect*, is observed close to the axis in correspondence of the head end of the motor (see figure 2.10), caused by this distribution of pressure gradi-

ents already described: in proximity of the head end, a certain amount of fluid recirculates towards the injector from the axis-center. Figure 2.10 depicts the isosurface corresponding to a null value of axial velocity: this means that a sign inversion of the axial velocity takes place between inward and outward the surface.
This recirculation zone has a volume that decreases, going from *cold* simulation to *blowing*, *hot* and *nozzle*, because pressure gradients mitigate progressively (see figure 2.7b).

The effect of mass flow adduction, chemical reaction and isentropic acceleration on vortex behavior as been evaluated comparing *Cold*, *Blowing*, *Hot* and *Nozzle* cases. In figure 2.11 axial and tangential velocity are plotted along an axial line, placed 1 mm apart from grain surface. The difference in axial velocity between *cold* test and *blowing* test is low, with a slight acceleration in the second case, due to a total mass flow rate increase. This difference increases when combustion takes place due to the increasing temperature. The nozzle effect is negligible respect to that of chemical reactions. As far as the tangential velocity is concerned, generally, it results far less affected by changes in total mass flow rate a chemical processes: in the swirl zone after impingement and flow stabilization this parameter softly changes along most length of the grain.

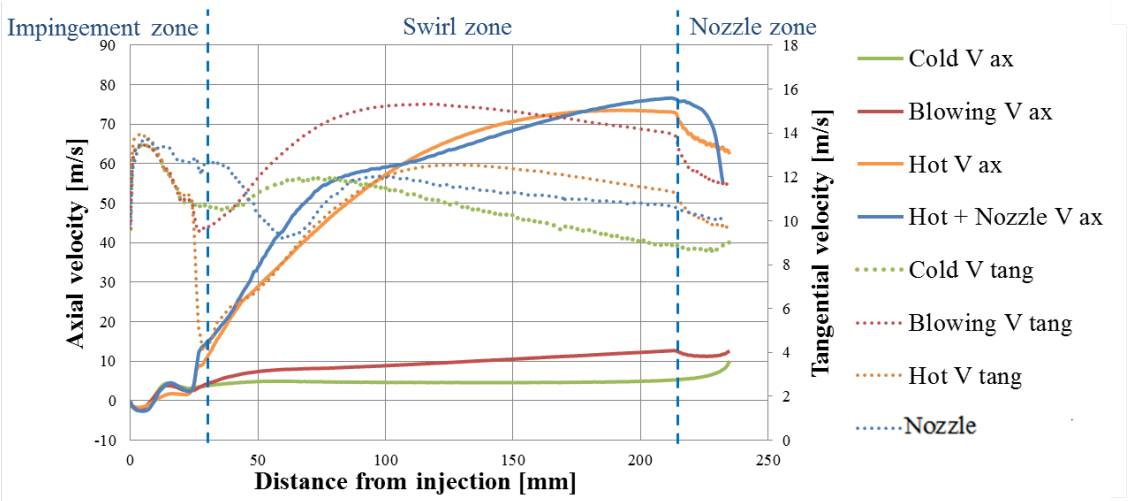

Figure 2.11: Axial and tangential velocity profiles along an axial line located 1 mm apart from the fuel grain

Swirl angle has been calculated for each case as follows:

$$\delta = \operatorname{atan}\left(\frac{u_z}{u_\theta}\right) \tag{2.13}$$

Figure 2.12 compares the swirl angle case by case, as calculated along an axial line located 1 mm apart from the fuel grain surface. After the impingement region, swirl angle slightly changes, and it can be seen once again the effect of the combustion. Taking into account what observed about the velocity components (see figure 2.11), it can be concluded that the combustion straighten the streamlines mostly because it accelerate the axial component of the velocity, while the tangential remains almost the same.

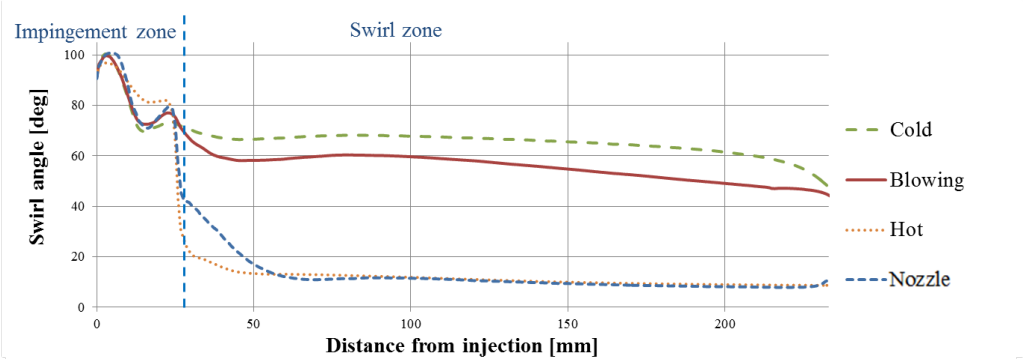

Figure 2.12: Swirl angle comparison along an axial line located 1 mm apart from the fuel grain

It has been noticed, however, a residual tangential component of the flow when exiting the nozzle, which has been evaluated to cause a thrust loss of approximately 2 %; this aspect should be object of investigation in terms of possible momentum compensation if the motor would have been mounted on a vehicle. Figure 2.13 shows this residual tangential component at the outlet.

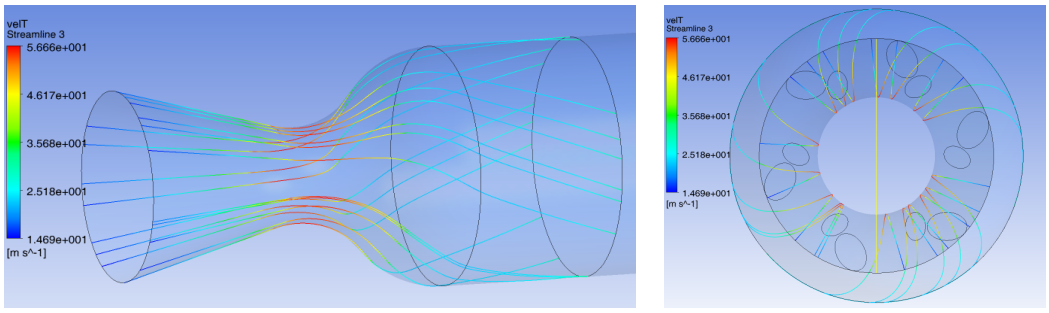

(a) (b)

Figure 2.13: Vortex flow simulation: nozzle detail in a side (a) and back view(b)

Figure 2.14 shows streamlines for all the simulated cases: it can be observed their progressive straighten respect to the cold injection case ((a)) because of total mass increasing ((b)) and combustion ((c)) and nozzle acceleration ((d)). As a final comparison, also the axial injection case is shown ((e)), where streamlines are straight.

As far as the comparison between *Axial* and *Nozzle* cases is concerned, the axial injection produces the typical strongly stratified flowfield with the fuel and the oxidizer moving almost parallel to the flame along the port (see figure 2.15b, where oxidizer mass fraction along the motor is shown). This produces the typical low performances normally encountered in hybrid rockets, as can be seen in figure 2.15a. On the contrary the vortex injection produces a strong helical flow that enhances the turbulence level in the combustion chamber. Thanks to centrifugal effects, the hot products are mixed with the central cold core and this allows for fresh oxidizer to reach the flame: this drive to a more complete, and thus efficient, combustion process (see figure 2.15d, where oxidizer mass fraction along the

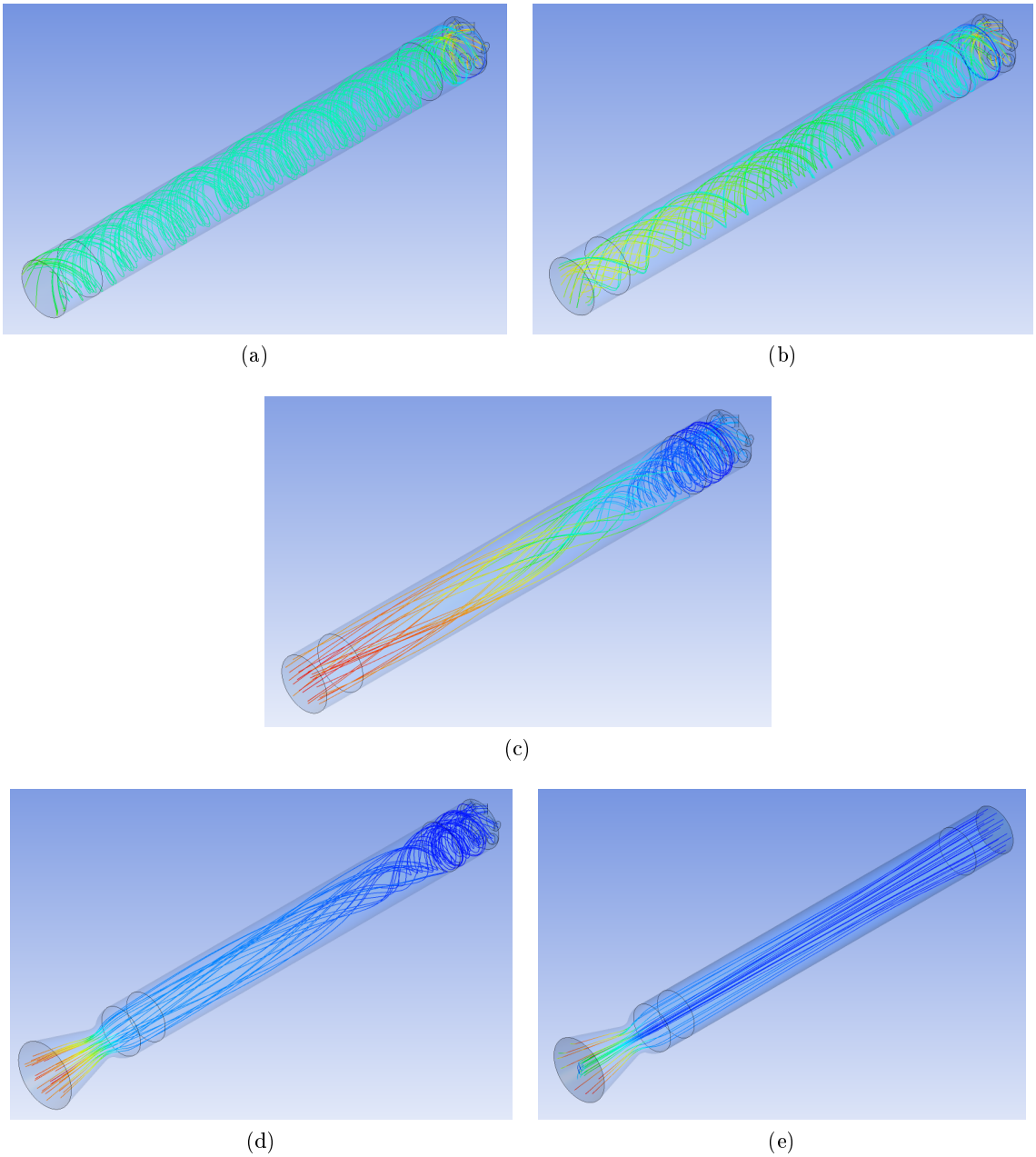

(a) (b)

(c)

(d) (e)

Figure 2.14: Streamlines comparison case by case: vortex injection cold(a), vortex blowing(b), vortex hot(c) and vortex hot with nozzle(d) and axial injection hot with nozzle (e)

motor is shown) and to a more uniform diffusion of combustion products inside the combustion chamber, as can be observed by a more diffusely hot temperature in figure 2.15c. Moreover centrifugal forces push the flame near the wall enhancing the heat flux and thus the regression rate. This is confirmed by a very thin, and close to the grain surface, flame.

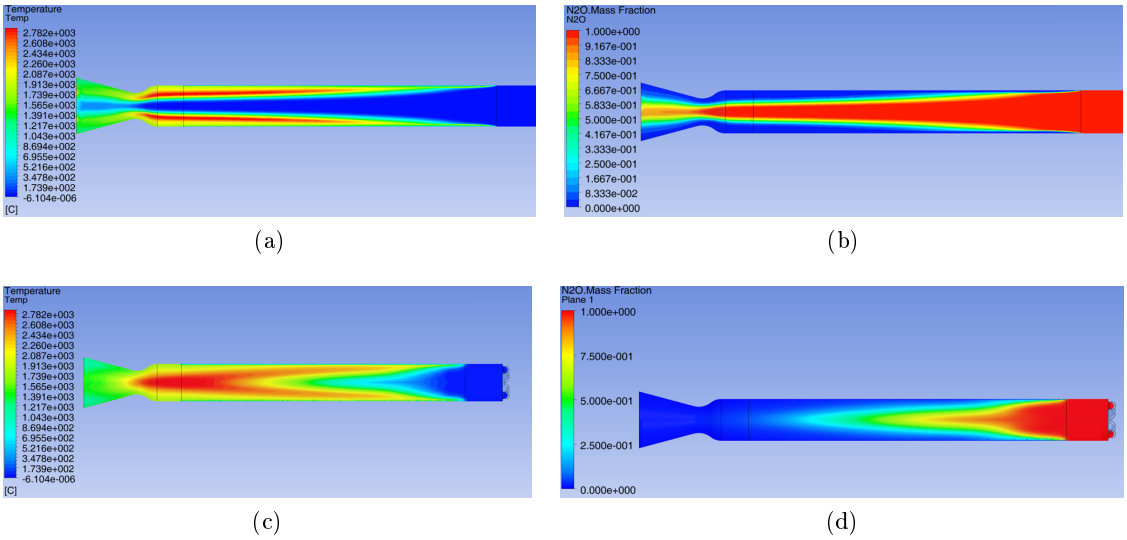

Figure 2.15: Flame temperature profiles: (a) and (c) show the temperature profile for the axial and vortex case respectively; (b) and (d) show the oxidizer consumption for the same case respectively

Experimental Feedback

Experimental tests with the same chamber geometry have been performed by UPD, with both pressurized and self-pressurized N2O. The reader is referred to Bellomo et al. [7] and [48]) for a complete description of the experimental campaign.

The strong impingement effect predicted by CFD simulations for this configuration of vortex injector has been confirmed by experimental evidence. Figure 2.16 compares the grain consumption obtained for an axial ((a)) and a vortex ((b)) test: a strongly nonuniform consumption of the fuel grain is observed in (b); where the fluid impinges, heat flux is higher and thus regression rate.

Experimental tests have confirmed also the presence of a rip-tide effect. In fact figure 2.17 compares the experimental evidence with the CFD prediction: (b) shows the axial velocity, just downstream the injector (2 mm apart); scale has been limited to negative values to highlight backflow. (a) shows some traces of residuals spotted on the injection plate by this backflow effect.

Measured performances showed an increase in regression rate up to 51% and a combustion efficiency that rises from values lower than 80% in the axial injection configuration, up to more than 90% with vortex. Moreover, a reduction of the instabilities in the chamber pressure has been measured.

This investigation has been followed by an experimental and numerical project, intended to study fully tangential vortex injection: for complete details, the reader is referred to Bellomo's PhD dissertation [49] and Bellomo et al. [12] and [8]. Even in this case the hybrid motor burned N2O as oxidizer, and wax as fuel; the class is again that of lab-scale

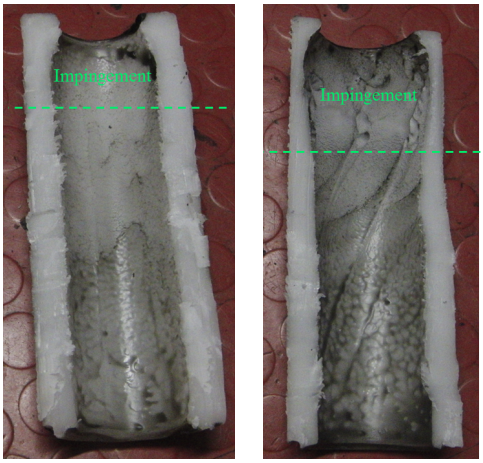

(a) (b)

Figure 2.16: Fuel grain consumption after 3 s burning for an axial injection test (a) and a vortex one (b)

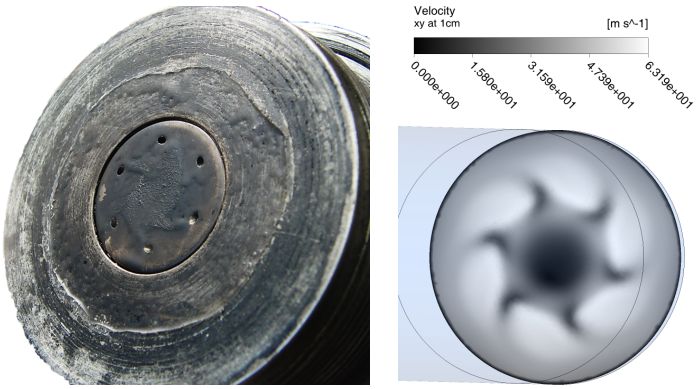

(a) (b)

Figure 2.17: Rip-tide effect: vortex injector after burn (a), presents paraffin residuals distributed in a characteristic path, which is reproduced by CFD simulation, (b)

motors (i.e. 1kN). Even if mixed axial-tangential vortex has been demonstrated to provide an increase in performance, a non-uniform grain consumption has been observed. This further work had three objectives:

1. to compare fully tangential vortex injection with axial injection;
2. to study the motor throttling behavior at fixed operating points;
3. to evaluate the effect of changing the combustion chamber configuration on the performance.

During this experimental campaign, a reduction of pressure oscillations has been observed respect to the axial case, from more than 7% down to 4%.

Moreover, regression rate has been increased of 41%. Combustion efficiency passed from the axial case value of 76% to up to 90% with vortex.

Finally, in this case, an almost uniform fuel grain consumption has been observed along the grain; fuel frontal consumption has been detected, due to the absence of protection disks.

2.2.2 Preliminary Assessment on the Motor Performance

A set of 9 cases has been simulated by means of commercial CFD to investigate the peculiarities of the hybrid motor with fully tangential vortex injection, when some geometrical and physical parameters are changed.

The base geometry corresponds to the preliminary motor configuration described in section 2.1.

Figure 2.18 shows the fluid geometry which corresponds to the first simulated case, "C1". This represents the fluid geometry corresponding to the motor preliminary design reported in section 2.1.

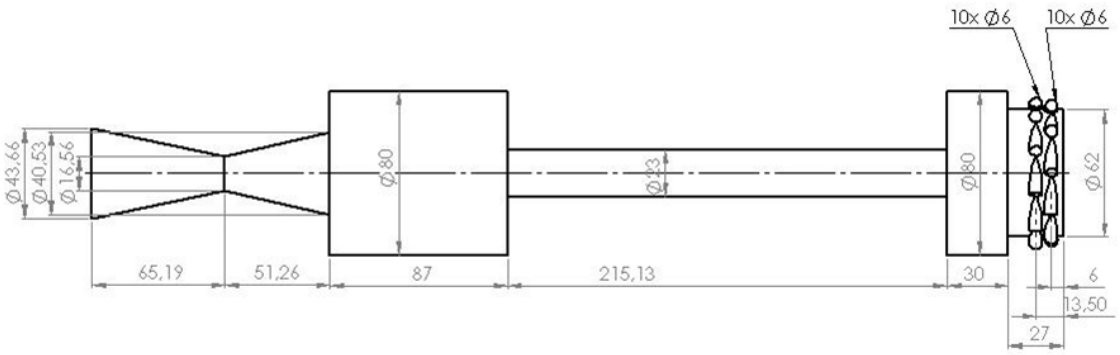

Figure 2.18: CAD drawing of the reference fluid volume, used for CFD investigation about vortex

Table2.5 reports the details about the simulated cases. For nomenclature about injector configuration, the reader is referred to figure 2.2.

The nominal oxidizer flow rate used is that reported in table 2.1.

The swirl number, SN_g, reported in table 2.5 is the geometric one, as calculated according to equation 2.1; moreover, $D_{p,0}$ refers to the initial port diameter, and $\dot{m}_{ox,n}$ is the nominal mass flow rate.

For the fuel mass flow rate calculations it has been employed the relation with the regression rate:

$$\dot{m}_{fuel} = \rho_{fuel} A_{burn} \left[a \left(\frac{\dot{m}_{ox,n}}{A_p} \right)^n \right] \tag{2.14}$$

where the preliminary values of a and n were provided by Nammo Raufoss AS [60]:

- a=0.08, for $\left[G_{ox} = \frac{kg}{m^2 s} \right]$;
- n=0.68;

Test case	Peculiarity	Injector configuration			Pre cc	Grain	Post cc	Mass flow rates	
		β,[deg]	θ [deg]	SN_g				$\dot{m}_{ox}$	$\dot{m}_{fuel}$
C1	*Reference case*	90	90	4.82	y	$D_{p,0}$	y		
C2	SN_g *doubled*	90	90	9.64	y	$D_{p,0}$	y		
C3	*Axial-tangential injector*	90	45	4.59	y	$D_{p,0}$	y	$\dot{m}_{ox,n}$= 0.4 kg/s	$\dot{r} = a\, G_{ox}^{n}$
C4	*Post-cc removed*	90	90	4.82	y	$D_{p,0}$	n		
C5	*Pre-cc removed*	90	90	4.82	n	$D_{p,0}$	y		
C6	*Pre-cc and post-cc removed*	90	90	4.82	n	$D_{p,0}$	n		
C7	*Port diameter at 75% burn time*	90	90	4.82	y	$D_{p,75}$	y		
C8	$\dot{m}_{ox}$ *reduced at 10%*	90	90	4.82	y	$D_{p,0}$	y	$0.1 \cdot \dot{m}_{ox,n}$	
C9	$\dot{m}_{ox}$ *reduced at 50%*	90	90	4.82	y	$D_{p,0}$	y	$0.5 \cdot \dot{m}_{ox,n}$	

Table 2.5: Tangential vortex: CFD configurations investigated

Numerical Setup

All the simulations have been performed as steady-state, each representing a specific instant during motor operation.

A sensitivity analysis on the mesh element size has been performed: the "C1" section geometry has been meshed in several ways with different maximum element size and sizing refinement to identify the best compromise between the total number of elements (and so the computational cost) and the accuracy of the results. The selected mesh configuration has been then adopted for all the simulations.

All the fluid geometries simulated have been meshed with unstructured tetrahedral elements, with inflation near the walls, and a specific refinement near the nozzle throat and the inlet regions. The most important mesh settings are reported in table 2.6, as finally adopted to simulate the nine cases.
This set up usually determines a mesh counting nearly 2 million elements, which implies a computational cost of about 8 hours to reach convergence with a common 8-cores processor and 8GB RAM.

The $k-\omega$ turbulence model has been applied.

Referring to figure 2.19, the boundary conditions are:

- oxidizer inlet with fixed mass flow (blue surfaces);
- wall with no slip condition, fixed temperature and fixed mass flow sources where the fuel is injected (red surface);
- outlet at ambient pressure (1 bar) in correspondence of the nozzle exit section (orange surface);

Parameter	Value
Global maximum face size, [mm]	1
Global maximum element size, [mm]	1
First inflation layer thickness, [mm]	0.1
Number of inflation layers	8
Inflation layers growth rate	1.2
Nozzle throat element size, [mm]	0.6
Inlet regions element size, [mm]	0.4

Table 2.6: Numerical investigation about vortex: main mesh settings

- only for wedge geometries: rotational periodicity, in correspondence of the cut sections of the slice (one shown, green surface);
- no slip wall with adiabatic condition for the other surfaces.

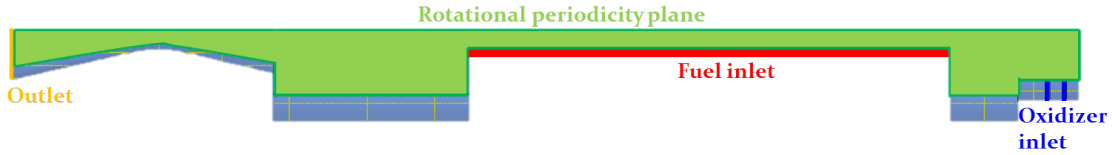

Figure 2.19: Numerical investigation about vortex: boundary conditions

Thermo-chemistry. Oxidizer is hydrogen peroxide, 87.5% concentration; fuel is HTPB. The oxidizer is injected as its decomposed products, according to the chemical balance equation:

$$1\,H_2O_2\,(87.5\%) = 0.788\,H_2O_2 + 0.212\,H_2O \rightarrow 1\,H_2O + 0.394\,O_2 \tag{2.15}$$

Oxidizer is injected in gaseous phase, as after being decomposed through a catalyst; its temperature is about 933 K (i.e. the decomposition temperature).

On the other hand, the fuel mass flow is determined from the empirical regression rate equation, eq. 2.14, with those coefficients reported previously. Fuel is injected as gaseous butadiene at about 960 K; this temperature has been estimated by means of the Arrhenius law, assuming a low activation energy of 13.35 kcal/mol for HTPB under high heating rates and for a regression rate of 3.58 mm/s [3].

After a preliminary investigation about the most suitable combustion model, the Eddy Dissipation model has been selected as the best compromise between accuracy, simplicity, computational effort, reliability and availability of the information required by the setup. The main assumptions of this model are listed:

- one forward reaction evaluated at stoichiometric OF and expected operative pressure by means of CEA software, so in hypothesis of chemical equilibrium;
- no re-combinations: this aspect can be relevant where local OF ratio is substantially different form the stoichiometric value and chemical kinetics becomes relevant;
- chemical equilibrium shift as a function of OF ratio is not considered;
- reaction rate depends exclusively on turbulent mixing (Damkholer number »1).

Moreover radiation effects has not been taken into account.

Most of the uncertainties and inaccuracies introduced by these assumptions are prominently mitigated when a motor provided by vortex injector is considered: as highlighted in previous section (2.2.1), vortex injection enhance turbulent mixing and then hybrid combustion efficiency, so the motor functioning approaches the ideal performance of chemical equilibrium.

A single step chemical reaction has been used, balanced as follows:

$$14\,H_2O + 5.5\,O_2 + 1\,C_4H_6 \rightarrow 3\,CO_2 + 15\,H_2O + 1\,CO + 1\,H_2 + 1\,O_2 + 1\,OH \qquad (2.16)$$

This equation has been balanced using the NASA CEA code, to identify the most important species (all the species produced by the reaction and having a molar fraction higher than 10^{-3}), in order to obtain a correct flame temperature. The approximation of the eddy dissipation model is justified by the fact that in typical hybrid rockets the limiting rate is the turbulent mixing (fast chemistry).
The main simplifications adopted to describe the H2O2-HTPB chemistry are:

- all the species involved are treated as ideal gases;
- fuel is injected in gaseous state at fixed flow rate;
- simplified chemical reaction, as pointed out previously.

Fluid Geometry Definition

Referring to figure 2.18, it can be seen that the vortex injector is constituted by 2 rows of 10 channels each, one row staggered respect to the other; this characteristics denies the possibility to exploit symmetric or periodic boundary conditions. Because of this injector configuration some drawbacks have arisen: hard and not optimal convergence and high computational cost, in spite of a poor mesh (i.e. big element size) and thus inaccurate results. These considerations forced to follow another strategy: the injector geometry can be simplified according to the hypothesis of uniform ring injection (see figure 2.20b); in fact the injection holes are located very close one to each other on the injection bore surface, as can be observed in figure 2.20a. The thickness of each ring has been calculated such as the equivalent inlet area is the same proper of the 20 holes configuration.

This simplification neglects possible 3D interaction between the channels and velocity non-uniformity on each inlet section but gives axis-symmetry to the geometry. With this setup the direction cosines (d_r and $d_\perp$) have to be assigned: they have been imposed

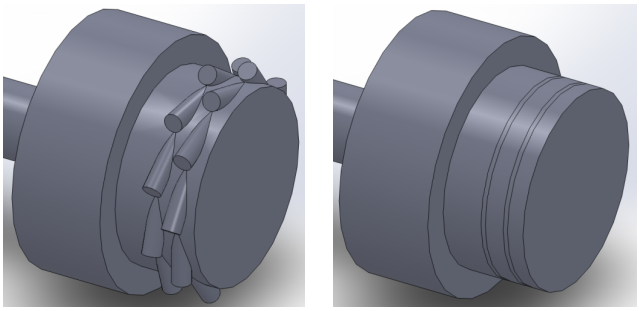

(a) (b)

Figure 2.20: CFD representation of the vortex injector fluid volume: (a) shows the original configuration with 20 channels, while (b) corresponds to the simplified geometry with 2 rings

uniformly equal to the central value of the channel; according to nomenclature reported in figure 2.2, they resulted as follows:

$$\hat{\varphi} = \text{acos}\left(\frac{r_{inj} - r_{port}}{r_{inj}}\right) \tag{2.17}$$

$$d_r = \sin\hat{\varphi} = \frac{v_r}{v_{inj}} \tag{2.18}$$

$$d_\perp = \cos\hat{\varphi} = \frac{v_\perp}{v_{inj}} \tag{2.19}$$

This solution provides a series of advantages:

- there is no need to simulate the injector channels into the CFD model, because inlet condition would be set up in terms of velocity components directly on the rings surface;
- a slice (i.e. a quarter) of the whole geometry can be simulated, applying a rotational periodicity as boundary condition to represent the whole volume;
- thanks to a reduced volume, the mesh refinement can be increased, having a total number of elements comparable with the whole geometry roughly meshed, and thus the same computational cost;
- finally, the forced axial-symmetry imposed by the boundary condition and the fine mesh guarantee a fast convergence and an accurate solution.

According to this new approach, a comparison of the results for a reference case simulated both as a whole geometry and as a section has been performed at first, to assure the goodness of the uniform ring injection hypothesis. Every other setting has been left unchanged. Hereafter some details about the comparison are reported. The comparison refers to the reference case, "C1".

Figure 2.21 reports pressure, temperature, and axial velocity profiles respectively, as colormaps along an axial plane, for the whole geometry case (top) and the section geometry

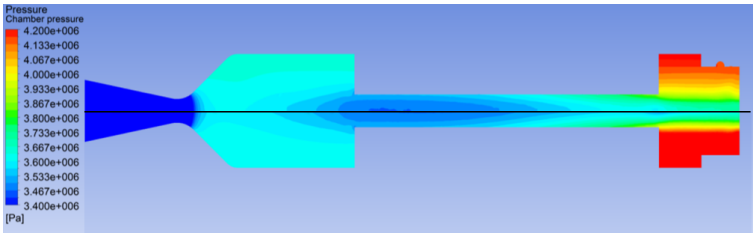

(a)

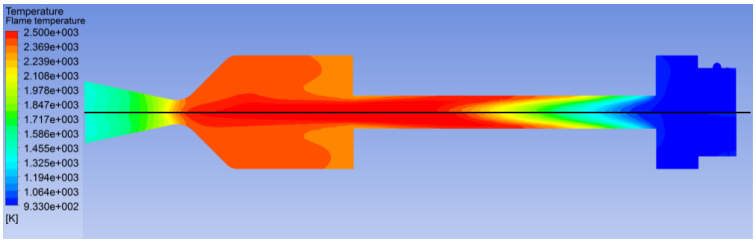

(b)

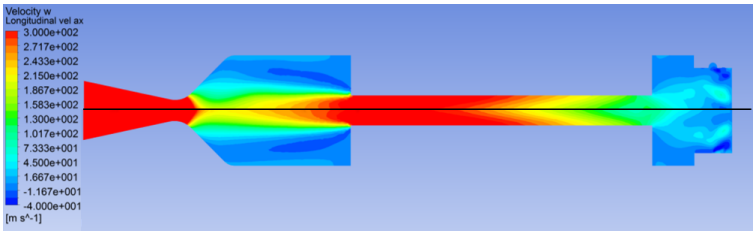

(c)

Figure 2.21: CFD comparison of the the vortex injector representation for the "C1" case: each figure reports the entire geometry case on the top and the section geometry one on the bottom; pressure, temperature and axial velocity colormap are shown respectively in (a), (b), (c)

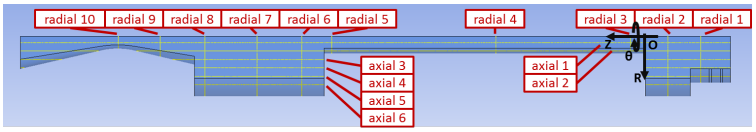

Figure 2.22: Axial and radial lines adopted to plot variables

one (bottom). Ranges have been limited to exclude nozzle effect, and better highlight possible differences upstream the nozzle.
As a start, these results confirm that there are no macro differences between the two simulations.

In the following, the same variables have been compared between the two cases, as plotted curves along specific lines (see figure 2.23); again the effect of nozzle expansion has been excluded. Figure 2.22 reports the locations of the lines selected. Referring to plots of figure 2.23, subscript "s" stands for "section", indicating the quarter slice simulation, while "w" stands for "whole", indicating the whole geometry simulation.

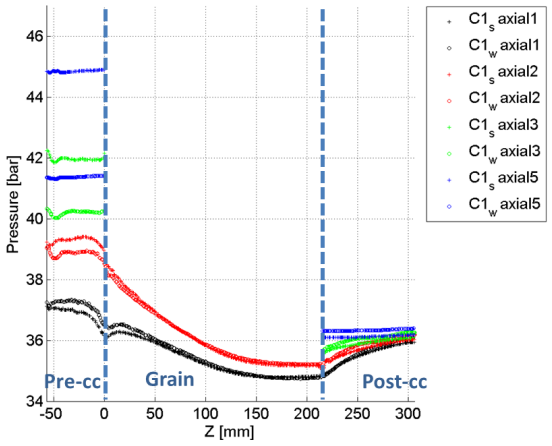

(a)

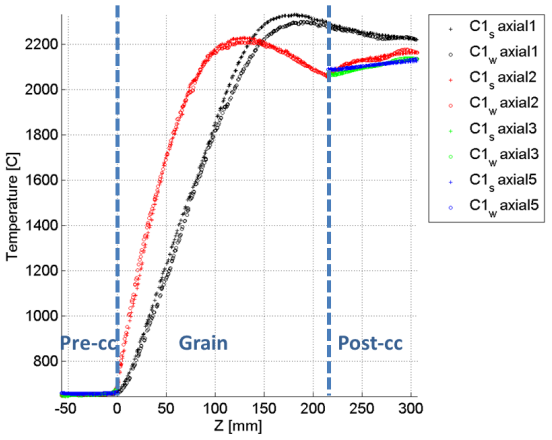

(b)

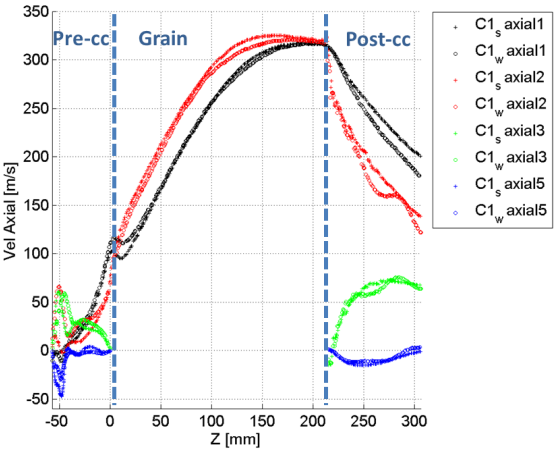

(c)

Figure 2.23: CFD comparison of the the vortex injector representation: figures (a), (b), (c) report respectively pressure, temperature and axial velocity plots along the axial lines defined in figure 2.22

The two simulations exhibit the same trends, with maximum differences under 3%, with the exception of the pressure radial distribution inside the pre combustion chamber: at the maximum radius, the simulation using the ring injection hypothesis overestimates pressure values of about 10%; the main differences observed are at the radial periphery of the pre combustion chamber (axial "3" and axial "5"), because of different centrifugal effects produced by the two different injector representations. These differences however do not affect the behavior of the engine in the inner part of the pre-cc, along the grain and in post-cc as, which remains almost the same in both cases.

Main Results

The main results coming out from this analysis have been validated according to experimental results provided by Nammo [60].

Solutions have been obtained with second order accuracy on equations; to check for achieved convergence, several parameters have been monitored: the simulation has been considered terminated when their values have remained in a ±5% variation range. The variables monitored iteration by iteration have been:

- maximum pressure value;
- mean pressure value;
- maximum temperature value;
- mean temperature value;
- axial velocity in three different axial positions of the volume;
- tangential velocity in the same three different positions tracked for the axial component.

Moreover, at convergence all the residuals had to be below 1e-5.

Respect to the axial-tangential vortex, with a fully tangential vortex, the impingement zone is more narrow, since the oxidizer exits the injector exclusively with a tangential component, and so interaction between jets and flow stabilization take place in the very first portion of the combustion chamber (see figure 2.24). Figure 2.24 shows the streamlines along the motor: as already described, it can be noticed the straightening caused by axial acceleration of the flow, due to mass flow addition, chemical reactions and isentropic acceleration. The flow acquires immediately an axial velocity component, according to continuity equation, and it enters the grain port basically with no radial component due to impingement effect, as it can be seen in figure 2.25 both from velocity vectors (a) and axial and radial velocity components comparison (b). Radial velocity is plotted along an axial line located 1 mm apart from the fuel grain surface (and thus 1 mm far from the imposed boundary condition); it is almost constant along the fuel grain lenght, so it is expected an almost uniform fuel consumption. Velocity vectors are plotted on an axial plane and a detail view is shown on the injection region 2.25a; several recirculation can be distinguished, which can be explained by two different causes: macro-recirculation at the radial periphery are due to sudden change in port section; on the other hand, the compact

recirculation at the motor axis near the injection chamber is due to the already described pressure gradients caused by the vortex motion.

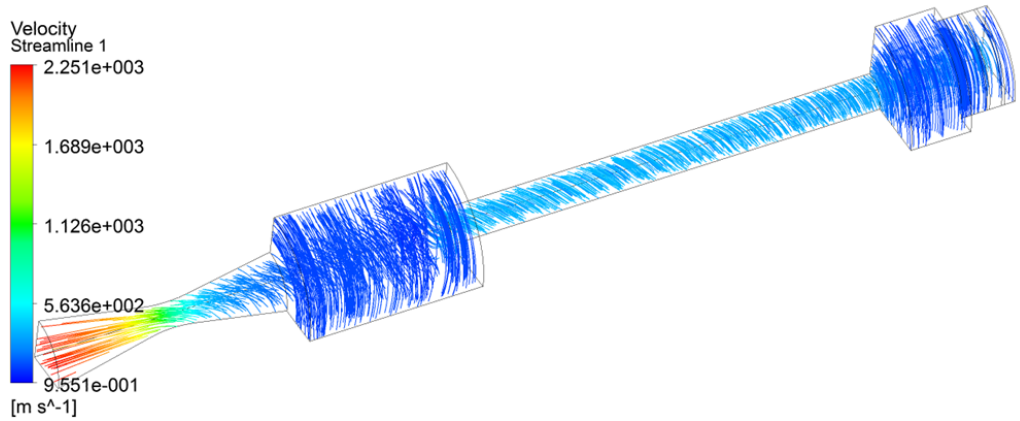

Figure 2.24: Fully tangential vortex streamlines

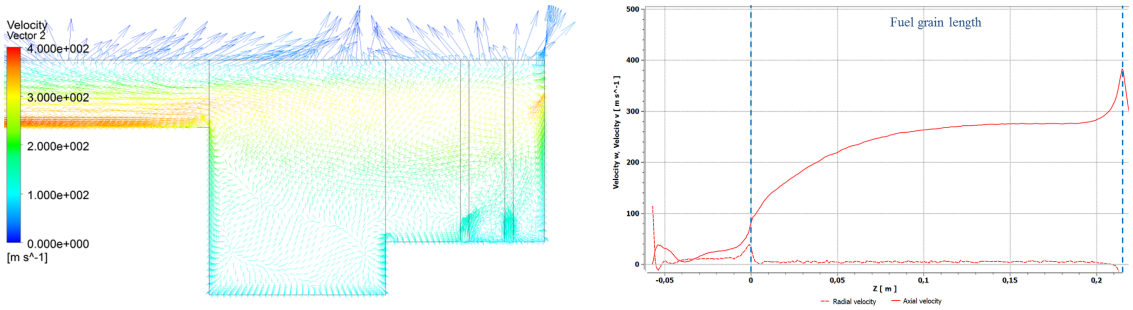

(a) (b)

Figure 2.25: Fully tangential vortex flowfield: detail of the injection velocity vectors (a); axial and radial veocity components along the motor (b)

The characteristic velocity has been calculated, case by case, as resulted from the CFD simulation according to eq. 2.20:

$$c^* = \frac{p_c \, A_{th}}{\dot{m}_{tot}} \tag{2.20}$$

Table 2.7 compares c^* of the reference case "C1" with those of the other cases, to highlight which configuration changes produce an increase of the performance. For the "C1" case a combustion efficiency of 95 % has been calculated.

These results have been combined with the analysis of the swirl number. As described in previous section (see sec. 2.2.1), swirl number can describe the relative intensity of the rotational flow and how it varies along the motor because of heating, friction, mass addition and section changes. Swirl number trends can also give important information about motor performance. So, according to equation 2.2, this parameter has been evaluated at different locations along the motor for each simulated case.

Test case	Peculiarity	$\frac{c^*_{Ci}-c^*_{C1}}{c^*_{C1}}$, [%]
C1	*Reference case*	0
C2	SN_g *doubled*	+2
C3	*Axial-tangential injector*	-2
C4	*Post-cc removed*	-4
C5	*Pre-cc removed*	+3
C6	*Pre-cc and post-cc removed*	-1
C7	*Port diameter at 75% burn time*	+3
C8	$\dot{m}_{ox}$ *reduced at 10%*	+8
C9	$\dot{m}_{ox}$ *reduced at 50%*	+3

Table 2.7: Tangential vortex: combustion efficiency comparison for the 9 cases simulated

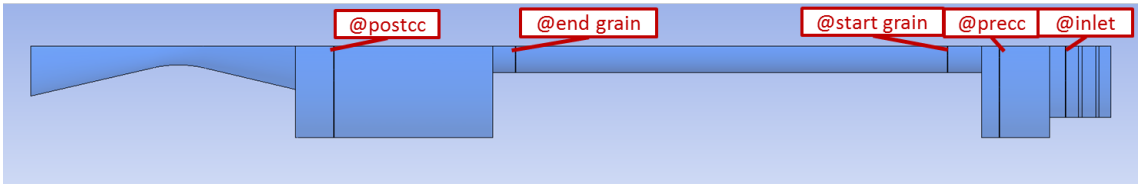

Figure 2.26: Locations adopted to evaluate the swirl number

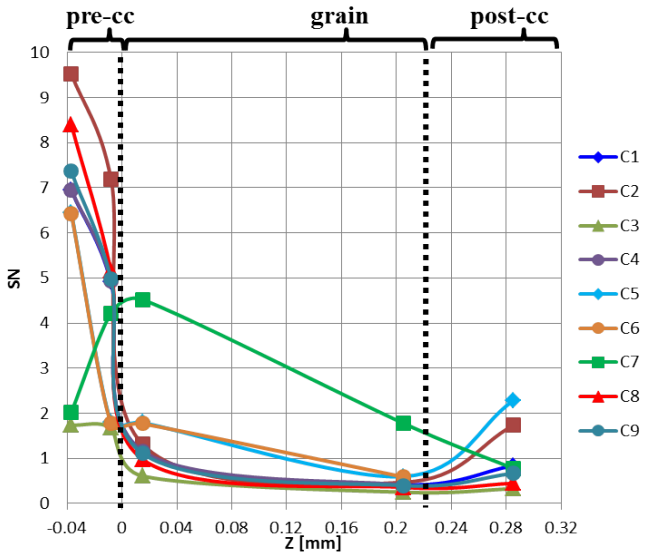

Figure 2.27: Swirl number as a function of axial position for the 9 cases simulated

Figure 2.26 shows the location where the swirl number has been evaluated.

Figure 2.27 reports the swirl number trends for the nine simulations performed, table 2.8 reports the values plotted in fig. 2.27. Swirl number has been calculated in each position as expressed in eq. 2.2, averaging the fluxes over a section plane located in that position.

Test case	**Swirl number**				
	inlet	*pre-cc*	*start grain*	*end grain*	*post-cc*
C1	6.95	4.91	1.16	0.42	0.84
C2	9.53	7.19	1.31	0.47	1.73
C3	1.74	1.67	0.61	0.25	0.33
C4	6.95	4.94	1.16	0.41	-
C5	6.45	-	1.79	0.60	2.28
C6	6.43	-	1.77	0.59	-
C7	2.02	4.22	4.52	1.78	0.78
C8	8.40	5.15	0.98	0.36	0.45
C9	7.36	4.98	1.11	0.40	0.67

Table 2.8: Swirl number as a function of axial position for the 9 cases simulated

As previously noticed (see sec. 2.2.1), friction has a minor effect in reducing the swirling component, while heat and mass addition along the grain cause a large drop of the swirl number, particularly because they force an increase of the axial velocity component.
Every time there is a change in the cross section the swirl number is strongly affected. In fact, considering an incompressible flow, for simplicity, while the axial velocity component changes according to continuity equation, $v_{\parallel} \propto 1/r^2$, the tangential one follows the conservation of angular momentum, $v_{\theta} \propto 1/r$; it follows that: $SN \propto v_{\perp}/v_{\parallel} \propto r$. The CFD results show a strong drop of the SN from the pre-chamber to the port and a recover from the port to the post-chamber, confirming the predicted general trend. However this is only a qualitative statement because of the complex flowfield inside the combustion chamber, affected by strong temperature, density and velocity gradients and three-dimensional recirculations.
Generally, dissipative mechanisms contribute to a decrease of the swirl number. This explains why the computed swirl number slightly changes even if the reference geometrical swirl number remains constant (like in the case of constant geometry). In fact at reduced mass flows the dissipation is reduced so the swirl number results higher. It is worth nothing that dissipative phenomena act in different ways in the axial and tangential directions. In the axial direction they cause a pressure drop (because the velocity is constrained by the continuity equation), while in the tangential direction they induce a decrease of the rotational velocity (because of a loss in the angular momentum). The final result is a decrease in the swirl number.
Considering the different geometries tested a mixed axial-tangential injection, as expected, shows a significant reduction of the swirling flow and consequently of performances.

Doubling the swirl number on the contrary shows the opposite effect. In general higher swirl numbers force higher mixing and consequently lead to higher efficiency. The downside is that a remarkably major pressure gradient in the radial direction settles down in this case; especially in pre-combustion chamber the maximum pressure is increased by 15 % respect to reference case, even though the actual operative pressure down the grain and post-combustion chamber remains almost the same. This aspect represent a major drawback from a system point of view: feed lines operating conditions and combustion chamber case high pressure design.
The suppression of pre-combustion chamber enlargement reduces the dissipation caused by recirculations; in fact, it has been observed that a pre-combustion chamber with a larger cross section respect to the injection bore causes recirculations that weaken the flow. In this case, if the pre-combustion chamber is removed, the specific configuration of the injector guarantees enough length to the flow, downstream the inlet apertures, to stabilize its rotational path before entering the grain port; thus the grain is expected not to suffer nonuniform regression due to impingement effects. It has to be highlighted that the design of vortex injector and pre-combustion chamber is critical: a hybrid motor provided by vortex injector can be potentially extremely compact, but a minimum space must be given to the fluid, downstream the inlet aperture, to stabilize its path before entering the grain port, in order to have the best performances.
The post-combustion chamber, on the contrary, helps the final mixing of the reactants. Even if this effect is less important in the case of the vortex motor, it is still present because the high regression rate allows for shorter fuel grains. Moreover it helps the flow to enter the nozzle without a strong swirling component.
Simulations of throttling down respect to the nominal case have been performed together with a simulation of the same motor geometry but with a larger port area (describing a following instant during combustion). At lower mass fluxes the efficiency is higher because of the increased residence time. Moreover in the case of the large port area the swirl number is preserved because no strong contraction occurs.

2.3 Guidelines for the Experiments

The outcomes of the the numerical investigation just described have been both in terms of performance prediction and useful suggestions for the finalization of the motor design.

As far as the performance prediction is concerned, the main outcomes are:

- a combustion efficiency higher than 95 % is expected, thanks to the effectiveness of vortex injection in mixing the reactants;
- a fully tangential vortex injection is not expected to produce impingement effects in the fuel grain, if a uniform empty volume is left to the fluid downstream the injector channels, in order to stabilize its path before entering the grain;
- the motor is expected to perform at high combustion efficiency even at throttling levels below the nominal one;
- some traces of unburnt propellant can be spotted on the vortex injector, because of the rip-tide effect.

As far as the finalization of the design is concerned, the following suggestions have been derived:

- in order to avoid any possible dissipation effect due to recirculation, the sharp edge between the end of the post-combustion chamber and the convergent part of the nozzle has to be removed: so the front section diameter of the converging part of the nozzle has been fitted to the post-cc diameter;
- since the vortex injection produces pressure gradients in radial direction, which mitigates along the axis, the post-chamber results the most suitable location to measure a representative value of the operative pressure.

Chapter 3

Experimental Setup

UPD has overcome the issues related to handling and storing high concentration hydrogen peroxide integrating the main hybrid motor with a dedicated gas generator, to reproduce 87.5% H2O2 in dissociated condition. The mixture produced inside the gas generator is then injected as oxidizer into the combustion chamber of the hybrid motor. The gaseous mixture is created mixing oxygen and water with a gaseous heat flux produced by a oxygen-polyethylene combustion process; this mixture is expected to get to a temperature around 660 °C (i.e. decomposition temperature of 87.5% H2O2 [58]).

In the following a complete description of the whole experimental setup, in its final design configuration, is illustrated. A complete list of the specifications is also provided.

3.1 Specifications

As already said, the design specification of the lab motor have been identified in the preparatory phase of the SPARTAN project and have not been modified hereinafter, since the main scope of the setup was to validate numerical simulations; thus the most important thing was to have information about all its functioning parameters and conditions, in order to reproduce them in the numerical test case.
The following requirements have been specified:

- functional requirements:
  - the experimental set-up has to be safe and versatile;
  - the test motor has to be operated at fixed-step throttling levels, easily and precisely adjusting each mass flow rate independently;
- performance requirements:
  - stable and constant values of the mass flow rates involved must be guaranteed;
  - the gas generator is expected to reproduce decomposed 87.5% H2O2 as it would result passing through a catalyst; this "simulated" hydrogen peroxide is the oxidizer to be fed to the main combustion chamber; thus the following requirements are needed for the mixture:
    - theoretical mixture temperature achieved: not less than 930 K;

    - theoretical O2 mass fraction: next to 0.41;
    - minimum impurities (i.e. CO2) introduced by the oxygen-polyethylene combustion process;

- diagnostics requirements:
  - the mass flow rates control devices must be reliable;
  - the diagnostic system must allow the evaluation of the following motor performance parameters: c^*, OF, G_{ox}, $\dot{r}$; they can be calculated by means of the following formulations:

$$c^* = \frac{p_c A_{th}}{\dot{m}_{tot}} \tag{3.1}$$

$$OF = \frac{\dot{m}_{ox}}{\dot{m}_{fuel}} \tag{3.2}$$

$$\dot{r} = aG_{ox}^n \tag{3.3}$$

    According to these formulas, the interesting measurements to be acquired during experimental tests are:
    - combustion chamber pressure, p_c;
    - nozzle throat diameter before and after test, A_t, for throat area evaluation and erosion;
    - oxidizer mass flow rate, $\dot{m}_{ox}$, for $\dot{m}_{tot}$, OF and G_{ox} evaluation;
    - fuel grain initial and final diameter, for mean G_{ox} evaluation;
    - fuel grain weight, for average regression rate evaluation: $\dot{r}$;

- vortex injector requirements:
  - the maximum vortex injector pressure drop at nominal mass flow shall be less than 0.2 MPa.

3.2 Test-Bed Design

As can be observed in figure 3.1 the experimental set-up is composed of three main parts:

1. Hybrid Torch (HT), which provides a thermal heat flux to the gas generator;
2. Gas Generator (GG), where the hot gases generated by the hybrid torch mix up with H2O and O2 directly injected into GG, to simulate decomposed H2O2;
3. Combustion Chamber (CC), where the oxidizer mixture created in the gas generator is injected, by means of a vortex injector, and combustion with HTPB fuel takes place.

So the combined functioning of HT and GG produces a mix of gases like decomposed 87.5% H2O2.

This solution allows the possibility to finely control the composition of the oxidizer mixture and its temperature, by regulating the mass flow rates of water and oxygen introduced in the mixing chamber, and the amount of thermal flux provided by HT.

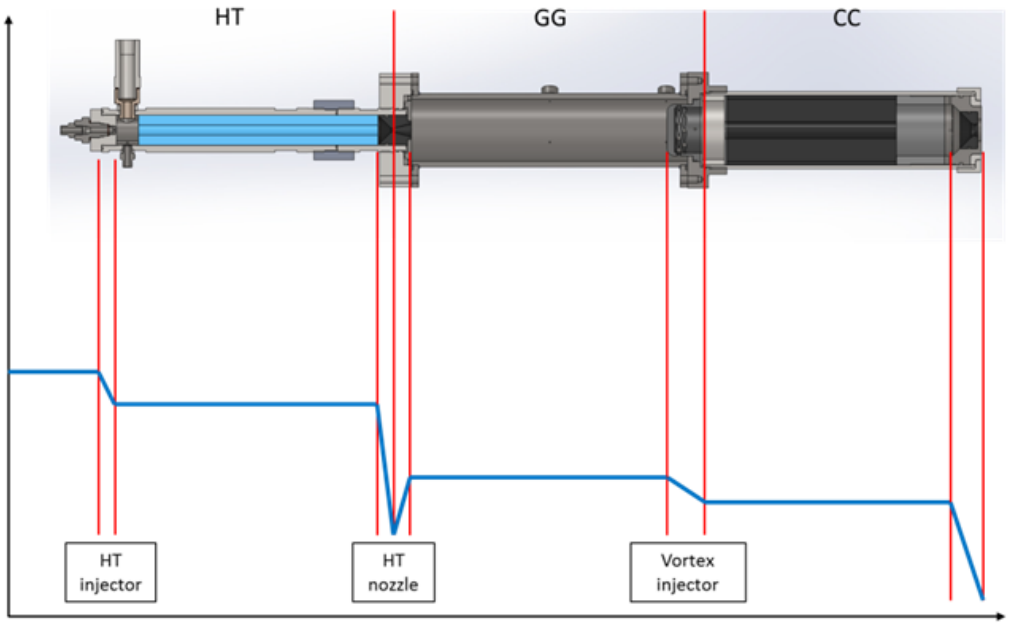

Figure 3.1: Schematic of the hybrid motor assembly

3.2.1 Oxidizer Mixture Composition

Chemical species	87.5% H2O2 before decomposition	Theoretical decomposition of 87.5% H2O2	HT-GG mixture composition before mixing	Theoretical GG mixture composition after mixing
H2O2	87.5%	0%	0%	0%
H2O	12.5%	58.8%	39.1%	44.7%
O2	0%	41.2%	56.5%	41.6%
HDPE	0%	0%	4.4%	0%
CO2	0%	0%	0%	13.7%

Table 3.1: Theoretical decomposition of 87.5% H2O2 vs GG mixture comparison

The theoretical composition of the GG mixture have been deduced by means of chemical equilibrium calculations (CEA), referring to the mean mass flow rates.

The resulting composition of the mixture has been compared with the theoretical decomposition of 87.5%H2O2 (see table 3.1).

The final mass fraction of each mass flow rate has been tailored, in order to obtain after mixing a composition similar to decomposed HP, in terms of oxygen mass fraction. In fact, the main parameter to respect is the percentage of oxygen, since the other gases are almost not involved in the combustion process with HTPB, and so have no relevant

effect on the fuel regression rate in CC.

As can be observed in table 3.1, the resulting mixture contains in any case a slight percentage of impurity, due to carbon dioxide production; this represents however the best compromise between resulting oxidizer temperature, O2 mass fraction and minimum CO2 mass fraction.

The thermochemical software predicted an after mixing temperature of 640 °C, for the theoretical GG mixture reported in table 3.1.

3.2.2 Throttling Functioning

The test-bed is capable of working at different fixed point thrust levels, in order to characterize the performance at different operating conditions.

The thrust modulation is performed through the control of the total oxidizer mass flow rate coming from GG; this means regulating each contribute that enters the GG: gaseous oxygen, liquid water and thermal flux from HT.

HT has to be throttled together with the changing of the motor throttling range, to maintain the mean OF ratio at the optimal value (i.e. the stoichiometric one) in each configuration. To obtain this result, the HT oxygen mass flow rate is adapted consequently, and the grain length too, if needed according to the relation $\dot{r} = f(G_{ox})$ proper of *O2-HDPE*.

As far as the main combustion chamber is concerned, the fuel grain length was decided to obtain an OF ratio equal to 6.5 at nominal oxidizer mass flow, so during throttling it is expected to decrease.

Table 3.2 summarizes the expected mass flow rates, required to obtain the mixture composition illustrated in table 3.1 at the different throttling levels tested.

Throttling level	$\dot{m}_{O2}$ **HT, [kg/s]**	$\dot{m}_{HDPE}$, **[kg/s]**	$\dot{m}_{O2}$ **GG, [kg/s]**	$\dot{m}_{H2O}$ **GG, [kg/s]**
50 %	0.0206	0.0069	0.070	0.063
75 %	0.0310	0.0103	0.105	0.094
100 %	0.0413	0.0138	0.140	0.125

Table 3.2: Nominal mass flow rates at different throttling levels

3.3 Test Bed Main Subsystems

3.3.1 Hybrid Torch

HT is actually a hybrid motor; the oxidizer is GOX, injected into the combustion chamber through a single hole axial injector, and the fuel is HDPE.

Heat flux modulation is performed both regulating the GOX mass flow rate and changing the length of the HDPE grain, if needed, to preserve the optimal OF ratio. As the aim of the hybrid torch is to provide a thermal flux in order to heat up the GG mixture, the OF

ratio is chosen to satisfy the maximum flame temperature requirement, so it corresponds to the stoichiometric value for oxygen and HDPE (i.e. $OF \approx 3$).

These propellants were chosen to get low percentage of impurity (approximately 15% of CO2) in the simulated H2O2 mixture that is injected in the main combustion chamber.

GOX mass flow rate is regulated by means of a De-Laval venturi, with choked throat, located upstream the axial injector; this choice guarantees a constant mass flow rate decoupling the feed line functioning from the downstream behavior, inside the hybrid torch. At each throttling level the venturi upstream pressure is regulated to the desired value with a fast calibration of the pressure regulators.
Further details about the hydraulic circuit are provided in section 3.5. Figure 3.2 reports a schematic of the hybrid torch. A post combustion chamber and a mixer (not shown in figure) have been added at the end of the grain to enhance mixing and thus increase combustion efficiency since a completely reacted and well mixed hot flux is preferred to enter GG.

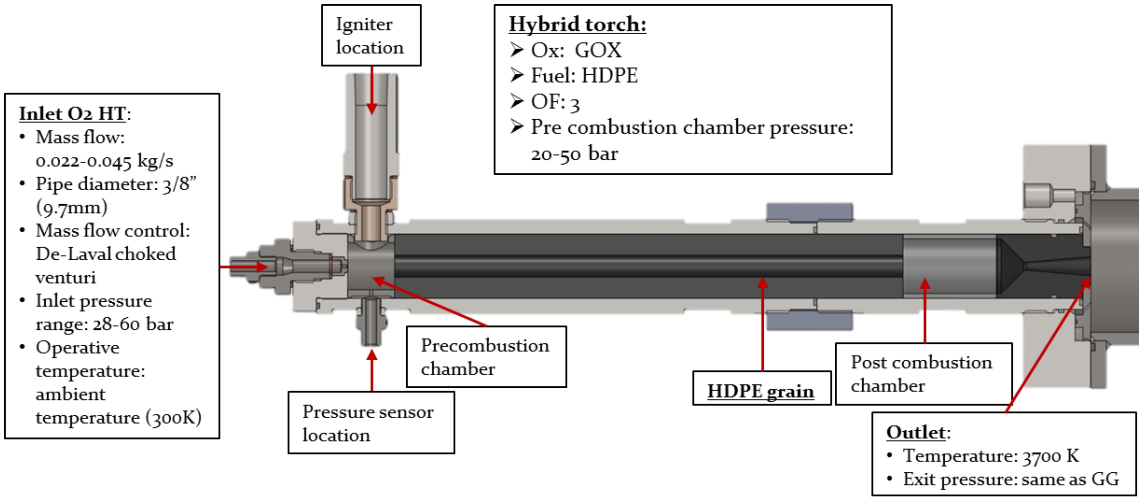

Figure 3.2: Schematic of the hybrid torch

Eq. 3.3 has been used during the design phase, to estimate fuel mass flow rate, and thus grain length, adopting for a and n the following values [59]:

- a=0.132, for $\left[G_{ox} = \frac{g}{cm^2\, s}\right]$;
- n=0.498.

where regression rate results in $[mm/s]$.

Table 3.3 summarizes the design operating conditions, foreseen for the hybrid torch at each throttling level.

A preliminary calibration phase has been performed, to verify the actual dependency $G_{ox} - \dot{r}$ for the hybrid torch, and then adjust the grain length, respect to the design estimation reported in table 3.3. Moreover, additional changes have been implemented to enhance the combustion efficiency, in order to mitigate HT nozzle throat erosion (see section 5.5.1 for further details).

Throttling level	$\dot{m}_{O2}$ HT, [kg/s]	$\dot{m}_{HDPE}$, [kg/s]	Grain length, [mm]	Operative pressure, [bar]
50 %	0.0206	0.0069	330	22.5
75 %	0.031	0.0103	400	35.5
100 %	0.0413	0.0138	460	47

Table 3.3: Reference design parameters for the hybrid torch functioning at different throttling levels

Nozzle is designed to be choked at the throat, but to recover pressure at the outlet, since the main aim of the hybrid torch is to provide a hot mixture; then it would have been useless to convert combustion's thermal energy into kinetic energy.

3.3.2 Gas Generator

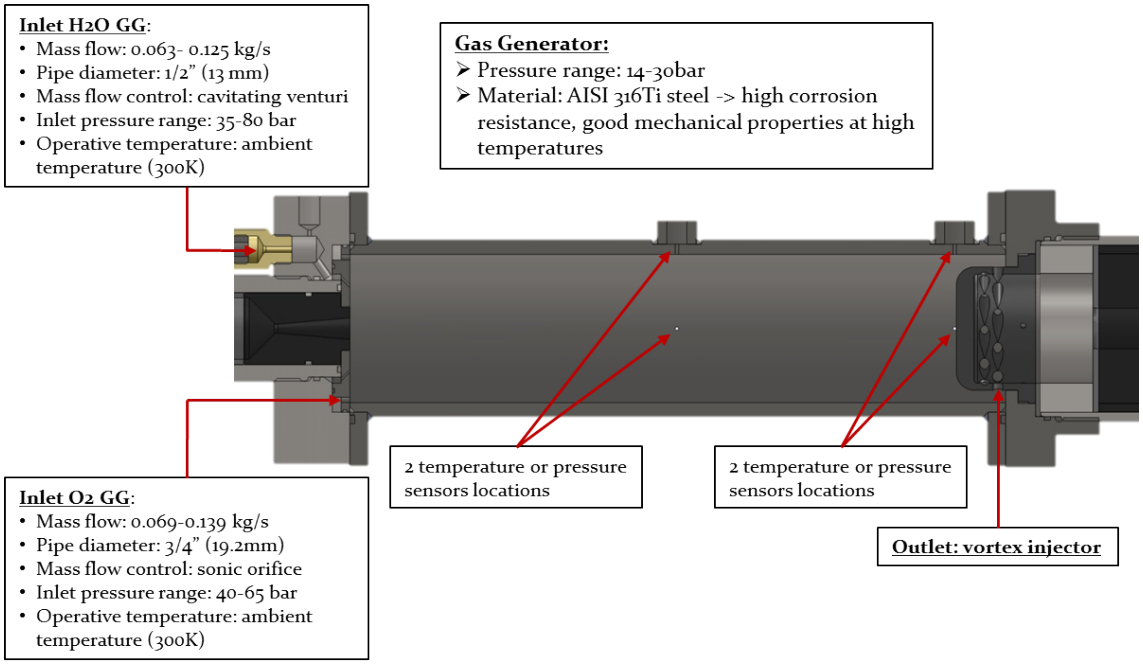

Figure 3.3: Schematic of the gas generator

Figure 3.3 shows a schematic of the gas generator.
GG is a mixing chamber where the hot gases from HT are injected, together with water and oxygen, in order to reproduce a flux of decomposed hydrogen peroxide with a slight amount of impurity ($\sim$ 15% CO2) at the desired temperature ($\sim$ 650 °C).
Temperature is measured using dedicated thermocouples, installed both in the mixing chamber and at the injector inlet of the main combustion chamber.

GG material selected is AISI 316Ti, thanks to its good properties in oxidative ambient at high temperature.

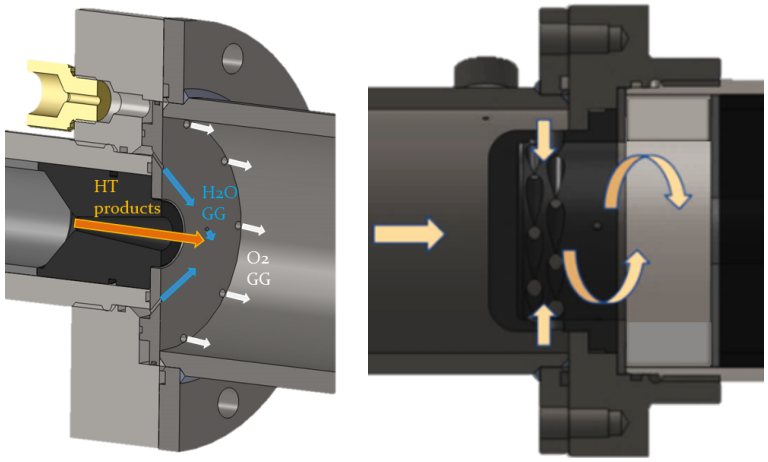

(a) (b)

Figure 3.4: Gas generator inlet and outlet regions: (a) shows the different mass flow rate contributions and the structure of the injection plate; (b) is a zoom on the outlet, which is represented by the vortex injector of the main combustion chamber

Figure 3.4 shows CAD models of GG, zoomed in the inlet and outlet regions.
It can be seen (fig. 3.4a) that the GG injection plate has two separate cavities, to lead water and oxygen separately into the mixing chamber; on the other end, the combustion products coming from the hybrid torch are injected directly inside the mixing chamber, since the injection plate is interfaced directly with HT nozzle outlet.
The injection channels assigned to water are tilted radially, to spray water directly towards the hot flame coming out from the hybrid torch nozzle. The cavity for water has been located around the HT nozzle aperture with the aim of mitigating the heating up of the nozzle itself, and thus throat erosion. Experimental evidence has confirmed the effectiveness of this solution, since a couple of tests where the O-ring fails to prevent water from evacuating outside the flange have shown a more serious throat erosion.
The outlet section correspond to the vortex injector inlet: figure 3.4b shows the path, followed by the mixture passing from GG to CC. As the net cross section available to the mixture to exit is small, it is expected that the chemical recombination, heating and mixing up processes of the mixture are completed when the mixture passes through the vortex injector, being forced to turbulently mix in correspondence of GG outlet.

The design process of the GG mixing chamber has been supported by CFD analysis, to have preparatory information about the internal behavior of the oxidizer mixture prior being injected in the main combustion chamber.

Thrust modulation is performed regulating both the GOX and H2O mass flow rate, besides the heat flux from HT; both the GOX and H2O feed line are provided by chocked orifices: a sonic orifice and a cavitating venturi respectively, so the mass flow rate regulation is accomplished setting the upstream pressure properly.

Preliminary tests of HT-GG coupled functioning have been performed, to verify the actual temperature, reached by the mixture. As expected, because of several factors, such as thermal dispersion and mixing inefficiency, the actual mixture temperature resulted lower than the predicted theoretical value; as a result, the heat flux provided by the hybrid torch has been slightly increased, respect to the design value, to compensate this issue. The reader is referred to section 5.5.1 for further details.

3.3.3 Combustion Chamber

Finally, CC is the main combustion chamber. In figure 3.5, a schematic of CC is pictured.

It burns HTPB as fuel; fuel grains were produced and provided by Nammo Raufoss AS, a partner of the SPARTAN project. The grain is casted into a phenolic tube. All the grains had an initial port diameter of 34 mm and a length of 230 mm. Figure 3.6 shows an example of a HTPB grain.

The length of the HTPB grain was decided to obtain OF ratio equal to ~ 6, at 100% throttling level.

The oxidizer mixture produced inside GG is injected in the main combustion chamber through a fully tangential vortex injector with 20 holes, located into two rows. The injector for the UPD motor is not intended to be representative of the flight motor: it is suitable for the experimental hardware produced by UPD, so it has been designed for the involved mass flow rate and pressure drop.

The main combustion chamber comprehends also a pre- and a post-combustion chamber. The combustion products expand through a nozzle, which the divergent part has been removed to, for acoustic noise mitigation. Because of nozzle truncation, the effective thrust produced is lower than the corresponding design value.

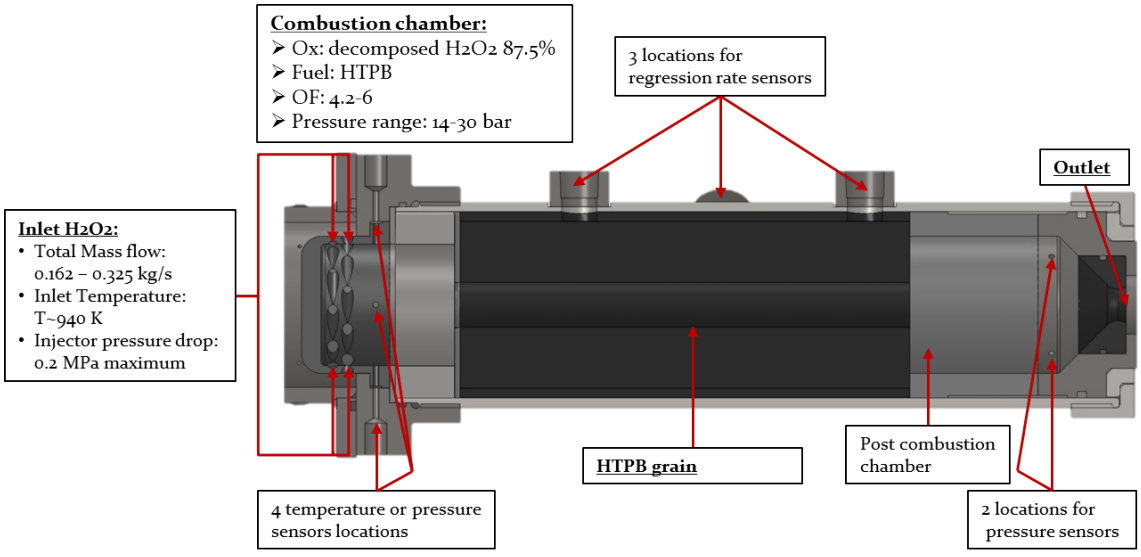

Figure 3.5: Schematic of the combustion chamber

The fully tangential vortex injector is shown in figure 3.7a, while figure 3.7b clarifies the nomenclature adopted to describe a vortex injector.

(a) (b)

Figure 3.6: HTPB grain, provided by Nammo Raufoss AS: before (a) and after burn (b)

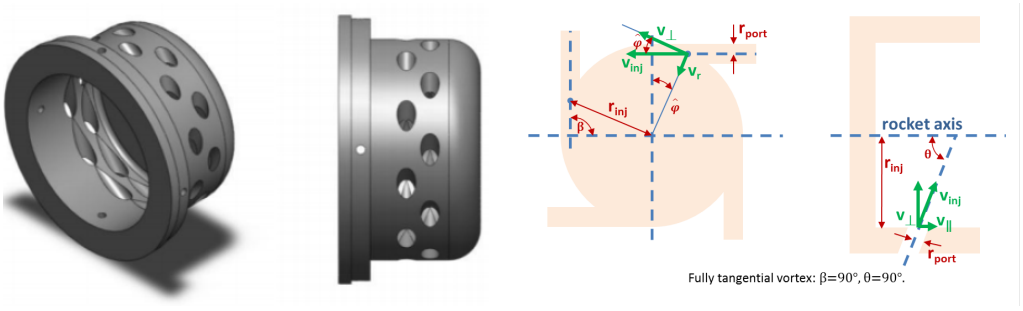

(a) (b)

Figure 3.7: Vortex injector schematic (a) and nomenclature (b)

Preliminary design of vortex injector was performed according to indications provided by Nammo Raufoss AS. The diameter and the number of the holes were calculated according to the maximum required pressure drop at nominal oxidizer mass flow and the desired geometrical swirl number, $SN_g \sim 4.5$ (see eq. 2.1).

In depth study has been performed about vortex injection by means of CFD tool, to understand its peculiarities; according to these analysis, it was expected from the beginning to have high performance at each throttling level. The reader is referred to chapter 2, for details about the numerical investigation performed.

In the design phase, motor mean performance (G_{ox}, OF, c^*) have been estimated thanks to equation 3.3, with the following values for the parameters a and n:

- a=0.07, for $\left[G_{ox} = \frac{kg}{m^2 s}\right]$;
- n=0.62;

where regression rate results in $[mm/s]$.
These values were provided to UPD by Nammo Raufoss AS, according to its experimental results, performed on a similar motor configuration, both in terms of injector geometry and selected propellants [60].

Table 3.4 summarizes the expected behavior of CC, according to the design calculations.

Throttling level	$\dot{m}_{tot}$ **GG, [kg/s]**	$\dot{m}_{HTPB}$, **[kg/s]**	**Grain length, [mm]**	**Mean OF**	**Operative pressure, [bar]**
50 %	0.1605	0.037	230	5.8	25
75 %	0.2403	0.047	230	5.1	20
100 %	0.3201	0.056	230	4.3	15

Table 3.4: Reference design parameters for the combustion chamber functioning at different throttling levels

3.4 Test Bench

A new test bench has been designed and manufactured, to replace the previous one.

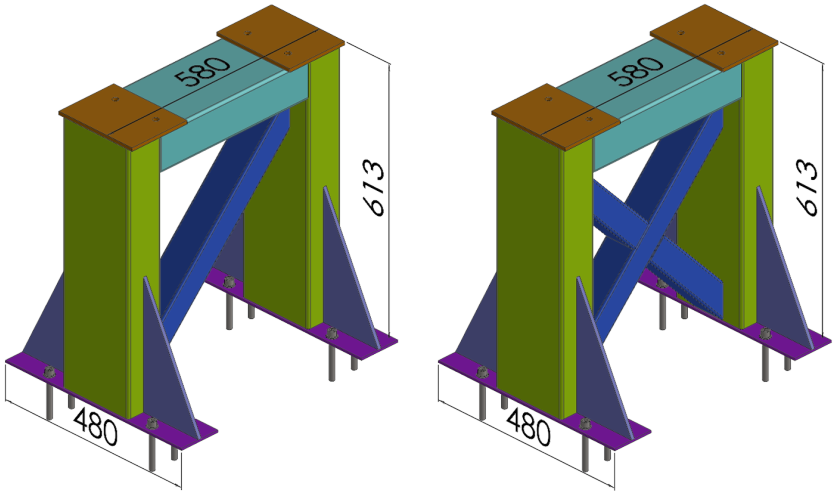

(a) (b)

Figure 3.8: UPD test bench for lab-scale motors testing: CAD schematic of the preliminary version(a) and final version (b); total sizes are shown in [mm]

The requirements which have driven to build a new test bench have been:

- to have a compact test bench, in terms of total size of the structure, designed to stand loads produced by lab scale motors (i.e. up to 3 kN);
- to design a stiff test bench, whose modal frequencies are not less than 100 Hz: so the thrust measurement is not affected by spurious vibration, proper of the bench and excited by the motor functioning, in the range $[0, 100]\,Hz$.

Moreover it has been mandatory to use off-the-shelf beams as basic components of the structure, to mitigate costs. Box beam and I beam based structured have been investigated but finally, a box beam based one has been developed. The choice of box beam components limits the total weight of the structure.

The design phase has been performed by means of FEM analysis. The basic idea has been to realize an architrave based structure, with two bearing columns and some additional components to reinforce the structure and increase the first modal frequencies. All the structural components are to be welded together to form a unique and indivisible structure.
A preliminary version has been reinforced with a transverse beam and 4 gusset plates; this configuration is shown in figure 3.8a; the total sizes are also shown. The modal analysis performed by means of the mechanical solver provided the modal frequencies reported in table 3.5, while figure 3.9 shows the corresponding modal vibrations, comparing the deformed to the undeformed shape.

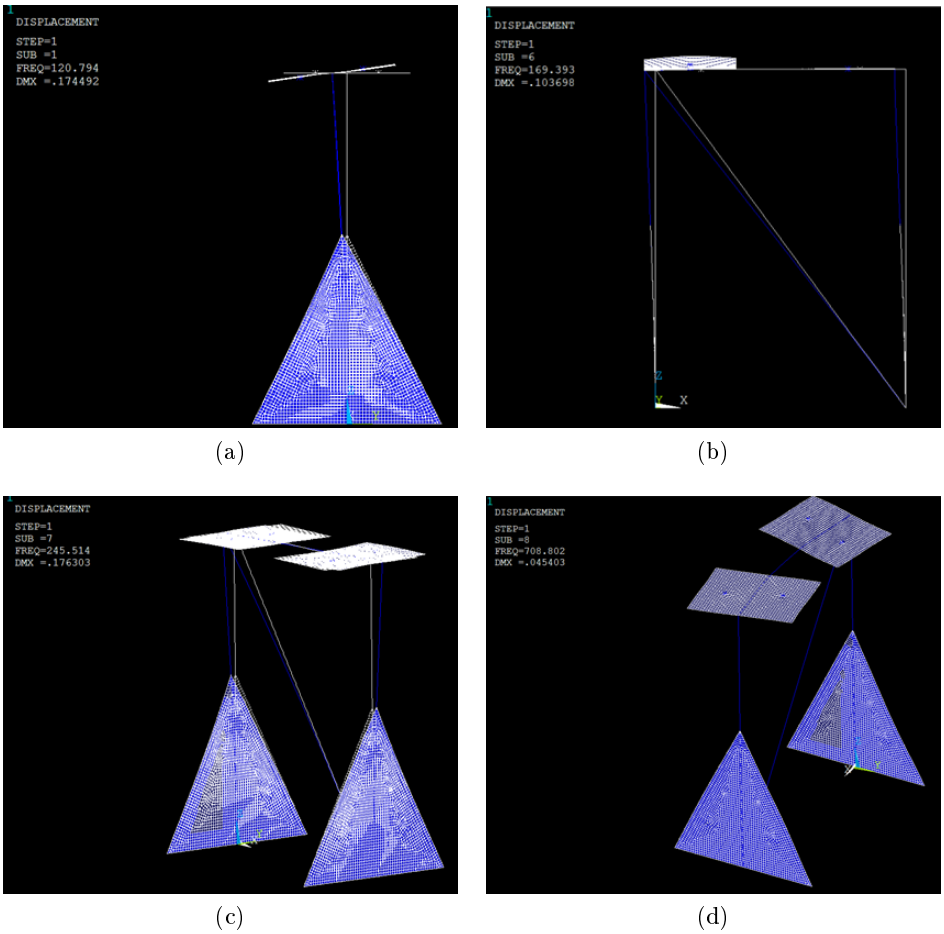

(a) (b)

(c) (d)

Figure 3.9: Modal vibrations of the UPD test bench: deformed vs undeformed shape, corresponding respectively: (a) to *Mode # 1*, (b) to *Mode # 2*, (c) to *Mode # 3*, (d) to *Mode # 4*

Mode	**#1**	**#2**	**#3**	**#4**
Frequency, [Hz]	121	169	246	709

Table 3.5: Modal frequencies of the UPD test bench, as estimated by FEM analysis

Respect to the preliminary configuration, which however would have satisfied the requirements, a further reinforcement has been added to get to the final configuration, as can be seen in figure 3.8b: a second transverse beam, mounted in the opposite direction respect to the first one. As expected, this change has caused a further stiffening of the entire structure, increasing the modal frequencies of about 200 Hz.
This test bench is fixed to the ground by means of 8xM12 screws, as shown in figure 3.8.

3.4.1 Motor Mounting Configuration

The interface between the test bench and the motor assembly has been kept unchanged respect to the previous design, for convenience. It is constituted by a mounting plate, conveniently connected both to sustain the motor assembly weight and to transmit the thrust load from the motor to the thrust measurement system. It has to be highlighted that the thrust measurement has never been used in this work, because unnecessary.

Figure 3.10 shows the whole assembly, composed by:

1. test bench;

2. thrust measurement system;

3. mounting plate.

As it can be observed, the mounting plate is not directly connected to the test bench: two linear guides are mounted horizontally above the test bench by means of dedicated supports; along these linear guides, two low friction runners can slide. The runners are connected directly to the mounting plate, thus the assembly *test bench-linear guides-runners-mounting plate* causes the plate to be able to slide respect to the fixed test bench.

Thrust can be measured by means of a traction load cell, connected on one side to the fixed test bench and on the other side to the mounting plate, by means of ball joints . Figure 3.10b shows the interfaces of the load cell both to the test bench and to the mounting plate.
The motor is supposed to be mounted above the sliding plate.

The motor mounting solution foresees two rigid connections, attached to the gas generator closing flanges on one side and to the mounting plate on the other side. They are constituted by reinforced slices of off-the-shelf L-section bars.
Appropriate structural verification has been performed for the connection bolts to shear stress.
Figure 3.11 shows the motor assembly, mounted on the test bench through the sliding plate, and connected to the load cell

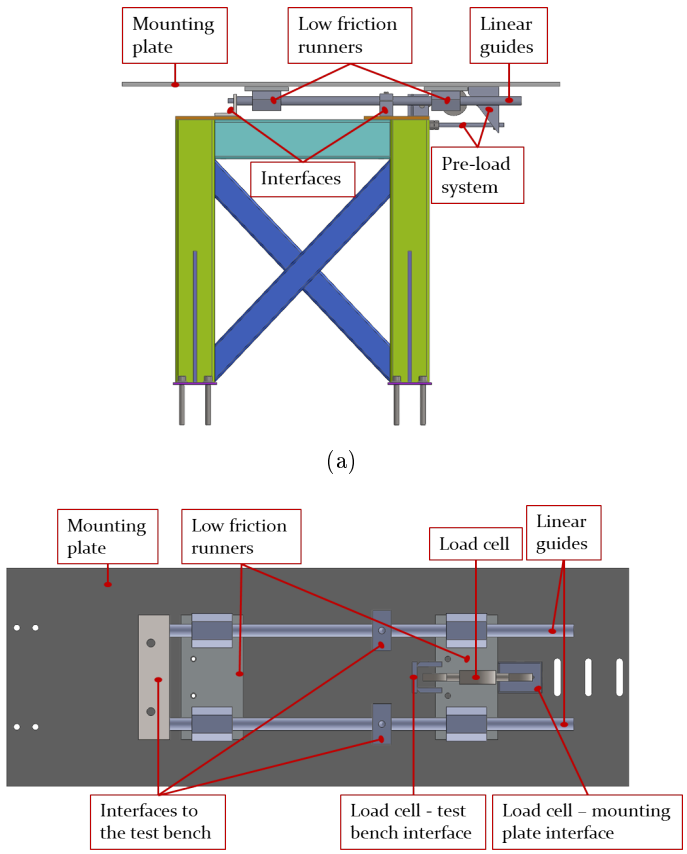

Figure 3.10: UPD test bench for lab-scale motors testing: CAD schematic of the preliminary version(a) and final version (b); total sizes are shown in [mm]

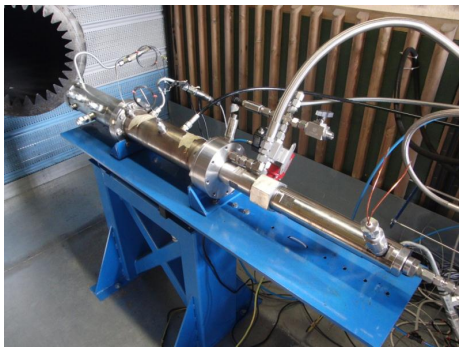

Figure 3.11: Motor assembly mounted on the test bench

3.5 High Pressure Plumbings

The circuit is constituted by three different feed lines:

- line 1, oxygen for hybrid torch: O2 HT;

- line 2, oxygen for gas generator: O2 GG;
- line 3, water for gas generator: H2O.

Figure 3.12 reports the hydraulic and pneumatic scheme of the circuits for the Gas Generator and Spartan lab motor.

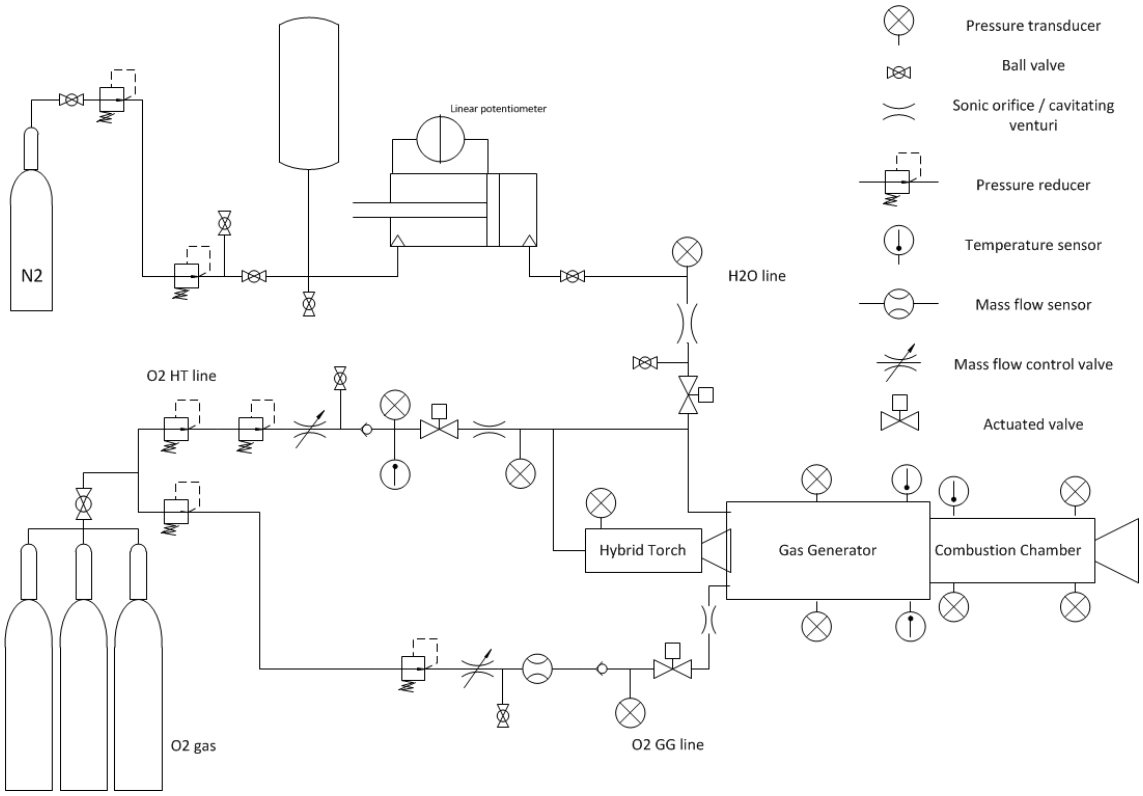

Figure 3.12: Experimental setup: hydraulic and pneumatic circuit

The oxygen is provided by a group of commercial tanks at 200 bar: up to 7 tanks are connected together as a unique oxygen reservoir. The main pipe is branched into two lines (O2 GG and O2 HT) before the first stage pressure regulators (one for each line); the first stage regulators are responsible for the most part of the pressure drop: nominally, they reduce the downstream pressure to the [50 80] bar range.
Downstream the first stage, each line is composed by:

- flexible pipe;
- second stage pressure regulators, to reduce the pressure at the desired operative value;
- needle valve, to perform a pressure fine tuning;
- check valve for safety reason;

- on-off pneumatic ball valve, electronically actuated in remote mode, to start and stop oxygen flow;
- sonic orifice, to settle the dependency of the oxygen mass flow rate uniquely from the upstream pressure;
- several sensors.

Both O2 lines are provided by a sonic orifice, to set the mass flow rate at the design value: their aim is to keep the mass flow rate independent from the downstream pressure, since in their throat the sonic condition is reached.
The governing equation for this kind of device is eq.4.1, applied to the choked section of the orifice, A_{so}:

$$\dot{m}_{O2} = C_d A_{so} \sqrt{\frac{k}{R_g}} \frac{p_0}{\sqrt{T_0}} \left(\frac{2}{k+1} \right)^{\frac{k+1}{2(k-1)}} \tag{3.4}$$

Thus, once defined the fluid (and thus: k, R_g, T_0) and the orifice geometry (and thus: A_{so} and C_d), the only parameter to act on is the upstream total pressure, p_0.

HT orifice is a converging-diverging nozzle, while GG orifice is a simple sonic one, for construction constraints.

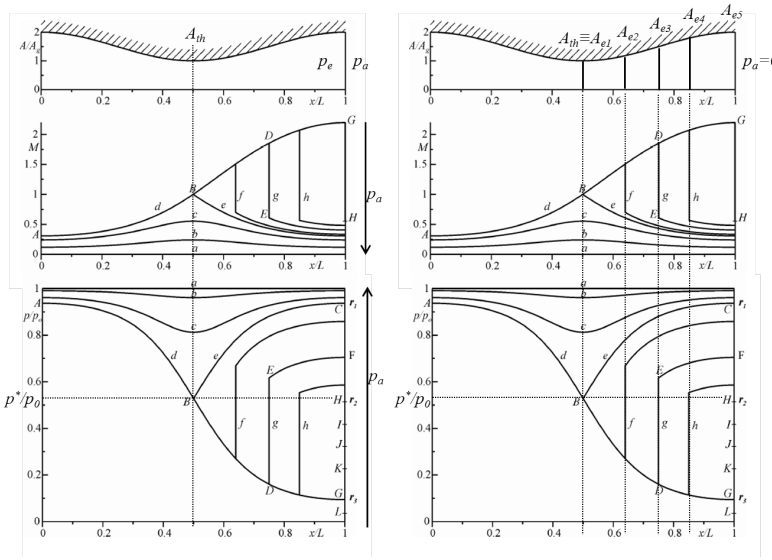

Figure 3.13: De-Laval nozzle possible operating conditions: the left scheme shows flow characteristics as a function of ambient pressure, downstream the nozzle exit, for a given geometry; the right scheme represents the dependency of flow characteristics on the expansion ratio (A_e/A_{th}), neglecting downstream pressure influences

Referring to figure 3.13, the HT orifice has a wider range of acceptable downstream pressure (p_a), because the orifice is provided by a diverging part downstream the throat ($A_e > A_{th}$): so the downstream pressure can largely exceed the choking value (p^*), up to the "C" condition in figure. On the contrary, the GG orifice can operate in choking conditions only if the downstream pressure is below the choking value, since $A_e \equiv A_{th}$. For

this reason, considering the operative pressure in GG ($p_a = p_{GG}$)at each throttling level, two orifices with different throat section have been needed for O2 GG pipeline, to cover the required mass flow rate range; a smaller orifice for the 50% and 75% throttling levels, and a larger one for the full throttling level. The driving constraints in designing them have been: the upstream pressure, p_0, was not to exceed *70 bar*, for safety and economic reasons, but should be enough high to guarantee the choked functioning of the orifice at any required mass flow rate, considering the operative downstream pressure imposed by GG-CC functioning.

As far as H2O line is concerned, it is pressurized by a piston-tank: one side of the tank is filled with nitrogen at the desired pressure, while the other side is filled with water: water flows in blow-down mode, and for this reason the pressurization volume has been enlarged using a reservoir connected with the upstream section of the piston-tank (see scheme in figure 3.12).

The water mass flow is controlled by a cavitating venturi.
Figure 3.14 shows the CAD drawing of this device. Convergent and divergent cone angles have been deduced from typical values traceable in literature [61]. The design phase has been supported also by CFD simulations of cavitation: in particular, the maximum downstream pressure which guarantees cavitation at the throat has been deduced. Figure 3.15 shows an example of the CFD results: vapor volume fraction is reported; cavitation takes place in correspondence of the throat section where pressure gets down to the saturation value.

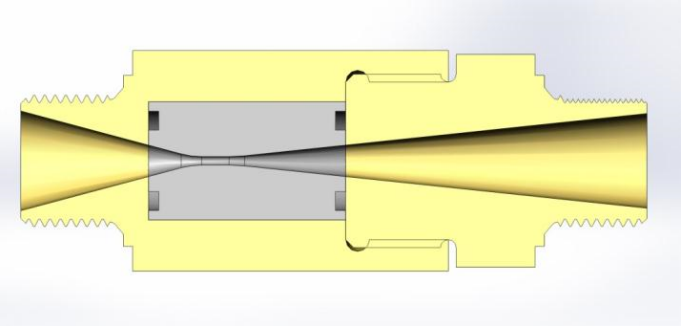

Figure 3.14: CAD drawing of the cavitating venturi designed

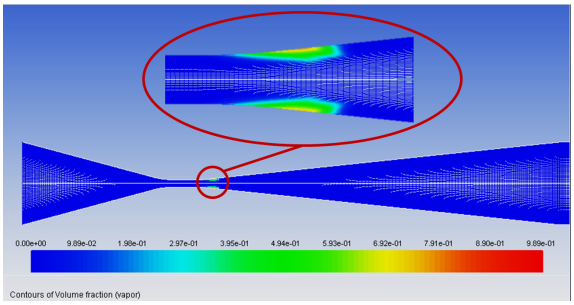

Figure 3.15: CFD simulation of the cavitating venturi functioning. The vapor volume fraction is shown.

The formulation, that describes the cavitating venturi behavior, is as follows:

$$\dot{m}_{h2o} = C_d A_{cv} \sqrt{(2\rho\,(p_i - p_{sat}))} \tag{3.5}$$

where the discharge coefficient, C_d, has been assumed equal to *0.94*, during the design phase, according to [61]

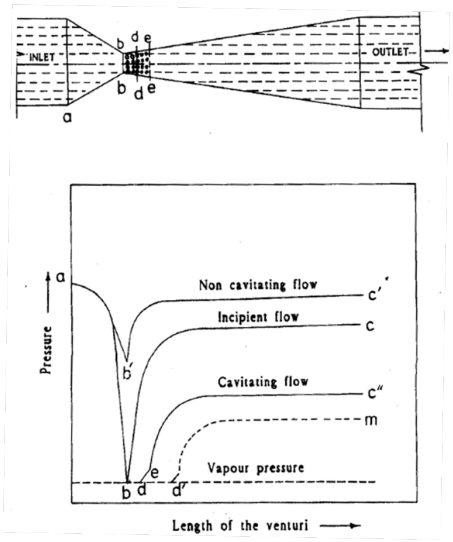

Figure 3.16: Cavitating venturi typical functioning: flow characteristics as a function of ambient pressure and throat length, for a given throat diameter

Referring to figure 3.16, [62], pressure decreases in the converging section and increases in the diverging one. Below a certain value of downstream pressure (i.e. ambient pressure outside the divergent part of venturi), the acceleration of the fluid towards the throat is such that vapor pressure is reached: this is the incipient cavitation condition. With further reduction of downstream pressure, two phase condition extends: this is the cavitating flow condition. Extending the throat length, cause the cavitation to extend, too. Vapor bubbles collapse further downstream and the flow becomes single phase again.
So, if the cavitation at the throat section is guaranteed, as for the oxygen sonic orifices, even in this case the mass flow rate is decoupled from downstream phenomena and it can be controlled acting on the upstream pressure, p_i (see eq. 3.5).

Since the throttling range of the water mass flow rate is sensibly wide, it has been impossible to use one single venturi for all the foreseen mass flow rates: two different venturi diameters have been designed; a smaller one for the 50% and 75% throttling levels and a larger one for the 100% one. The driving constraints in designing them have been: the upstream pressure, p_i, was not to exceed *80 bar*, for safety reasons, since the tank has been designed for this maximum operative pressure; but should be enough high to guarantee cavitation in the throat section, considering the operative downstream pressure imposed by GG-CC functioning.
Considering figure 3.14, the cavitating venturi has been designed as an assembly of three parts: most of the convergent and divergent portions are part of two always usable peaces, while the central throat is constituted by an interchangeable insert. This solution has

allowed to save some money, since cavitating venturi manufacturing resulted expensive. Small changes of the throat diameter respect to the design value would have caused intolerable changes in the required upstream operative pressure; thus, strict dimensional tolerances have been required in manufacturing the venturi throat inserts, as reported in figure 3.17. These order of tolerances have forced to produce them by EDM, which is an expensive technique.

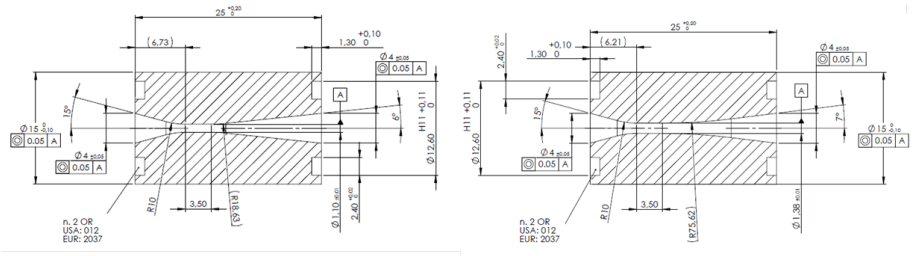

Figure 3.17: Drawings of the two cavitating venturi inserts with the required manufacturing tolerances: the smaller one for the 50% and 75% throttling levels (left) and the larger one for the 100% one (right)

Finally, table 3.6 summarizes the characteristics of the orifices adopted for mass flow rate control on the three feed lines.

	O2 HT feed line		**O2 GG feed line**		**H2O GG feed line**	
	Orifice type	**Throat diameter [mm]**	**Orifice type**	**Throat diameter [mm]**	**Orifice type**	**Throat diameter [mm]**
50% throttling	conv-div	2	conv	3	cavitating	1.1
75% throttlingl	conv-div	2	conv	3	cavitating	1.1
100% throttling	conv-div	2	conv	3.7	cavitating	1.38

Table 3.6: Characteristics of the orifices adopted for mass flow rate control on the three feed lines

Chapter 4

Measurement System

4.1 Diagnostics Apparatus

A complete array of sensors has been designed and installed, to perform a complete analysis of the developed performance during the operative phases, so all critical aspects of the motor functioning are investigated. In particular, the diagnostics apparatus can monitor the following parameters:

- water mass flow rate;
- GG oxygen mass flow rate;
- pressure, at several locations along the three feed lines;
- pressure, in correspondence of the different chambers: hybrid torch, gas generator and main combustion chamber;
- temperature, at certain locations along the feed lines, to monitor oxygen and water temperature;
- temperature at GG outlet and CC injection;
- thrust.

HT and CC fuel mass flow rate are derived as mean values, weighting fuel grains before and after each test.

Even though, O2 GG mass flow rate can be derived from the sonic orifice upstream pressure, once the discharge coefficient has been estimated (see eq. 3.4), the O2 GG line is provided by a further instrument to doubly check the mass flow rate measurement: a Coriolis mass flow meter.

In the same way, a double check is performed also for water mass flow rate: it can be evaluated with eq. 3.5, once estimated the discharge coefficient; but it can also be derived from the time-varying signal of volume occupied by water. This information is provided by a linear potentiometer, connected to the sliding piston of the water tank, which measure the instantaneous displacement of the piston and thus the mass discharged. Sections 4.3 and 4.4.2 provide additional information about this measurement derivation.

Finally, GG mixture temperature is foreseen.

A preliminary analysis has been conducted to select the most suitable instrument. Section 4.2) reports this analysis.

Several locations are available for mounting the temperature measurement devices, both in the gas generator chamber and at the vortex injector inlet; figure 4.1 shows the mounting positions available.

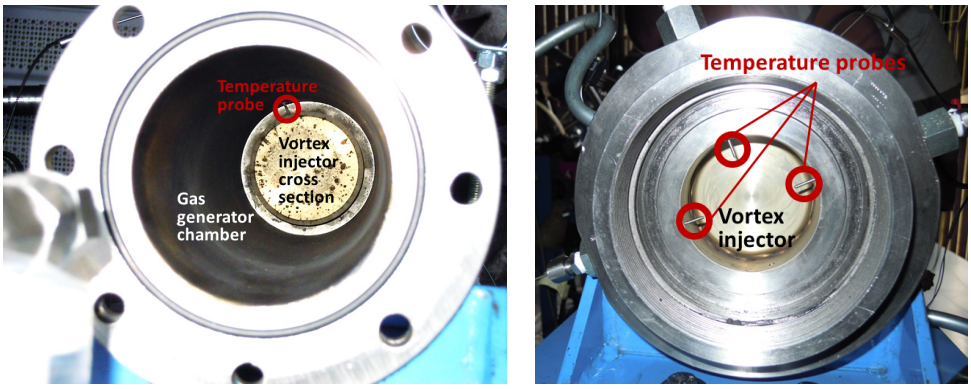

(a) (b)

Figure 4.1: Thermocouples mounting locations: (a) inside the gas generator chamber, immediately upstream the vortex injector; (b) inside the combustion chamber, immediately downstream the vortex injector holes

Signals are acquired using a custom sensor amplification PLC system and A/D converter: 1kHz maximum sampling frequency, 250 Hz maximum sensors bandwidth. The acquisition system can also perform automatic control of actuating valves and time-scheduled operations with a minimum time step of 1ms.
The complete list of sensors and instruments is reported in table 4.1 and 4.2, for the feed lines and the motor assembly respectively.

4.2 Oxidizer Temperature Measurement

A time-varying temperature measurement inside GG is required for two main reasons:

- to assure the structural integrity of the chamber case, subjected to thermal loads;
- to track the mixture temperature: HTPB ignition capability can be inferred from this information; moreover, mixture temperature trends as a function of time provide useful indication about the mixture composition, in order to guarantee a repeatable composition test by test.

Since the mixture is the result of both turbulent mixing and chemical recombination between different flow rates it is possible that it is still reactive when facing the temperature measurement device; moreover, among the species composing the final mixture, oxygen is a major component so the device is required to withstand an oxidizing ambient.

Table 4.1: Diagnostic apparatus of the three feed lines

	Objective	Requirements	Sensor/ instrument	FS	Accuracy (% FS)
O2 HT	Oxygen pressure regulator	Pin: 0-200 bar; Pout: 0-100 bar; Max mass flow: 1200 Nm^3/hr Nominal mass flow: 144 Nm^3/hr	R 300 HE		
	Pressure upstream sonic orifice		Gefran TK	100 bar	0.25
	Pressure downstream sonic orifice		Gefran TK	100 bar	0.25
O2 GG	Oxygen pressure regulator	Pin: 0-200 bar Pout: 0-100 bar Max mass flow: 1200 Nm^3/hr Nominal mass flow= 540 Nm^3/hr	R 300 HE		
	O2 GG mass flow meter	PN: 100 bar Mass flow range: 18-180 g/s	Coriolis flow meter Micro Motion F	0.18	0.09
	Pressure upstream sonic orifice		Gefran TK	100 bar	0.25
	Pressure downstream sonic orifice		Gefran TK	100 bar	0.25
H2O GG	Tank pressure, N2 side		Gems 2200	250 bar	0.25
	Tank pressure, H2O side		Gefran TK	100 bar	0.25
	H2O mass flow meter	Mass flow range: 15.6-156 g/s Accuracy: 0.25% RDG	Magnetic flow meter, Rosemount 8700 Transmitter Rosemount 8732	0.156	0.25
	Pressure downstream on-off valve		Gefran TK	100 bar	0.25
	Linear potentiometer	Displacement force: < 25 N	Gefran LT	400 mm	0.05%

Table 4.2: Sensors dedicated to the motor assembly diagnostics

	Measure	Sensor	FS	Accuracy (% FS)	Frequency response
HT	Pre cc pressure	Kistler 4260A	70	0.05	2kHz (-3dB)
GG	Pressure	Gefran TK	60	0.25	
	Outlet temperature	TC-J	760		
CC	Pre cc pressure	Kistler 4260A	70	0.05	2kHz (-3dB)
	Post cc pressure	Kistler 4260A	70	0.05	2kHz (-3dB)
	Injection temperature	TC-J	760		

A survey has been conducted among different types of temperature measurement devices off-the-shelf, to identify the best candidate for this application; two macro-categories have been considered since they are the most diffuse in industrial applications for their good compromise between cost-accuracy-versatility: thermocouples and resistance thermometers. Once their main characteristics have been outlined, the device to be used has been selected according to predefined requirements and constraints. A description of the conducted survey is reported in appendix 6.

Then, a dynamic characterization of the selected temperature measurement device has been performed, in conditions as similar as possible to the real operative ones. The main objective has been to identify an accurate analytic model of the device with the associated response time constants, and thus cutting frequencies. Most of all, the knowledge of the first cutting frequency is required, to establish if the selected instrument can properly track the signal in its full spectrum, without distortions or loss of information. Section 4.2.2 describes this characterization.

A 0D analytic model has been developed, to predict the coupled behavior of HT and GG, and thus to derive the frequency spectrum of a typical temperature signal to be read by the diagnostic device. Section 4.2.1 describes the model implemented.

In the next section, the main requirements of the measurement device are listed, and the selected device is reported.

Requirements and Selection of the Temperature Measurement Device

According to the application described, the driving requirements to select the temperature measurement device have been:

- Temperature operative range: [0,800] °C: most of the time the device is at room temperature [10,30] °C but it has to withstand cyclic thermal loads up to 700/800 °C for a maximum duration of 15 seconds and a total of 3 times per week on average.
- Low cost: since the mixture to be measure can be chemically reactive and the temperature could exceed the 800 °C due to unpredictable chemical recombination effects, it is convenient to keep the cost per piece as low as possible. For each component a maximum price of 30 € has been fixed.
- The device has to withstand an oxidizing ambient.

The first and second listed constraints forced to discard immediately the resistance thermometers as a viable solution, also because they have a low response time. A fast response time was not one of the first requirements but a faster instrument was preferred. Among the different types of thermocouples, those made of precious metals have been discarded for cost reasons. The remaining best candidates which satisfy the operative range required were J, K and N types. K types have been discarded for their thermoelectric instability (see appendix 6).
Finally J-type thermocouples have been selected for two main reasons:

- Previous experience in using them, and thus availability of the required acquisition system;

- A higher sensitivity.

Considering the major thermoelectric stability and the wider operative range of N-type's, they represent however a valid alternative.

As a guarantee of protection against the oxidizing ambient, a MIMS J-type insulation has been selected with stainless steel sheath to protect the thermocouple from oxidation. The probe diameter has been selected as a compromise between costs and time response since an extremely fast response was not required; as an example, a ϕ1.5mm-thermocouple costs approximately 30 € while a ϕ0.25mm-thermocouple costs approximately three times. Moreover, probes with smaller diameter are demonstrated to have a shorter lifetime in aggressive ambient.

4.2.1 HT & GG Coupled Functioning Model

The 0D analytic model simulates the combustion process into the hybrid torch, to estimate the HDPE flow rate; this quantity, together with the other mass flow rates involved, is then used to predict the time-varying profile of temperature inside the gas generator, by means of a thermo-chemical software (NASA-CEA).

It has to be highlighted that the model neglects the ignition transient, and so describes the steady functioning of the system, after the step input due to ignition.

Hybrid Torch Modeling

Basically, the hybrid torch behavior is described by the following:

- continuity equation for an isentropic flow of an ideal gas (i.e. the combustion products), applied to the chocked nozzle throat A_{th} of the hybrid torch:

$$\dot{m} = A_{th}\sqrt{\frac{k}{R_g}}\frac{p_0}{\sqrt{T_0}}\left(\frac{2}{k+1}\right)^{\frac{k+1}{2(k-1)}} \tag{4.1}$$

- regression rate law to estimate the burned fuel:

$$\dot{r} = f(G_{ox}, p_c, x, ...) \tag{4.2}$$

- characteristic velocity estimation by means of a thermo-chemical software (CEA):

$$c^* = CEA(A_{th}, m_{ox}, m_f, \eta) \tag{4.3}$$

  where the subscripts ox and f refer respectively to oxidizer and fuel.

These equations are solved step by step; the model has the possibility to add the effect of nozzle throat erosion, combustion efficiency less than 1 and variable oxidizer mass flow rate.

As far as the burned fuel estimation is concerned, in 2002 Carmicino performed a wide test campaign on a lab-scale hybrid motor, burning GOX and HDPE. The geometrical configuration was very similar to the one proper of the hybrid torch.

As a result of this campaign, a not negligible dependency of the instantaneous regression rate from the operative pressure has been found, due to chemical kinetics effects [63]. According to this consideration, Carmicino adopted the Wooldridge and Marxman model [64] to express the instantaneous regression rate law:

$$\dot{r} = aG_{ox}^{n}p_{c}^{m} \tag{4.4}$$

with the following values for the empiric coefficients involved, as the best fit ($R^2 = 0.837$):

- a=0.043;
- n=0.266;
- m=0.476.

The same approach has been adopted in the present model; respect to the values found by Carmicino, the best fit in the present case resulted slightly different:

a	n	m
0.043	0.32	0.365

Table 4.3: GOX-HDPE regression rate law coefficients

The values of these coefficients have been tailored with experimental data provided by a preliminary test campaign on the hybrid torch alone. These preliminary tests confirmed a slight dependency of the resulting mean regression rate from the operative pressure. For further details, the reader is referred to chapter 5.
Three tests were performed in the 50% throttling level configuration, to verify its correct functioning. The main parameters evaluated were:

- oxygen mass flow, deduced from measuring the sonic orifice upstream total pressure and total temperature, according to the isentropic flow relations;
- mean fuel mass flow, simply estimated as the ratio between the fuel mass burned(weighted before and after the test by a balance with $\pm 2\,g$ error) and the burning time;
- pressure inside the hybrid torch combustion chamber;
- nozzle throat diameter before and after test, to check possible erosion effects;
- finally, mean combustion efficiency was calculated as the ratio between the experimental and the theoretical characteristic velocity; the former is calculated from the mean combustion chamber pressure, while the latter can be evaluated thanks to CEA thermochemistry software.

	HT #14	HT #15	HT #16
oxidizer mean mass flow rate, [kg/s]	0.0194	0.0192	0.0192
fuel mean mass flow rate, [kg/s]	0.0089	0.0088	0.0087
mean chamber pressure, [bar]	22.3	22.4	22.3
mean characteristic velocity, [m/s]	1574	1581	1590
efficiency, [%]	87	88	88

Table 4.4: Hybrid torch preliminary test data

Table 4.4 reports the experimental data corresponding to these tests.

These tests have denoted no nozzle erosion; the port diameter represents the only geometric parameter which have changed over the time: no ablative mixing devices were included. So, combustion efficiency has been assumed constant during the whole test, and its value has been calculated referring to the combustion chamber mean pressure. Its value have been used to calculate the actual characteristic velocity, respect to the ideal (perfect equilibrium) value predicted by the thermo-chemical software.

The empiric coefficients in equation 4.4 have been determined by means of a Montecarlo approach with the following requirements:

- step by step, the maximum residual between the fitted value and the moving average of the combustion chamber pressure should be less than 1% respect to the moving average itself;
- the mean fuel mass flow rate predicted by the model should be equal to the experimental one ±2%.

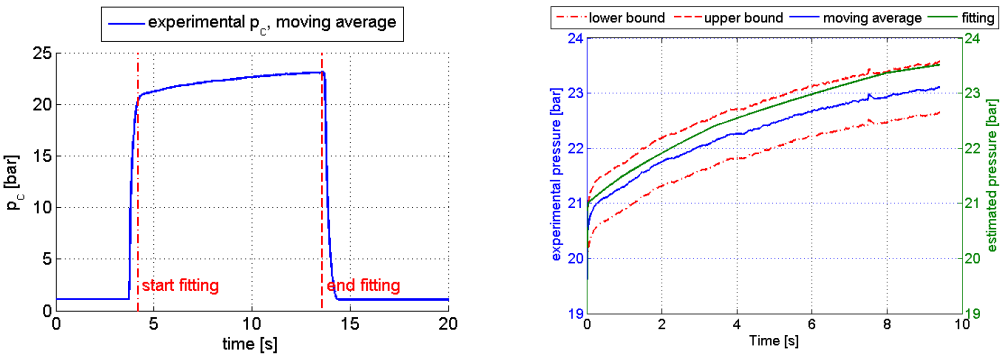

(a) (b)

Figure 4.2: HT combustion chamber pressure: (a) shows the moving average of an experimental acquisition; (b) is the correspondent zoom in, on stationary data, to compare them with the model prediction (required tolerance on residuals is included)

Figure 4.2 reports a comparison between experimental and analytic model. 4.2a shows an example of the HT combustion chamber pressure, as acquired during one of the preliminary tests mentioned (HT14); the vertical lines highlight the stationary range which the analytic model is applied on. 4.2b zooms in, on stationary data, to compare the final fitting with the acquired data; the dotted lines mark the maximum error tolerated on the fitting prediction.
The analytic model in this case has predicted a mean fuel mass flow rate equal to $0.0089\,kg/s$. Figure 4.3 shows the time-varying prediction of the combustion process for this test.

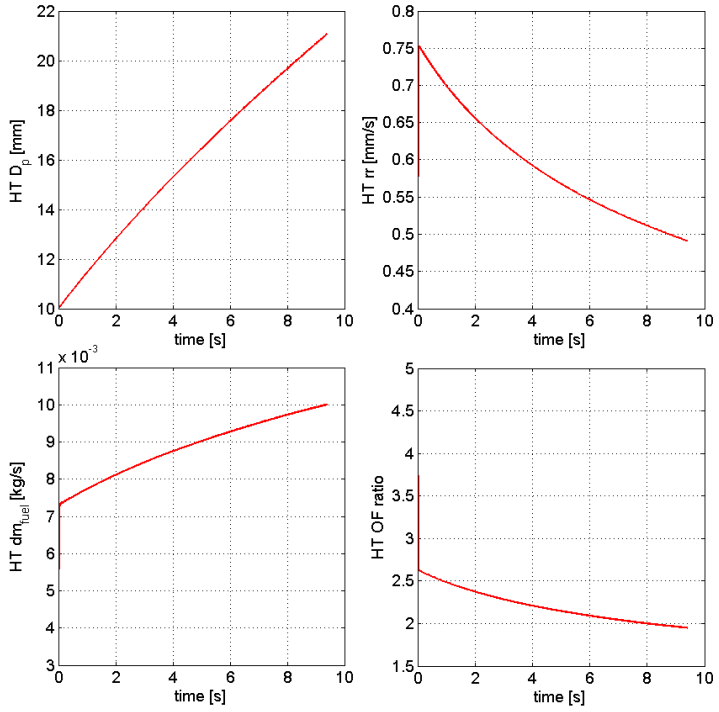

Figure 4.3: HT combustion prediction by the analytic model: port diamater (top left), regression rate (top right), fuel mass flow rate (bottom left), OF ratio (bottom right)

Gas Generator Modeling

The next part of the analytic model regards the estimation of GG functioning. In particular the mixture temperature is estimated step by step, combining thermo-chemistry with the information about the mass flow rates involved. As already said, the main goal is to predict a "typical" temperature profile of the mixture to derive its spectrum, and then to identify a suitable measurement device.

Possible sources of mixture temperature fluctuation could be represented by variations in:

1. HDPE flow rate, due to:

   (a) the hybrid torch combustion process itself (eq. 4.4);
   (b) possible changes of the combustion efficiency, if any ablative mixing device is introduced;
   (c) fluctuation of oxygen mass flow rate provided to the hybrid torch;
2. water and/or oxygen mass flow rate provided to GG;
3. gas generator operative pressure: gas generator and combustion chamber work coupled in terms of pressure; so if the combustion chamber faces any pressure fluctuation, this will affect the gas generator too;
4. mixture temperature variations respect to the theoretical (i.e. predicted by CEA) value, because of:
   (a) thermal dispersion towards the wall;
   (b) chemical reactions: the recombination process in GG depends on the chemical composition of the combustion products coming out from the hybrid torch; if the HT combustion efficiency is low (that is the flame is stratified), the combustion process is not completed when the mixture exit the HT nozzle, and then chemical reactions take place in GG; the efficiency of these chemical processes depends on the turbulent mixing inside GG.

Among the listed aspects, points 1a, 1b, 1c and 3 have been included in the model. 1a is implicitly included in the modeling of the HT combustion process.
HT combustion efficiency can be vary if an ablative mixing device is included: as long as the device is not completely consumed, combustion efficiency is high; then it falls down, to values in the order of what reported in table 4.4, as soon as the device has disappeared.
Fluctuations of oxygen provided to the HT combustion chamber are not expected, but anyhow a slight decrease due to a hypothetically diminishing upstream pressure has been included, to evaluate its effect on the production of pyrolyzed fuel.
Pressure fluctuations inside the main combustion chamber could be potentially due to:

- a change in the operating mode of CC: before HTPB ignition, the motor works as a monopropellant one, then its pressure is subjected to a step change when ignition takes place;
- CC nozzle erosion;
- combustion instabilities.

The step input due to HTPB ignition has been included, while in this context pressure slight decrease due to erosion has been neglected.
As far as combustion instabilities are concerned, it was not expected to face them; according to previous works, found in literature about vortex injection with similar configurations, pressure oscillation were expected to be below 5% [6], [8]. The whole engine test campaign has confirmed this assumption.

Considering the other sources of possible fluctuations listed previously, fluctuations of GG oxygen flow rate and water flow rate can be neglected since they are nominally steady;

during regular functioning of the feed lines, any possible fluctuation arisen would be linearly decreasing, since due to an upstream pressure decrease, caused by tanks emptying.
For what pertains point 4, the thermal dispersion towards the wall obey to a slow dynamic phenomena: as a first approximation, GG can be considered a body with a conductive heat transfer resistance negligible respect to the heat transfer resistance at the surface; this implies a small value of the Biot number ($Bi < 1$). In fact, assuming $h_i \approx 250 \frac{W}{m^2 K}$ as a typical value for air heat transfer coefficient in forced convection inside a tube ([65]), and considering GG wall thickness as the characteristic dimension L, Biot number results:

$$Bi = \frac{h_i L}{\lambda_{ss}} = \frac{250 \cdot 0.008}{14} \approx 0.14 \tag{4.5}$$

where λ_{ss} is the thermal conductivity of AISI316Ti [67]. The value assumed for heat transfer coefficient is precautionary; in fact there can be found in literature smaller values for hot gases in forced convection through a piping, [66].
In such a hypothesis, if a step input is considered for the gas generator, initially at ambient temperature and suddenly subjected to the heat flux provided by the high temperature mixture, its response can be described as exponential with a typical response time calculated as follows:

$$\tau_{GG} = \frac{m_{GG} c_{p,ss}}{A\, h_i} \tag{4.6}$$

where m_{GG}, $c_{p,ss}$ and A represent respectively: gas generator mass, stainless steel specific heat capacity and gas generator inner surface, subjected to the heat transfer.
The effect of natural convection with ambient air has been neglected in this simplified interpretation.

Finally, considering the recombination process inside GG, fluctuations are not expected; any variation depends mainly on the hybrid torch combustion efficiency (and thus on the composition of the mixture coming from the HT nozzle), and the turbulent mixing inside GG; since the combustion efficiency of the hybrid torch is expected not to vary, or at worst to decrease smoothly because of gradual consumption of the mixing device, it is supposed that the consequent GG temperature variation follows this smooth variation. The mixing efficiency inside GG is expected to depend on residence time and turbulence, and thus to be peculiar of the throttling level.

The time-varying profiles of the parameters included in the analytic model have been defined referring to experimental data provided by a test performed on the whole engine, at 50% throttling level ("spartan_23"). The reader is referred to chapter 5, section 5.5.1 for further details.
Figure 4.4 shows the profile used in the analytic model to simulate: HT nozzle throat erosion ((a)), HT combustion efficiency variation ((b)) and GG operative pressure variation, due to sudden HTPB ignition in CC ((c)).

A time-step of *0.001 s* has been used and a test of *12.5 s* duration has been considered. From GG temperature profile, its FFT has been derived; a Hanning window has been adopted. Figure 4.5 reports the resulting estimation of mixture temperature inside GG ((a)), and its FFT, zoomed in the range $[0\,1] Hz$ ((b)).

Analyzing the FFT, no dynamic content is observed above 0.2 Hz. The width of the peak at $\approx 0\,Hz$ depends on the maximum achievable resolution.

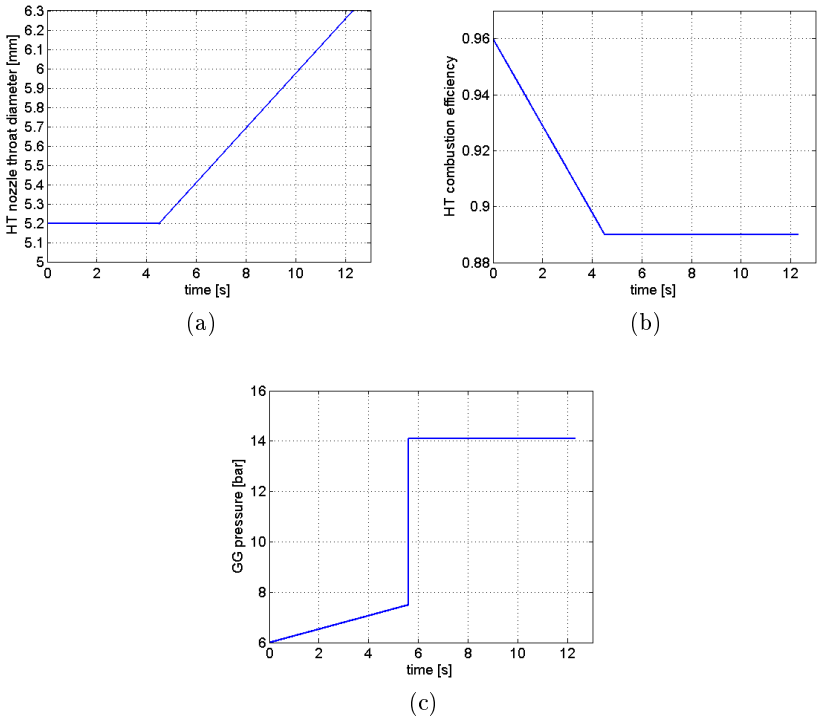

(a) (b) (c)

Figure 4.4: Time-varying profiles of the parameters included in the analytic model: HT nozzle throat erosion ((a)), HT combustion efficiency variation ((b)) and GG operative pressure variation, due to sudden HTPB ignition in CC ((c))

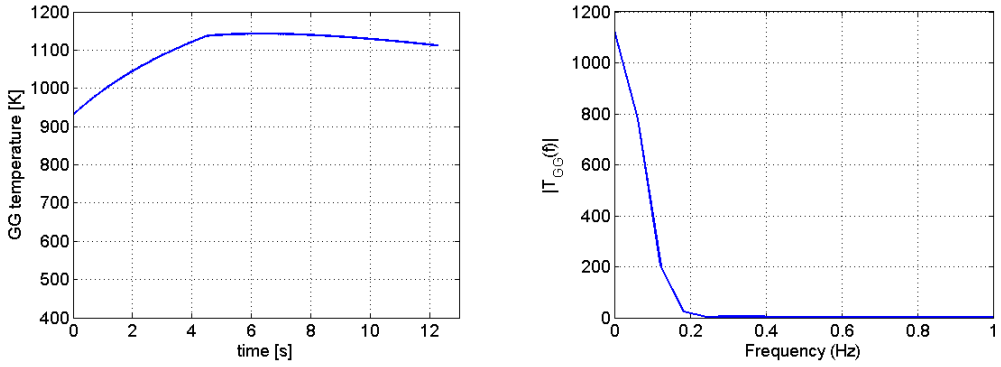

(a) (b)

Figure 4.5: Estimation of mixture temperature inside GG by means of the analytic model: (a) shows the time-varying profile, while (b) represents the temperature spectrum, zoomed in the range $[0\,,\,1]Hz$

Thus, according to what already observed, it is assumed that a typical temperature signal of the GG mixture temperature has no frequency content above 0.2 Hz.

4.2.2 Thermocouple Dynamic Characterization

As far as the static response of a thermocouple is concerned, the uncertainty estimation of a static reading is derived from the norm.

As far as the dynamic response is concerned, a representative test procedure has been defined to experimentally characterize the thermocouple behavior in the specific application.

The basic idea has been to impose a step input to the measurement device, as located in its nominal position, and then to derive its transfer function from the measured response.

The experimental setup was composed by:

- gas generator and hybrid torch assembled together;
- a MIMS J-type thermocouple, installed into the gas generator (see figure 4.1a);
- a Beckhoff PLC for digitalization and acquisition of the signal.

The dynamic characterization of both the thermocouple in GG is reported in the following.

During the dynamic characterization, a preliminary test of HT and GG in their coupled functioning has been used; a 50% throttling level has been considered. The thermocouples have been subjected to the step input produced by the simultaneous adduction in GG of combustion products from the hybrid torch, oxygen and water from the GG feed lines.

The sampling frequency has been set to 20 Hz, since it is not expected to have temperature fluctuation above $f_{Ny} = f_s/2$ (see section 4.2.1) and the cutting frequencies proper of the measurement device are expected to be far below f_s.

To proceed with the analytic modeling of the instrument, a preliminary data analysis has been performed, in order to restrict the data vectors to the interesting range; thus the initial section of the acquisition, where the instrument measures the ambient temperature, has been removed. Moreover, in order to correctly fit the signal, the offset due to the ambient temperature has been removed.

Time Constants Evaluation

According to the test procedure previously described, thermocouples' response, $g_o(t)$, has been acquired.

A MIMS thermocouple can be described as a second order instrument; see appendix 6 reported in appendix for a full description about the thermocouple theoretical modeling.

The steady response of a second order instrument results [68]:

$$g_{os}(t)_{II} = K\left[1 + \frac{1}{\tau_3 - \tau_4}\left(\tau_4 e^{-\frac{t}{\tau_4}} - \tau_3 e^{-\frac{t}{\tau_3}}\right)\right] \tag{4.7}$$

And the transfer function is:

$$W(s)_{II} = \frac{K}{(\tau_3 s + 1)(\tau_4 s + 1)} \tag{4.8}$$

To evaluate the time constants, some mathematical properties of equation 4.7 have been used; in fact it can be rewritten as:

$$\underbrace{ln\left(\frac{K-g_o t}{K}\right)}_{G(t)} = ln\left[\frac{\tau_3}{\tau_3-\tau_4}e^{-\frac{t}{\tau_3}} - \frac{\tau_4}{\tau_3-\tau_4}e^{-\frac{t}{\tau_4}}\right] \tag{4.9}$$

It can be supposed to have a time constant much higher than the other one ($\tau_4 \gg \tau_3$); thus the exponential term with τ_3 can be neglected after a certain time t^*, since its contribution become negligible. So equation 4.9 becomes:

$$ln\left[G\left(t\right)\right] \approx ln\left[\frac{\tau_4}{\tau_4-\tau_3}e^{-\frac{t}{\tau_4}}\right] = ln\left[\frac{\tau_4}{\tau_4-\tau_3} - \frac{t}{\tau_4}\right] = A - \frac{t}{\tau_4} \tag{4.10}$$

which represents the equation for a straight line.
Thus, τ_4 can be derived from the angular coefficient of the function $ln\left[G\left(t\right)\right]$, for $t > t^*$.

Figure 4.6 shows an example of $ln\left[G\left(t\right)\right]$ plot, and the corresponding linear fitting for the evaluation of τ_4.

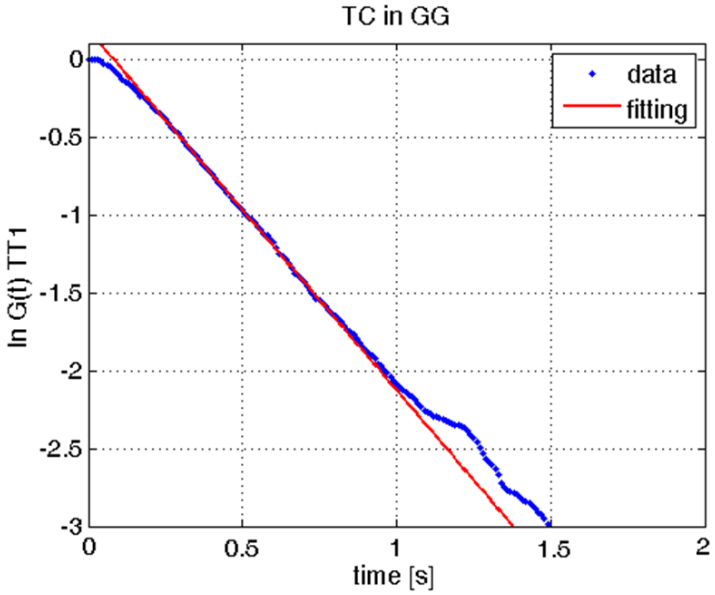

Figure 4.6: Example of linear fitting to evaluate the second time constant

Referring to figure 4.6, the function deviates from linearity both for small values of time, because the effect of the other time constant is not negligible, and for high values of time, because $G\left(t\right) \to 0$, and thus small fluctuations of $G\left(t\right)$ produces large variations of $\ln G\left(t\right)$.

Once calculated τ_4, τ_3 can be estimated with the following:

$$ln\left[G^*\left(t\right)\right] = ln\left[e^{\left(A-\frac{t}{\tau_4}\right)} - G(t)\right] = ln\left[\frac{\tau_3}{\tau_4-\tau_3} - \frac{t}{\tau_3}\right] = B - \frac{t}{\tau_3} \tag{4.11}$$

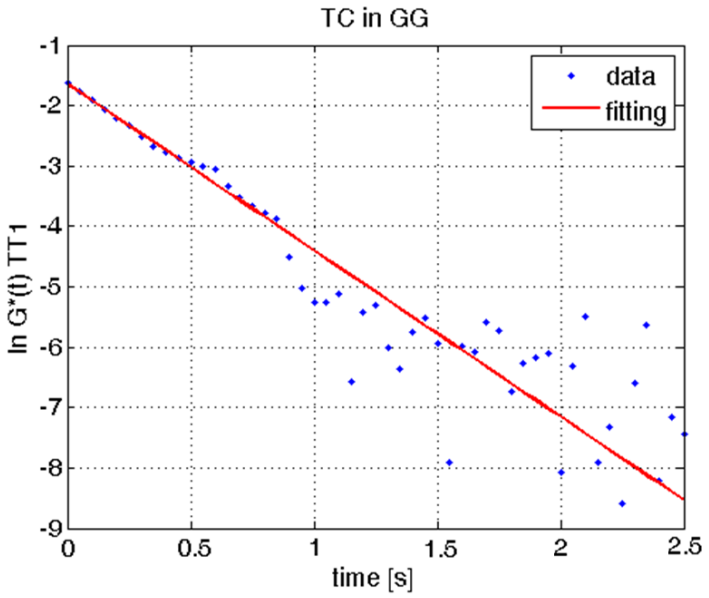

Figure 4.7: Example of linear fitting to evaluate the first time constant

which represents the equation for a straight line.
Thus, τ_3 can be derived from the angular coefficient of the function $ln\left[G^*\left(t\right)\right]$, for $t < t^*$.

It can be seen from figure 4.7 that the function deviates from linearity as the time increases, since $G^*\left(t\right) \to 0$.

Figure 4.8 compares the resulting fitted curve with the acquired experimental data.

Table 4.5 reports the resulting time constants.

Thermocouple	**Parameter**	**Value**	**Uncertainty**
T_{GG}	τ_3	0.06	0.05-0.07
	τ_4	0.44	0.42-0.45

Table 4.5: Thermocouples time constants

The thermocouples is characterized by the following cutting frequencies:

- $fc_1 = 0.36\,\text{Hz}$;
- $fc_1 = 2.65\,\text{Hz}$;

Now that the time constants have been estimated, the dynamic response of this thermocouples for this specific application can be described as a low pass filter with the transfer function of eq. 4.8.

Two main purposes of measuring the GG mixture temperature have been defined at the beginning of the section:

- to assure the structural integrity of the GG case, subjected to thermal loads;

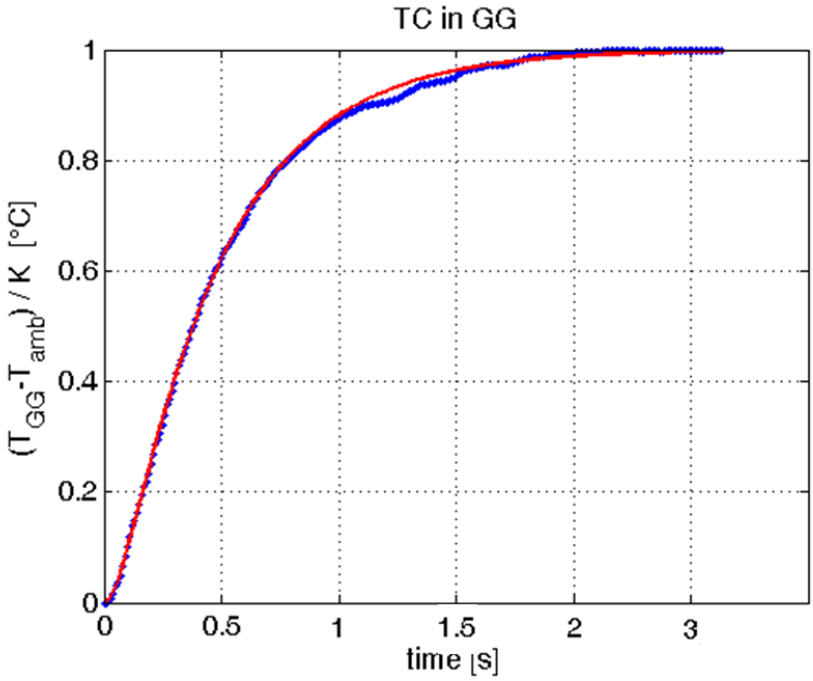

Figure 4.8: GG thermocouple fitting with a 2^{nd} order model

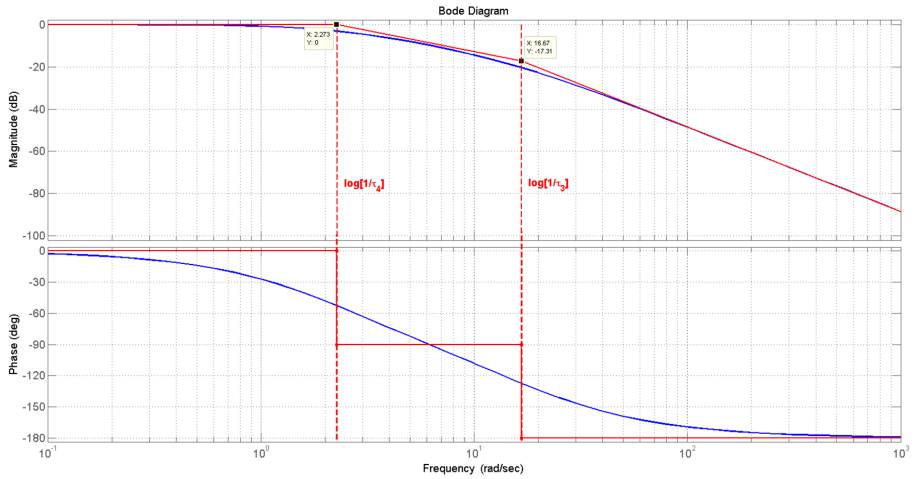

Figure 4.9: Bode diagram for the thermocouple mounted in GG

- to track the mixture temperature, in order to derive useful indication about the mixture composition.

Considering the first aspect, a rough indication of the steel walls response time to a thermal load is provided by eq.4.6; a time constant in the order of $\sim 140s$ is found. Considering the dynamic behavior just characterized for the thermocouple, it can be said that any temperature rise is seen by the thermocouples well in advance before the GG walls would get to that value.

As far as the second aspect is concerned, according to the outcome of section 4.2.1, no frequencies components are expected to be present in the temperature signal above 0.2 Hz, once passed the ignition transient. Thus, the characterized thermocouple is able to follow the typical temperature variations, excluding the transient phase due to ignition: the interesting part of the signal has a frequency component lower than the first natural frequency of the instrument.

Figure 4.10 output signal produced by the thermocoupole, in response to the input signal generated by the analytic model. The thermocouple is not able to follow properly the initial transient phase due to a step input, but it can be seen that it can follow correctly smooth variations of the temperature.

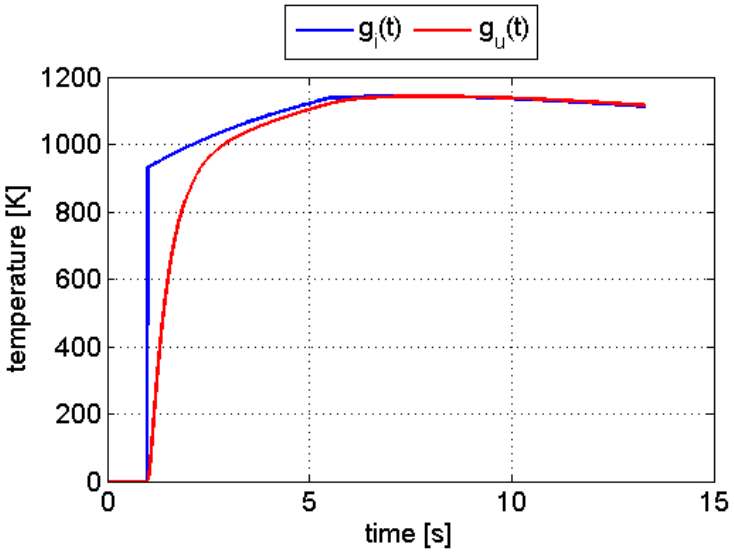

Figure 4.10: GG thermocouple response to a typical temperature profile, as predicted by the analytic method

4.3 Performance Parameters and Uncertainty Analysis

The main parameters that have been directly measured are:

- pressure;
- temperature;
- oxygen mass flow rate for the GG feed line;
- linear position for the water tank's piston;
- HT and CC nozzle throat diameters;
- fuel grains weights and dimensions;

- burning time.

On the other hand, the main quantities indirectly estimated are:

- orifices and venturi discharge coefficients;
- oxygen mass flow rate for the HT feed line;
- water mass flow rate, by means of both the analytic model and the linear potentiometer signal;
- mean fuel flow rate;
- mean and final port diameter of the fuel grain;
- mean fuel regression rate;
- mean characteristic velocity and combustion efficiency.

It has to be highlighted that all the measurements taken into account are to be considered static, or quasi-static: even the time-varying signals acquired by means of the PLC system have been used to calculate the mean value in a range where the measurand does not change.

Thus considering a static measurement, as far as a direct measurement is concerned, the classical methods of estimating type A and type B uncertainties have been adopted (for example: standard deviation of a statistical distribution, manufacturer's specifications, data sheet).

On the other hand, uncertainty for the indirectly estimated quantities has been derived from Kline McClintock error propagation [70]; being $y = y(x_1, \ldots, x_N)$ the parameter to be derived from $(x_1, \ldots, x_N)$ measured data, the error propagation is expressed as follows:

$$i_y = \left[\sum_{i=1}^{N} \left(\frac{\partial y}{\partial x_i} i_{x_i} \right) \right]^{1/2} \tag{4.12}$$

All the uncertainties reported in this work are referred to a cover factor of 3, which means a 99.7% confidence interval, when a Gaussian distribution is considered.

The parameters, acquired by means of the PLC system, are subjected to a rounding error due to a *16 bit* digitizing. This error has been estimated as:

$$i_{AD} = \frac{FS}{2^n - 1} \tag{4.13}$$

where FS is the full scale value, set for the specific channel, and n is the actual bit number, sign's bit excluded (i.e. 15 bits).

This contribution has been combined to the uncertainty due to the instrument accuracy, by means of the quadratic sum of uncertainties, for uncorrelated uncertainties [71]:

$$i_{tot} = 3 \left(\sum_{k=1}^{N} e_i^2 \right)^{1/2} = 3 \left(i_{AD}^2 + \sigma_m^2 \right)^{1/2} \tag{4.14}$$

where σ_m represents the standard deviation of the considered signal, in the time range adopted for its mean value calculation.

In the following, a complete description of the methods adopted to estimate the uncertainties is provided.

4.3.1 Discharge Coefficients

As described in section 3.5, oxygen and water mass flow rates are regulated according to the upstream pressure of the sonic orifices and cavitating venturi, respectively. Equations 3.4 and 3.5 describe the relation between mass flow rate and upstream pressure, given a certain cross section. The discharge coefficient, shown in these equations, is a peculiarity of the specific device considered, unknown at first; so an initial calibration is required to estimate its value.

Rearranging eq. 3.4 and 3.5, the discharge coefficient can be expressed respectively as:

$$C_{d,o} = \frac{\dot{m}_{O2}}{p_0} \frac{\sqrt{T_0}}{A_{so}\sqrt{\frac{k}{R_g}}\left(\frac{2}{k+1}\right)^{\frac{k+1}{2(k-1)}}} \tag{4.15}$$

$$C_{d,cv} = \frac{\dot{m}_{H2O}}{A_{cv}\sqrt{2\rho\left(p_i - p_{sat}\right)}} \tag{4.16}$$

The error propagation (eq. 4.12) to estimate the uncertainties. The uncertainty of k, R_g, and p_{sat} have been considered negligible. The latter parameter is calculated as a function of water temperature, according to an empiric relation: since the resulting uncertainty in the vapor pressure is negligible respect to the other contributions, it has not been considered.

$$i_{C_{d,o}} = \sqrt{\left(\frac{C_{d,o}}{\dot{m}_{O2}} i_{\dot{m}_{O2}}\right)^2 + \left(\frac{1}{2}\frac{C_{d,o}}{T_0} i_{T_0}\right)^2 + \left(-\frac{C_{d,o}}{p_0} i_{p_0}\right)^2 + \left(-\frac{C_{d,o}}{A_{so}} i_{A_{so}}\right)^2} \tag{4.17}$$

$$i_{C_{d,cv}} = \sqrt{\left(\frac{C_{d,cv}}{\dot{m}_{H2O}} i_{\dot{m}_{H2O}}\right)^2 + \left(-\frac{1}{2}\frac{C_{d,cv}}{\rho} i_{\rho}\right)^2 + \left(-\frac{1}{2}\frac{C_{d,cv}}{\Delta p} i_{p_i}\right)^2 + \left(-\frac{C_{d,cv}}{A_{cv}} i_{A_{cv}}\right)^2} \tag{4.18}$$

During the calibration phase, oxygen and water mass flow rates have been measured by means of the Coriolis mass flow meter and the magnetic flow meter, respectively. Referring to eq. 4.17 and 4.18, the different uncertainty contributions have been calculated as follows:

- mass flow rate, upstream pressure and oxygen temperature: 3 times the standard deviation, calculated in the range of steady response of the instrument;
- water density: the variation of its value as a function of temperature in the range [0,25]°C, respect to the reference value, assumed to be at 20°C [72];
- throat section: according to eq. 4.19, the propagation of the uncertainty on throat diameter, which has been assumed equal to the tolerance requested to the manufacturer.

$$i_A = \frac{\pi}{2}\phi\, i_\phi \tag{4.19}$$

Typical values of the uncertainties considered are listed in table 4.6.

Parameter	Value	Uncertainty	Relative uncertainty
$\dot{m}_{O2}$, [kg/s]	0.1036	± 0.006	$\pm 0.6\%$
T_0, [K]	279	± 0.5	$\pm 0.2\%$
p_0, [bar]	62.0	± 0.2	$\pm 0.3\%$
ϕ_o, [mm]	3	± 0.05	$\pm 1.7\%$
A_o, [m^2]	$7.1 \cdot 10^{-6}$	$\pm 2.4 \cdot 10^{-7}$	$\pm 3.3\%$
$\dot{m}_{H2O}$, [kg/s]	0.0577	± 0.0005	$\pm 0.9\%$
ρ, [kg/m^3]	998	± 1	$\pm 0.1\%$
p_i, [bar]	24.9	± 1.1	$\pm 4.4\%$
ϕ_{cv}, [mm]	1.1	± 0.01	$\pm 0.9\%$
A_{cv}, [m^2]	$9.5 \cdot 10^{-7}$	$\pm 1.7 \cdot 10^{-8}$	$\pm 1.8\%$

Table 4.6: Discharge coefficients evaluation: typical uncertanties

4.3.2 Mass Flow Rates and Regression Rate

Water Mass Flow Rate

The time-varying volume occupied by water inside the tank is monitored by means of the linear potentiometer. Its signal has been used as the primary reference for the water mass flow rate calculation, since it provides a more accurate measurement respect to the analytic formula with C_d.

Mass flow rate is derived from the equation:

$$\dot{m}_{H2O} = \rho_{H2O} A_{tk} v_p \tag{4.20}$$

where A_{tk} represents the tank inner cross section, and v_p is the velocity of the piston. The latter can be derived from the linear displacement of the piston, ΔL, which is measured by the linear potentiometer:

$$v_p = \frac{\Delta L}{\Delta t} \tag{4.21}$$

This method can be applied both to a dynamic estimation of the mass flow rate (and $\Delta L \to \delta L$ and $\Delta t \to \delta t$) and to a mean value calculation. The linear potentiometer can be considered a zero order instrument; thus no dynamic effects of attenuation or phase change has to be considered for the expected velocities of the piston.

The error propagation equation, eq. 4.12, applied to eq. 4.20 results:

$$i_{\dot{m}} = \sqrt{\left(\frac{\dot{m}}{v_p} i_{v_p}\right)^2 + \left(\frac{\dot{m}}{A_{tk}} i_{A_{tk}}\right)^2 + \left(\frac{\dot{m}}{\rho} i_{\rho}\right)^2} \tag{4.22}$$

The uncertainty $i_{A_{tk}}$ is calculated with eq. 4.19.

The uncertainty i_{v_p} is calculated again with eq. 4.12:

$$i_{v_p} = \sqrt{\left(\frac{1}{\Delta t} i_{\Delta L}\right)^2 + \left(\frac{\Delta L}{\Delta t^2} i_{\Delta t}\right)^2} \tag{4.23}$$

where the uncertainty of the piston travel, $i_{\Delta L}$, is calculated propagating the error of displacement, due to linearity errors, reported in the data sheet of the instrument.

Typical values of the resulting uncertainties are reported in table 4.7. These data refers to the mean mass flow rate calculation, which considers the initial and final displacement of the piston, to evaluate the piston travel; this approach implicitly assumes a linear trend of the displacement as a function of time, and thus a constant mass flow rate, which is the actual condition of each test.

Parameter	**Value**	**Uncertainty**	**Relative uncertainty**
Δt, [s]	7.14	± 0.01	$\pm 0.1\%$
ΔL, [mm]	40.1	± 0.2	$\pm 0.5\%$
v_p,[mm/s]	5.6	± 0.01	$\pm 0.2\%$
$\dot{m}_{H2O}$, [kg/s]	0.1127	± 0.0005	$\pm 0.4\%$

Table 4.7: Water mass flow rate derivation from linear potentiometer signal: typical uncertanties

HT Oxygen Mass Flow Rate

The oxygen mass flow rate for the hybrid torch feed line is calculated according to eq. 3.4. Thus the uncertainty results:

$$i_{\dot{m}_{O2}} = \sqrt{\left(\frac{\dot{m}_{O2}}{C_{d,o}} i_{C_{d,o}}\right)^2 + \left(\frac{\dot{m}_{O2}}{A_{so}} i_{A_{so}}\right)^2 + \left(\frac{\dot{m}_{O2}}{p_0} i_{p_0}\right)^2 + \left(-\frac{1}{2}\frac{\dot{m}_{O2}}{T_0} i_{T_0}\right)^2} \tag{4.24}$$

Most of the uncertainties involved in this formulation have already been reported in table 4.6.

Typical values of oxygen mass flow rate and its uncertainty are reported in table 4.8.

Parameter	**Value**	**Uncertainty**	**Relative uncertainty**
$\dot{m}_{O2}$, [kg/s]	0.044	± 0.002	$\pm 5.5\%$

Table 4.8: Oxygen mass flow rate for HT feed line: typical uncertantiy

Fuel Mass Flow Rate

A mean mass flow rate is evaluated, both for the hybrid torch (HDPE fuel) and the main combustion chamber (HTPB fuel).

The mean value is calculated from the weight loss of the fuel grain, ΔM_f, and the burning time, t_b, according to eq. 4.25:

$$\bar{\dot{m}}_f = \frac{\Delta M_f}{t_b} = \frac{M_{f,s} - M_{f,e}}{t_b} \tag{4.25}$$

The thrust termination effect has been neglected in the burning time evaluation. At the end of each test, not all the valves are closed together; in fact the valve of the water feed line is closed 0.5 s after the others, to perform a purging of the main combustion chamber. Thus it is assumed that the combustion in the main combustion chamber is immediately interrupted, once closed the oxygen valves: the termination tail does not participate to the burning time of HTPB. The pressure tail is very fast, and it is attributed to a "cold" emptying of the chamber. As far as the burning time of the hybrid torch is concerned, the tail is included in the burning time of HDPE as a source of uncertainty (see table 4.9).

According to Kline McClintock propagation, eq. 4.12, the uncertainty of the fuel mass flow rate is calculated as follows:

$$i_{\bar{\dot{m}}_f} = \sqrt{\left(\frac{\bar{\dot{m}}_f}{\Delta M_f} i_{\Delta M_f}\right)^2 + \left(\frac{\bar{\dot{m}}_f}{t_b} i_{t_b}\right)^2} \tag{4.26}$$

where $i_{\Delta M_f}$ is calculated combining the uncertainty of fuel grain weighting.

Typical values of the uncertainties involved are reported in table 4.9.

Parameter	**Value**	**Uncertainty**	**Relative uncertainty**
	HDPE, Hybrid Torch		
ΔM_f, [g]	152	± 2.8	$\pm 1.9\%$
t_b, [s]	10	± 0.4	$\pm 4\%$
$\bar{\dot{m}}_f$, [kg/s]	0.0152	± 0.0007	$\pm 4.4\%$
	HTPB, Combustion Chamber		
ΔM_f, [g]	376	± 2.8	$\pm 0.8\%$
t_b, [s]	7.1	± 0.3	$\pm 4.2\%$
$\bar{\dot{m}}_f$, [kg/s]	0.0526	± 0.0005	$\pm 1.0\%$

Table 4.9: Mean fuel mass flow rate: typical uncertantities

Regression Rate

Several techniques have been developed in years to locally measure the time-varying trend of regression rate: ultrasound, plasma capacitance gauge and resistance-based methods represent the best compromise between costs and accuracy and versatility [74].

In this work just a space-time averaged value is calculated, thus in the hypothesis of uniform regression along the grain length and during all the burning time, t_b.

$$\bar{\dot{r}} = \frac{D_{p,f} - D_{p,i}}{2\,t_b} \tag{4.27}$$

where $D_{p,i}$ and $D_{p,f}$ represents the initial and final grain port diameter, respectively. The latter is calculated according to the following:

$$D_{p,f} = \sqrt{D_{p,i}^2 + \frac{4\Delta M_{fuel}}{\pi \rho_{fuel} L_{grain}}} \tag{4.28}$$

Regression rate mean calculation is performed as already discussed both for the hybrid torch and the combustion chamber, but it must be said that:

1. HT mean regression rate is taken into account exclusively as a qualitatively comparison parameter, when considering different hybrid torch configurations or operative conditions;

2. CC mean regression rate was expected to be quite uniform along the grain length, according to what discussed about impingement effects in fully tangential vortex (see section 2.2.2).

Both the HDPE and HTPB grain port diameter has been measured after each test: the former has been measured in three position, front, middle, and back, while the latter at the front and at the back. The maximum diameter difference detected along the grain has been: <10% for HDPE and <8% for HTPB, thus the hypothesis of cylindrical shape after the burn has been considered suitable.

Referring to eq. 4.27 and eq. 4.28, the correspondent uncertainties have been calculated as follows:

$$i_{\dot{r}} = \sqrt{\left(\frac{1}{2\,t_b^2} i_{D_{p,f}}\right)^2 + \left(-\frac{1}{2\,t_b} i_{D_{p,i}}\right)^2 + \left(\frac{\dot{r}}{2\,t_b} i_{t_b}\right)^2} \tag{4.29}$$

$$i_{D_{p,f}} = \sqrt{\left(\frac{D_{p,i}}{D_{p,f}} i_{D_{p,i}}\right)^2 + \left(\frac{2}{\pi \rho_f L_g D_{p,f}} i_{\Delta M_f}\right)^2 + \left(\frac{2\,\Delta M_f}{\pi \rho_f^2 L_g D_{p,f}} i_{\rho_f}\right)^2 + \left(\frac{2\,\Delta M_f}{\pi \rho_f L_g^2 D_{p,f}} i_{L_g}\right)^2} \tag{4.30}$$

Table 4.10 summarize typical values of the uncertainties obtained in these calculations.

Oxidizer Specific Mass Flow Rate

The oxidizer specific flow rate has been calculated for the main combustion chamber, in order to express its relation with the resulting regression rate. A mean value has been calculated, according to the equation:

$$\bar{G}_{ox} = \frac{16 \bar{\dot{m}}_{ox}}{\pi \left(D_{p,f} + D_{p,i}\right)^2} \tag{4.31}$$

Parameter	Value	Uncertainty	Relative uncertainty
	HDPE, Hybrid Torch		
$D_{p,i}$, [mm]	10	±0.1	±1%
L_g, [mm]	292.6	±1	±0.3%
ρ_f, [kg/m^3]	930	±20	±2.1%
$D_{p,f}$, [mm]	28.4	±0.4	±1.3%
$\dot{r}$, [mm/s]	0.93	±0.04	±4.5%
	HTPB, Combustion Chamber		
$D_{p,i}$, [mm]	33.7	±1	±3%
L_g, [mm]	230	±1	±0.4%
ρ_f, [kg/m^3]	953	±5	±0.5%
$D_{p,f}$, [mm]	57.6	±0.6	±1.1%
$\dot{r}$, [mm/s]	1.67	±0.11	±6.4%

Table 4.10: Fuel regression rate: typical uncertantities

where the mean oxidizer flow rate is the sum of all the contribution coming from the gas generator, so: $\bar{\dot{m}}_{ox} = \bar{\dot{m}}_{O2}^{GG} + \bar{\dot{m}}_{O2}^{HT} + \bar{\dot{m}}_{H2O} + \bar{\dot{m}}_{HDPE}$. Its uncertainty has been deduced propagating the uncertainty due to each contribution.

The specific oxidizer flow rate uncertainty results:

$$i_{G_{ox}} = \sqrt{\left(\frac{2\,G_{ox}}{D_{p,f} + D_{p,i}}\right)^2 \left(i_{D_{p,i}}^2 + i_{D_{p,f}}^2)\right) + \left(\frac{G_{ox}}{\bar{\dot{m}}_{ox}} i_{\bar{\dot{m}}_{ox}}\right)^2} \tag{4.32}$$

Typical values are those reported in table 4.11.

Parameter	Value	Uncertainty	Relative uncertainty
$\dot{m}_{ox}$, [kg/s]	0.312	±0.004	±1.1%
$\dot{G}_{ox}$, [kg/m^{2}s]	190	±10	±5.3%

Table 4.11: Oxydizer specific mass flow rate for CC: typical uncertantiy

4.3.3 Combustion Efficiency

Combustion efficiency, η, is calculated as the ratio between the actual characteristic exhaust velocity, c_r^*, and the theoretical one, c_t^*, correspondent to the condition of chemically perfect equilibrium.

$$\eta = \frac{c^*}{c^*_{th}} = \frac{p_c\, A_{th}}{\dot{m}_{tot}} \cdot \frac{1}{c^*_{CEA}} \tag{4.33}$$

The latter can be calculated by means of any thermochemical software, providing as inputs:

- oxidizer and fuel mass flow rates,
- nozzle expansion ratio,
- nozzle throat diameter.

In this work, the theoretical characteristic velocity has been calculated for the 87.5%H2O2-HTPB propellants combination.

Its uncertainty has been estimated by a Montecarlo method, to evaluate the influence of the uncertainty of these inputs.

For each input, generically indicated as v_i, a range of possible values has been defined as:

$$\Delta = [v_i - \sigma, v_i + \sigma] = \left[v_i - \frac{i_{v_i}}{3}, v_i + \frac{i_{v_i}}{3}\right] \tag{4.34}$$

where i_{v_i} is the 3σ standard deviation of v_i.

A random combination of the aforementioned inputs in their respective ranges is generated, according to a Gaussian distribution; these inputs are provided to CEA to estimate the resulting theoretical c^*. 1000 combinations have been generated, to build the histogram. Figure 4.11 reports an example of a typical output.

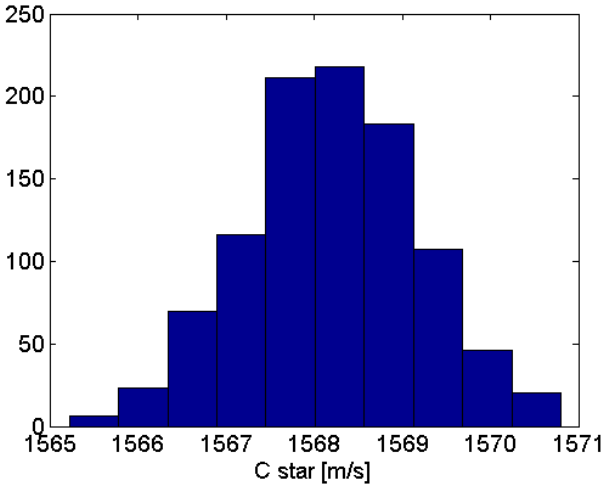

Figure 4.11: Histogram of theoretical c^*: effect of inputs uncertainties

The distribution has been considered a Gaussian distribution; so the 3σ standard deviation has been adopted as uncertainty of c^*_t.

On the other hand, the actual value, c_r^*, can be calculated according to the following [64]:

$$c_r^* = \frac{p_c\, A_{th}}{\dot{m}_{tot}} \tag{4.35}$$

where A_{th} is the CC nozzle throat section and $\dot{m}_{tot}$ is the sum of GG mixture mass flow rate and burnt HTPB mass flow rate.

So the uncertainty proper of the actual characteristic velocity and combustion efficiency are calculated respectively as:

$$i_{c_r^*} = \sqrt{\left(\frac{c_r^*}{p_c} i_{p_c}\right)^2 + \left(\frac{c_r^*}{A_{th}} i_{A_{th}}\right)^2 + \left(\frac{c_r^*}{\dot{m}_{tot}} i_{\dot{m}_{tot}}\right)^2} \tag{4.36}$$

$$i_\eta = \sqrt{\left(\frac{\eta}{c_r^*} i_{c_r^*}\right)^2 + \left(\frac{\eta}{c_t^*} i_{c_t^*}\right)^2} \tag{4.37}$$

$$\tag{4.38}$$

Combustion efficiency has been calculated as a mean value for each test, considering the mean combustion chamber pressure, p_c, and total mass flow rate, $\dot{m}_{tot}$.

Typical uncertainties are listed in table 4.12.

Parameter	**Value**	**Uncertainty**	**Relative uncertainty**
p_c, [bar]	28.7	± 1.1	$\pm 3.7\%$
$\dot{m}_{tot}$, [kg/s]	0.365	± 0.004	$\pm 1.2\%$
A_{th}, [m^2]	$1.99 \cdot 10^{-4}$	$\pm 1 \cdot 10^{-6}$	$\pm 0.6\%$
c_t^*, [m/s]	1590	± 3	$\pm 0.2\%$
c_r^*, [m/s]	1562	± 61	$\pm 3.9\%$
η	0.98	± 0.04	$\pm 3.9\%$

Table 4.12: Combustion efficiency of CC: typical uncertainty

4.3.4 GG Mixture Temperature

According to what discussed in section 4.2, the thermocouple responsible of measuring the temperature of the GG mixture is assumed to work in a quasi-static mode. In this hypothesis, the uncertainty typical of a static reading is considered, thus neglecting any attenuation or phase change effect caused by the dynamic characteristics. In fact, it has to be underlined that the temperature measurement of the mixture has been considered only in the time range of CC burning, where only smooth variations are expected.

The norm EN 60584-1 (IEC 584-1) provides the relation: $\pm 0.0075|t|$ to estimate the reading uncertainty (see table 6.2 in annex).

The final error is derived combining the just mentioned error with the rounding error due to the acquisition system; the latter is estimated according to eq. 4.13 and the final error is obtained from eq. 4.14.

Typical values are reported in table 4.13.

Parameter	Value	Uncertainty	Relative uncertainty
T_{GG}, [°C]	597	±5	±0.8%

Table 4.13: GG mixture temperature measurement: typical uncertanties

4.3.5 GG Mixture Composition

An estimation of the oxidizer mixture composition coming from the gas generator is required for two main reason:

1. to evaluate the difference of oxidizer composition between each test, in order to assure repeatability;
2. to verify if the oxygen mass fraction is close to the desired value (i.e. 0.41), which is typical of decomposed hydrogen peroxide in 87.5% concentration.

The ideal composition of the GG mixture is estimated by means of CEA thermochemical software; the inputs provided are:

- total oxygen mass flow rate (HT plus GG),
- water and HDPE mass flow rates,
- operative GG pressure.

CEA calculates the composition obtained at perfect chemical equilibrium.
Three main sources of errors can be identified:

1. uncertainties of the inputs;
2. thermal dissipation toward the gas generator walls make the process not-adiabatic;
3. efficiency of the turbulent mixing in GG limits the completeness of the chemical processes respect to the ideal case.

The estimation of the effect of these phenomena on the actual mixture composition is not straightforward.

As far as the last two aspects are concerned, two extreme cases have been considered, as a rough estimation:

1. the mixture in GG reaches the condition of perfect equilibrium but the process is not-adiabatic outward: so the chemical processes are forced to take place at assigned temperature and pressure;
2. the process is adiabatic outward but the perfect equilibrium condition is not reached.

In the following, the approach adopted to estimate these errors is described.

Uncertainties of the inputs

A Montecarlo method has been adopted.

For each of the aforementioned inputs, generically indicated as v_i, a range of possible values has been defined as:

$$\Delta = [v_i - \sigma, v_i + \sigma] = \left[v_i - \frac{i_{v_i}}{3}, v_i + \frac{i_{v_i}}{3}\right] \tag{4.39}$$

where i_{v_i} is the 3σ standard deviation of v_i.

A random combination of inputs in their respective ranges is generated, according to a Gaussian distribution; these inputs are provided to CEA to estimate the resulting composition.

For each experimental test, 10000 combinations have been generated, to build the histogram of distribution of the resulting mass fractions, composing the mixture. Figure 4.12 reports an example of a typical output.

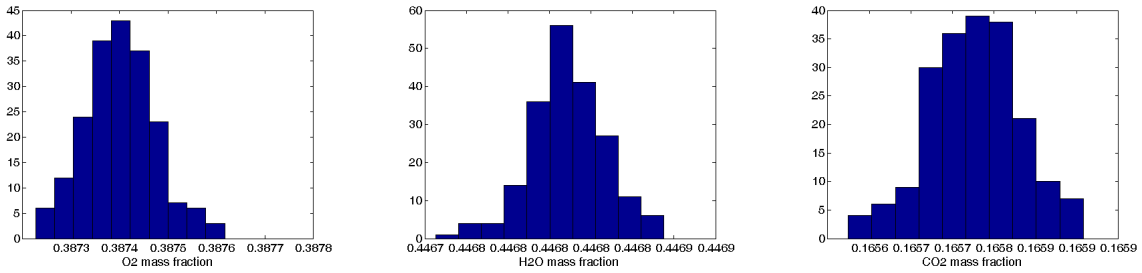

(a) (b) (c)

Figure 4.12: Histograms of GG mixture composition: effect of mass flow rates and pressure uncertainties on O2 mass fraction (a), H2O mass fraction (b), and CO2 mass fraction (c)

The probability distribution has been fitted with a Gaussian function and the corresponding 3σ standard deviation has been considered the final uncertainty of each mass fraction.

In the worst case (CO mass fraction), the maximum variation of the resulting mass fraction is up to $\pm 0.1\%$, respect to the central value.

Considering this result, the uncertainty about the inputs has been neglected, as a possible source of error in the estimation of the GG mixture composition.

Perfect Equilibrium, Not-Adiabatic Outward

The composition in this case is estimated by CEA, assigning as pressure and temperature the operative values measured experimentally.

The operative pressure during HTPB combustion has been used; as far as the mixture temperature is concerned, the value measured immediately upstream the vortex injector has been used, in correspondence of a plateau immediately before HTPB ignition. Since the temperature measured inside GG is not constant, during CC combustion, but it results slightly increasing during time, a sensitivity analysis has been performed, to evaluate the

influence of this variation on the resulting not-adiabatic composition. It has been found that the typical temperature span has a totally negligible effect on the resulting mass fractions.

The not-adiabatic mixture composition is almost identical to the adiabatic one; a maximum difference equal to 0.2% has been found between the adiabatic mixture mass fractions and the not-adiabatic one.

Table 4.14 reports the typical results obtained for each throttling level.

Test	**Input**	**Composition, mass fractions**	
		Not-adiabatic	**Adiabatic**
spartan_ 23, 50%	$T_0 = 575°C$ $p_0 = 14\,bar$ $m_{O2,HT} = 22\,g$ $m_{O2,GG} = 69.4\,g$ $m_{H2O,GG} = 62\,g$ $m_{HDPE} = 7.9\,g$	$mf_{CO2} = 0.154$ $mf_{H2O} = 0.447$ $mf_{O2} = 0.399$	$mf_{CO2} = 0.154$ $mf_{H2O} = 0.447$ $mf_{O2} = 0.399$
spartan_ 38, 75%	$T_0 = 525°C$ $p_0 = 24\,bar$ $m_{O2,HT} = 34\,g$ $m_{O2,GG} = 100.7\,g$ $m_{H2O,GG} = 89.9\,g$ $m_{HDPE} = 12.5\,g$	$mf_{CO2} = 0.165$ $mf_{H2O} = 0.447$ $mf_{O2} = 0.388$	$mf_{CO2} = 0.165$ $mf_{H2O} = 0.447$ $mf_{O2} = 0.388$
spartan_ 34, 75%	$T_0 = 598°C$ $p_0 = 24\,bar$ $m_{O2,HT} = 44\,g$ $m_{O2,GG} = 140\,g$ $m_{H2O,GG} = 112.7\,g$ $m_{HDPE} = 15.2\,g$	$mf_{CO2} = 0.153$ $mf_{H2O} = 0.424$ $mf_{O2} = 0.423$	$mf_{CO2} = 0.153$ $mf_{H2O} = 0.424$ $mf_{O2} = 0.423$

Table 4.14: Not-adiabatic mixture composition

Not-Perfect Equilibrium, Adiabatic Outward.

The efficiency of the process is evaluated comparing the theoretical total enthalpy of the mixture with the actual one.

As a first approximation it is assumed that:

- the variation of the specific heat capacity of the mixture, $c_{p,m}$, as a function of temperature is negligible, thus a mean value in the operative range is considered;
- the specific heat capacity, $c_{p,m}$, is almost the same for the completely mixed mixture and the incomplete one;
- as a direct consequence, the loss of energy (i.e. enthalpy) due to an incomplete mixing causes the mixture to have a certain amount of unburnt reactants;
- the total percentage of unburnt mass is equal to the percentage of enthalpy lost between the theoretical and the real case;
- the unburnt mass of each reactant in the final mixture is calculated according the reciprocal mass ratio at inlet.

In support of the second hypothesis, the specific heat capacity of the ideal mixture, as provided by CEA, has been compared with the specific heat capacity calculated for the correspondent non reacted GG mixture of oxygen, steam and ethylene at the actual temperature measured inside GG, according to the equation [73]:

$$c_{p,m} = \sum_{i=1}^{N} \left[\left(\frac{m_i}{m_{tot}} c_{p,i} \right) \right] \tag{4.40}$$

where $\frac{m_i}{m_{tot}}$ represents the mass fraction of each component, i; the specific capacity of each component, $c_{p,i}$ has been derived from [45].

The resulting difference in terms of $c_{p,m}$ is less than 5%.

According to the aforementioned assumptions, the total percentage, P_{ub}, of unburnt mass, m_{ub}, respect to the total oxidizer mass, m_{ox}^{GG}, has been calculated as follows:

$$P_{ub} = \frac{m_{ub}}{m_{ox}^{GG}} = \frac{T_{id} - Tr}{T_{id} - Tin} \tag{4.41}$$

where T_{id} represents the ideal temperature achieved by the mixture, as predicted by CEA at perfect equilibrium, considering the actual operative pressure, and mass flow rates; on the other hand, T_r is the mixture temperature actually measured upstream the vortex injector; finally T_{in} is the initial temperature of the reactants, considering the control volume equal to HT plus GG.

Thus the difference of energy between the ideal and the real case is reduced to a difference of temperature.

The real temperature, T_r, has been assumed equal to the value measured by the thermocouple mounted in GG, upstream the vortex injector, once passed the ignition transient, and immediately before HTPB ignition, in correspondence of a plateau.

Once estimated P_{ub}, the final mixture is composed as follows:

- $m_{ox}^{GG} \cdot (1 - P_{ub})$ has the mass fraction composition provided by CEA in the ideal case;
- $m_{ox}^{GG} \cdot P_{ub}$ has the mass fraction composition of the unburnt GG mixture, considering the contribution of: O2 HT, HDPE HT, O2 GG, H2O GG.

Table 4.15 reports the typical results obtained for each throttling level, while table 4.16 compares the ideal composition with the not-ideal one.

Test	**Input**	T_{id} [K]	T_r [K]	P_{ub} [%]	**Composition**		
							Final result
spartan_36 50%	$T_{in} = 298\,K$	1158	873	33		$mf_{CO2} = 0.161$	
	$p_0 = 16\,bar$				$(1 - P_{ub})\%$	$mf_{H2O} = 0.444$	$mf_{CO2} = 0.108$
	$m_{O2,HT} = 21.9\,g$					$mf_{O2} = 0.395$	$mf_{H2O} = 0.422$
	$m_{O2,GG} = 69.1\,g$					$mf_{C2H4} = 0.051$	$mf_{O2} = 0.453$
	$m_{H2O,GG} = 60.1\,g$				$P_{ub}\%$	$mf_{H2O} = 0.377$	$mf_{C2H4} = 0.017$
	$m_{HDPE} = 8.2\,g$					$mf_{O2} = 0.571$	
spartan_26 75%	$T_{in} = 298\,K$	1194	953	27		$mf_{CO2} = 0.166$	
	$p_0 = 18\,bar$				$(1 - P_{ub})\%$	$mf_{H2O} = 0.445$	$mf_{CO2} = 0.121$
	$m_{O2,HT} = 34.5\,g$					$mf_{O2} = 0.389$	$mf_{H2O} = 0.427$
	$m_{O2,GG} = 104\,g$					$mf_{C2H4} = 0.053$	$mf_{O2} = 0.437$
	$m_{H2O,GG} = 91.9\,g$				$P_{ub}\%$	$mf_{H2O} = 0.378$	$mf_{C2H4} = 0.014$
	$m_{HDPE} = 12.9\,g$					$mf_{O2} = 0.569$	
spartan_31 100%	$T_{in} = 298\,K$	1121	923	24		$mf_{CO2} = 0.150$	
	$p_0 = 27\,bar$				$(1 - P_{ub})\%$	$mf_{H2O} = 0.431$	$mf_{CO2} = 0.114$
	$m_{O2,HT} = 43.5\,g$					$mf_{O2} = 0.419$	$mf_{H2O} = 0.416$
	$m_{O2,GG} = 138.2\,g$					$mf_{C2H4} = 0.048$	$mf_{O2} = 0.458$
	$m_{H2O,GG} = 113.3\,g$				$P_{ub}\%$	$mf_{H2O} = 0.369$	$mf_{C2H4} = 0.011$
	$m_{HDPE} = 15.0\,g$					$mf_{O2} = 0.583$	

Table 4.15: Not-perfect equilibrium mixture composition

Test	Perfect equilibrium	Not-perfect equilibrium	Relative error
spartan_36 50%	$mf_{O2} = 0.395$	$mf_{O2} = 0.453$	14.8%
	$mf_{H2O} = 0.444$	$mf_{H2O} = 0.422$	-5.0%
	$mf_{CO2} = 0.161$	$mf_{CO2} = 0.108$	-33.1%
		$mf_{C2H4} = 0.017$	-
spartan_26 75%	$mf_{O2} = 0.389$	$mf_{O2} = 0.437$	12.5%
	$mf_{H2O} = 0.445$	$mf_{H2O} = 0.427$	-4.1%
	$mf_{CO2} = 0.166$	$mf_{CO2} = 0.121$	-26.9%
		$mf_{C2H4} = 0.014$	-
spartan_31 100%	$mf_{O2} = 0.419$	$mf_{O2} = 0.458$	9.4%
	$mf_{H2O} = 0.431$	$mf_{H2O} = 0.416$	-3.4%
	$mf_{CO2} = 0.150$	$mf_{CO2} = 0.114$	-24.1%
		$mf_{C2H4} = 0.011$	-

Table 4.16: Perfect versus not-perfect equilibrium mixture composition comparison

4.4 Feed Lines Calibrations

As described in section 3.5, the hydraulic circuit is constituted by three different feed lines:

- line 1: oxygen for the hybrid torch;
- line 2: oxygen for the gas generator;
- line 3: water for the gas generator

The mass flow rate provided by each line is regulated thanks to a choked orifice: sonic orifices for the oxygen feed lines, and a cavitating venturi for the water feed line.
The following sections describe the calibration tests, performed basically to characterize the discharge coefficient of these orifices, and thus calibrate the law describing the mass flow rate.

For each feed line calibration, the adopted procedure has been the same: the pressurized tanks, where the fluid is stored, have been connected to the integrated feed line, upstream to the injection plate; mass flow rate, total temperature and upstream pressure have been measured.

4.4.1 Oxygen Feed Lines

Both O2 lines are provided with sonic orifices to set the mass flow rates at the design values: the aim is to keep the absolute value of mass flow independent from the downstream pressure.

As already shown in chapter 3, the governing equation is the 4.1, applied to the choked section of the sonic orifice, A_{so}:

$$\dot{m}_{o2} = C_d A_{so} \sqrt{\frac{k}{R_{g,O2}}} \frac{p_{0,O2}}{\sqrt{T_{0,O2}}} \left(\frac{2}{k+1}\right)^{\frac{k+1}{2(k-1)}} \tag{4.42}$$

Referring to the previous equation, it can be deduced that the mass flow, in choked condition through the sonic orifice, depends on:

- fluid properties (R_g, k);
- sonic orifice upstream pressure, $p_{0,O2}$;
- total temperature, $T_{0,O2}$;
- orifice throat section, A_{so};
- discharge coefficient, C_d.

So, the desired mass flow can be obtained by setting the upstream pressure. This type of mass control device needs a dedicated calibration procedure before use, to evaluate the discharge coefficient: it has been assumed equal to 1 during the design phase. The calibration has been performed using the Coriolis mass flow meter as the reference measurement.

As previously described (see section 3.5), HT orifice is a converging-diverging venturi, while GG orifice is a simple sonic one, for construction constraints. For the HT line, the diverging part of the orifice is designed to recover part of the pressure lost in the converging section.

During the whole engine test campaign, O2 GG mass flow is measured by the Coriolis flow meter, so the calibrated relation 4.42 provides a double check. On the other hand, the mass flow measurement of the O2 HT line is performed only by measuring the pressure upstream the sonic orifice after calibration.

Figure 4.13 reports a schematic of the pneumatic circuit adopted both for HT and GG sonic orifice characterization.

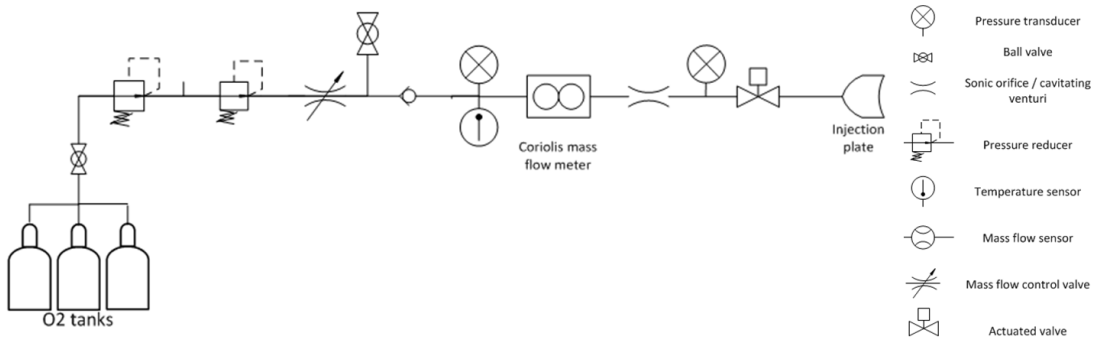

Figure 4.13: Setup scheme for the sonic orifices calibration; the reader is referred to figure 3.12 for the symbols' legend

The oxygen tank package has been connected to the feeding lines through two single stage pressure regulators. A needle valve downstream permits the fine regulation of the upstream pressure.
An electro-actuated ball valve is mounted just before the sonic orifice to control the gas adduction.
Pressure is measured by means of two sensors, mounted respectively upstream and downstream the sonic orifice. Total temperature is measured by means of a J thermocouple located in the same section of the upstream pressure sensor.

The calibration of the sonic orifices had also the scope of evaluating their choking limit, which is the maximum downstream pressure which guarantees the choked condition in correspondence of the throat section.
From this point of view, the HT orifice has a wider range of acceptable downstream pressure, because the orifice is provided by a diverging part downstream the throat: so the downstream pressure can largely exceed the choking value. On the contrary, the GG orifice can operate in choking conditions only if the downstream pressure is below the choking value. This is the reason why two orifices with different throat section have been needed (see section 3.5).

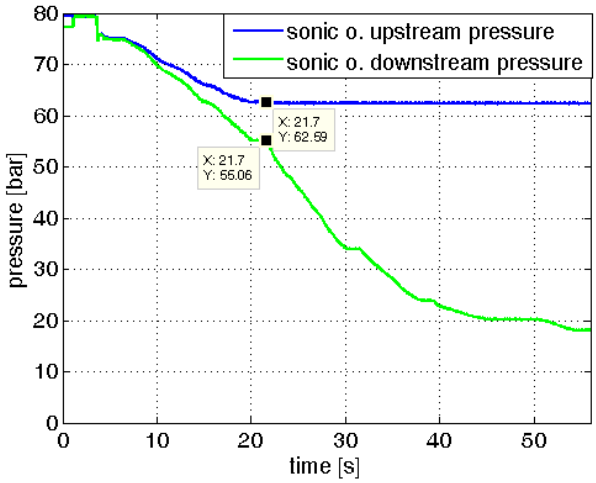

Figure 4.14: HT sonic orifice upstream and downstream pressure, during the choking-limit evaluation tests

To perform the choking limit evaluation, the circuit has been slightly modified respect to the configuration shown in figure 4.13: to regulate the downstream condition a needle valve has been mounted, completely closed at the beginning.
The electro-pneumatic ball valve has been left opened and to completely fill up the line. The needle valve has been progressively opened to let the oxygen flow out.
Up to a characteristic cross section the needle valve is choked and the sonic orifice works in subsonic mode, then the choking condition arise in the orifice, and from this point it can be seen clearly that the downstream pressure has no influence on the upstream pressure (see figure 4.14).

To ensure the choked condition of the orifice, the downstream pressure has to be ap-

proximately less than 88% respect to the upstream value, for the HT orifice, and less than 53%, for the GG orifice.

As an example, figure 4.14 shows the choking limit for the hybrid torch sonic orifice at 50% modulation:

Figure 4.15 reports an example of data acquisition, during the calibration of the sonic orifice for the GG feed line: upstream pressure was modulated dynamically acting on the second stage pressure regulator and waiting for the Coriolis meter to get the steady state value for each pressure level.

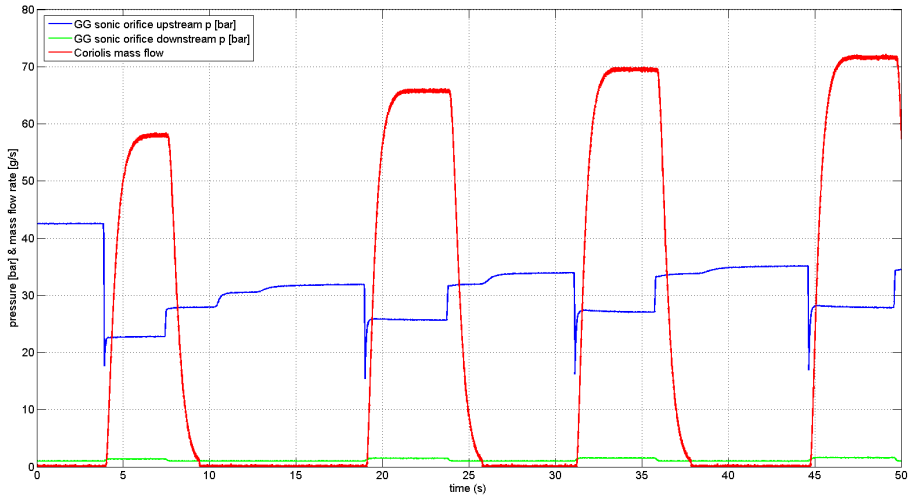

Figure 4.15: O2 GG sonic orifice calibration: the information provided by the Coriolis mass flow meter and the upstream pressure sensor are combined to evaluate the discharge coefficient of the orifice

For a major accuracy, the discharge coefficients have been calculated at different mass flow rate modulations.

The final values of $C_{d,HT}$ and $C_{d,GG}$ have been evaluated averaging all the data collected, and reported in table 4.18, 4.19 and 4.20 respectively. Table 4.17 reports these results.

As far as the HT discharge coefficient is concerned, it has been evaluated excluding the no-linearity range, that is the mass flow rates below 0.019 kg/s; this choice in order to have a more accurate estimation of the coefficient in the operative mass flow rate range.

The final uncertainty of the coefficients have been estimated propagating the error for the averaging-operation.

Tables 4.18, 4.19 and 4.20 summarize all the calibrations sequences, for the HT orifice, for the smaller GG orifice (i.e. $\phi = 3\,mm$) and for the larger one (i.e. $\phi = 3.7\,mm$) respectively.

In figures 4.16, 4.17 and 4.18, the discharge coefficient and the upstream total pressure are plotted as a function of the mass flow rate, for the HT feed line and the for the two orifices of the GG feed line respectively.
It can be seen that the discharge coefficient has a slight variation, as a function of the mass flow rate. This is more evident for the HT feed line (see fig. 4.16), at very low mass flow

Orifice	C_d	**Uncertainty**
O2 HT, $\phi 2$	0.96	0.02
O2 GG, $\phi 3$	0.924	0.007
O2 GG, $\phi 3.7$	0.939	0.006

Table 4.17: Oxygen feed lines calibration: final discharge coefficients

rates, where the device loses its linear behavior. The upstream pressure is a linear function of the mass flow rate.

Table 4.18: O2 HT feed lines calibrations: discharge coefficients evaluation

Hybrid torch feed line					
Mass flow rate [kg/s]	**Uncertainty [kg/s]**	**Pressure [bar]**	**Uncertainty [bar]**	C_d	**Uncertainty**
0.0046	0.0003	6.6	0.2	0.88	0.07
0.0100	0.0003	13.4	0.1	0.93	0.05
0.0190	0.0004	25.1	0.1	0.95	0.05
0.0293	0.0004	38.1	0.0	0.96	0.05
0.0379	0.0005	49.2	0.2	0.96	0.05
0.0482	0.0005	62.2	0.1	0.97	0.05
0.0465	0.0004	60.3	0.1	0.96	0.05
0.0488	0.0005	63.4	0.1	0.96	0.05

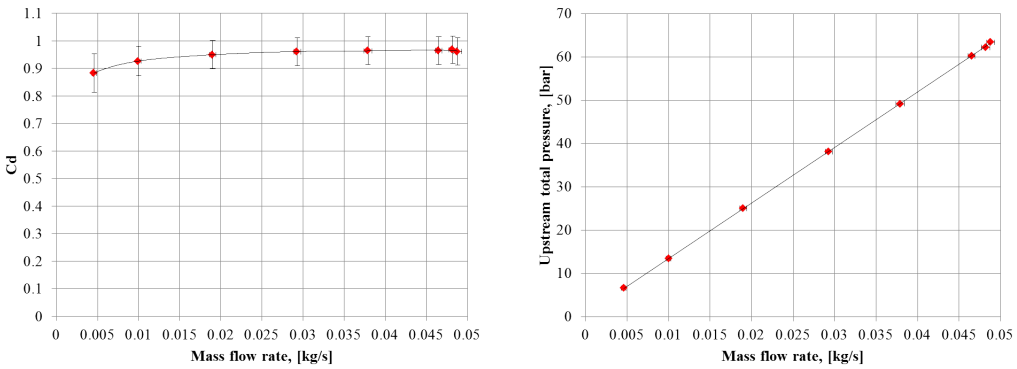

(a) (b)

Figure 4.16: O2 HT feed line calibration: (a) shows the discharge coefficient as a function of the mass flow rate; (b) shows the correspondent upstream pressure required to produce the specific mass flow rate

Table 4.19: O2 GG feed lines calibrations: discharge coefficients evaluation, $\phi 3$ mm orifice

Gas generator feed line, $\phi 3$ mm orifice					
Mass flow rate [kg/s]	**Uncertainty [kg/s]**	**Pressure [bar]**	**Uncertainty [bar]**	C_d	**Uncertainty**
0.0669	0.0005	40.1	0.1	0.93	0.03
0.0554	0.0005	33.8	0.1	0.91	0.03
0.0593	0.0005	35.9	0.1	0.92	0.03
0.0613	0.0006	37.1	0.1	0.92	0.03
0.0653	0.0006	39.4	0.1	0.92	0.03
0.0683	0.0006	41.0	0.1	0.93	0.03
0.0665	0.0005	39.8	0.1	0.93	0.03
0.0573	0.0005	34.6	0.1	0.92	0.03
0.0576	0.0005	34.8	0.1	0.92	0.03
0.0582	0.0005	35.2	0.1	0.92	0.03
0.0664	0.0004	40.1	0.1	0.92	0.03
0.0690	0.0004	41.5	0.1	0.93	0.03
0.0690	0.0006	41.7	0.1	0.92	0.03
0.0693	0.0007	41.7	0.1	0.92	0.03
0.1067	0.0005	65.1	0.1	0.93	0.03
0.1056	0.0005	64.1	0.1	0.93	0.03
0.1044	0.0005	63.3	0.1	0.93	0.03
0.1037	0.0005	62.9	0.1	0.93	0.03
0.1039	0.0006	63.2	0.1	0.93	0.03
0.0689	0.0005	42.3	0.1	0.92	0.03
0.0688	0.0008	41.6	0.1	0.92	0.03
0.1014	0.0005	61.0	0.2	0.92	0.03
0.1036	0.0006	62.0	0.2	0.93	0.03

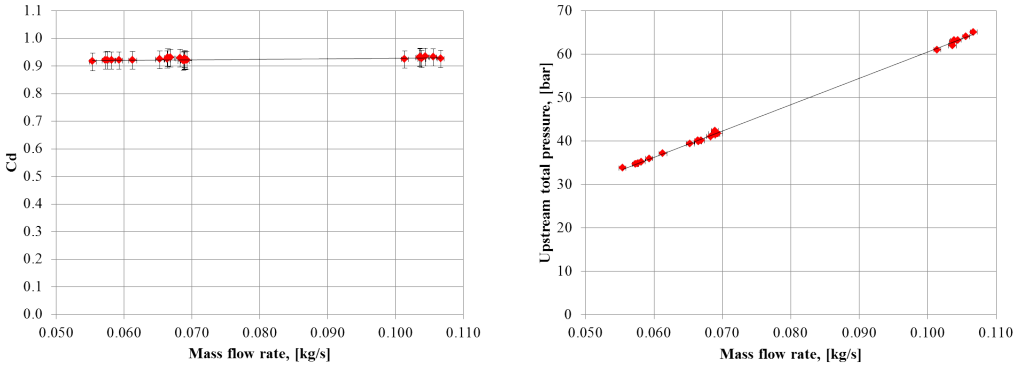

(a) (b)

Figure 4.17: O2 GG feed line calibration, $\phi 3$ mm orifice: (a) shows the discharge coefficient as a function of the mass flow rate, for the smaller orifice; (b) shows the correspondent upstream pressure required to produce the specific mass flow rate, for the smaller orifice

Table 4.20: O2 GG feed lines calibrations: discharge coefficients evaluation, ϕ3.7 mm orifice

Gas generator feed line, ϕ3.7 mm orifice					
Mass flow rate [kg/s]	**Uncertainty [kg/s]**	**Pressure [bar]**	**Uncertainty [bar]**	C_d	**Uncertainty**
0.0923	0.0005	35.9	0.1	0.937	0.026
0.0917	0.0006	35.7	0.2	0.938	0.026
0.0580	0.0005	22.8	0.1	0.928	0.026
0.0658	0.0004	25.7	0.1	0.933	0.026
0.0695	0.0005	27.1	0.1	0.935	0.026
0.0716	0.0004	27.9	0.1	0.937	0.026
0.0717	0.0006	27.9	0.1	0.937	0.027
0.0891	0.0008	34.5	0.3	0.943	0.028
0.0760	0.0004	29.6	0.2	0.938	0.027
0.0537	0.0004	21.0	0.1	0.934	0.027
0.0364	0.0004	14.3	0.1	0.930	0.028
0.0715	0.0006	27.9	0.1	0.933	0.026
0.1346	0.0009	53.3	0.2	0.934	0.026
0.1381	0.0006	54.3	0.2	0.940	0.026
0.1410	0.0007	54.8	0.2	0.952	0.026
0.1411	0.0008	54.6	0.2	0.954	0.027
0.1404	0.0005	54.2	0.2	0.958	0.026
0.1347	0.0005	53.0	0.1	0.937	0.026
0.1409	0.0005	55.3	0.1	0.940	0.026
0.1405	0.0012	54.6	0.1	0.951	0.027

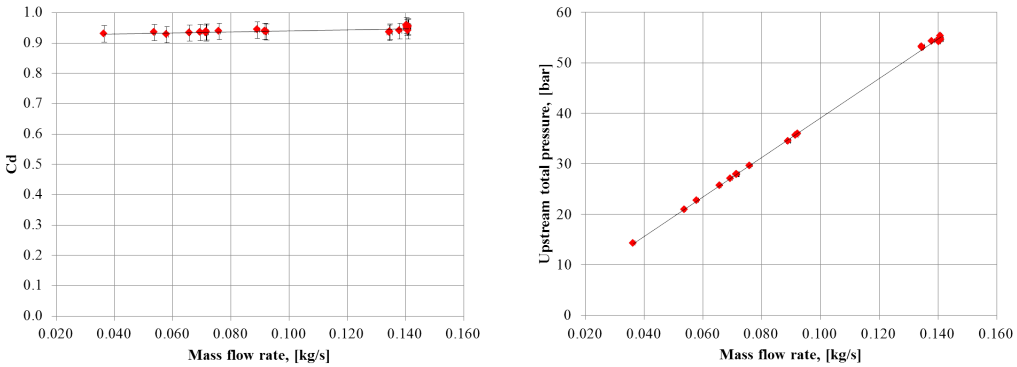

(a) (b)

Figure 4.18: O2 GG feed line calibration, ϕ3.7 mm orifice: (a) shows the discharge coefficient as a function of the mass flow rate, for the larger orifice; (b) shows the correspondent upstream pressure required to produce the specific mass flow rate, for the larger orifice

4.4.2 Water Feed Line

As described in chapter 3, the water mass flow is controlled by a cavitating venturi, specifically designed for this purpose.
The formulation, that describes the cavitating venturi behavior, is reported below for convenience:

$$\dot{m}_{h2o} = C_d A_{cv} \sqrt{(2\rho\,(p_i - p_{sat}))} \tag{4.43}$$

where water vapor pressure p_{sat} depends on water temperature, according to the Antoine equation [45]:

$$log_{10}\left(p_{sat,[bar]}\right) = A - \frac{B}{T_{[K]} + C} \tag{4.44}$$

Temperature range, [K]	A	B	C
[273-303]	5.40221	1838.675	-31.737

Table 4.21: Antoine equation parameters for water

Thus the mass flow rate through the piping depends on:

- fluid properties (ρ, p_{sat}, T);
- upstream pressure, p_i;
- cavitating venturi throat section, A_{cv};
- discharge coefficient, C_d.

Basically, once the upstream pressure is set, the mass flow rate is univocally determined, and decoupled from downstream phenomena. Since wide variations of the upstream pressure are required to span the mass flow rate range, two cavitating venturi have been designed and manufactured; the smaller (#1) to be used for 50% and 75% throttling level, and the larger (#2) for 100% throttling level.

During calibration, the upstream pressure has been set to different levels and the corresponding mass flow rate has been deduced, to evaluate the actual discharge coefficient of the piping. This information is needed to calculate the right upstream pressure required to supply the desired mass flow rate.
Two different mass flow rate measurement devices have been used (see table 4.1 for main measuring performance):

1. a magnetic flow meter, which gives a very accurate measure, but is affected by a long response time;
2. linear potentiometer, connected to the pressurizing piston; in this case, mass flow rate can be derived from the position of the piston, and the geometrical characteristics of the cylinder (i.e. its internal cross section, A_{piston}), thanks to water incompressibility.

The measurement provided by the magnetic flow meter has been also a reference, to verify the reliability of the mass flow rate indirect estimation through the linear potentiometer signal.

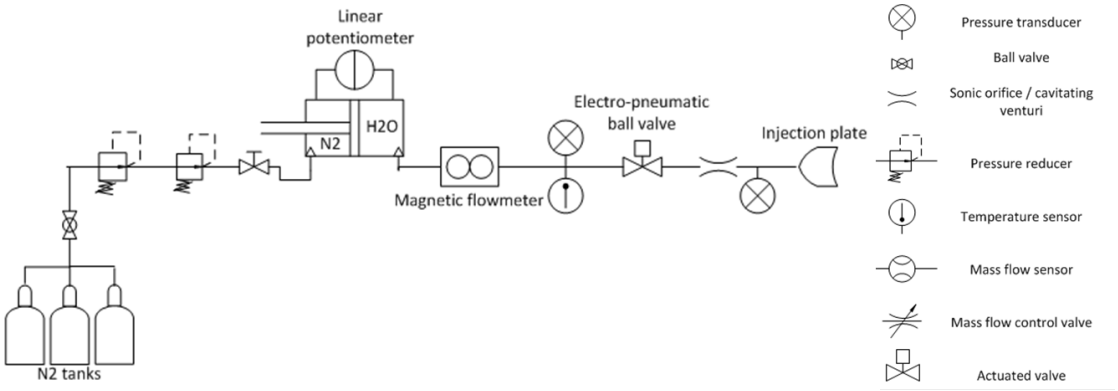

Figure 4.19: Setup scheme for the cavitating venturi calibration; the reader is referred to figure 3.12 for the symbols' legend

Figure 4.19 reports a schematic of the setup used for the water feed line calibration. In the whole engine test campaign, the magnetic flow meter has not been mounted.

Water tank is pressurized using nitrogen by means of a sliding piston, whose position (L_{tank}) is measured dynamically by means of the linear potentiometer. Thus water mass flow rate can be deduced from the variation of volume occupied inside the tank, as follows:

$$\dot{m}_{h2o} = \rho_{h2o} A_{piston} \frac{\delta L_{tank}}{\delta t} \tag{4.45}$$

Water discharge is operated in blow down mode: to limit the pressurization variation during discharge, a large reservoir has been connected to the piston tank, on the nitrogen side; thus the large capacity of the pressurizing volume mitigate the pressure loss.
Considering the water operative pressure and flow rate at each throttling level, acceptable variations during discharge have been predicted:

- 50% throttling level, with a 13 s long discharge: $\sim$ 2.3% pressure decrease, thus $\sim$ 1.2% mass flow rate decrease;
- 75% throttling level, with a 13 s long discharge: $\sim$ 3.5% pressure decrease, thus $\sim$ 1.8% mass flow rate decrease;
- 100% throttling level, with a 13 s long discharge: $\sim$ 4.5% pressure decrease, thus $\sim$ 2.3% mass flow rate decrease.

This variations extent has been confirmed in the whole engine test campaign.
As an example, figure 4.20 reports potentiometer and upstream pressure signal for a 50% throttling discharge. It can be seen the slight variation of the upstream pressure (green curve).

Figure 4.21 compares the three different methods used to evaluate water mass flow rate: by means of magnetic flow meter (red line), by means of time-derivation of linear

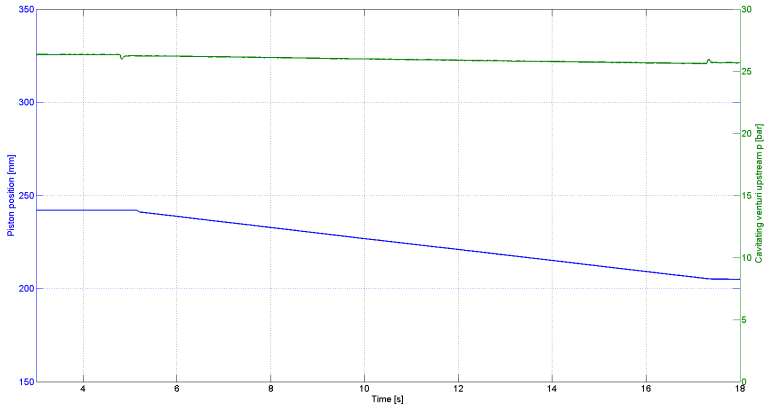

Figure 4.20: Cavitating venturi calibration: 50% throttling level discharge; the linear potentiometer (blue line) and upstream pressure (green line) signal are shown

potentiometer signal (blue line), and by means of isentropic formulation corrected by the discharge coefficient (green line) as stated in eq. 4.44.
Potentiometer signal has been fitted and derived in data post-processing to filter the acquisition noise and make the time derivation feasible, according to eq. 4.45. Figure 4.22 compares the rough data with the fitted curve.

Figure 4.21 confirms the low response time proper of the magnetic flow meter and the choice of using it just during calibration, as a check of the mass flow rate steady state value.

Finally tables 4.22 and 4.23 summarize the results of the calibration tests performed, for the smaller (i.e. ϕ1.1 mm) and the larger (i.e. ϕ1.38 mm) orifice, respectively. The same data are then plotted in figure 4.23; it can be seen that the discharge coefficient in these cases is almost a constant function of the mass flow rate (fig. 4.23a and 4.23c). The upstream pressure is a linear function of the mass flow rate (fig. 4.23b and 4.23d).

The final values of C_d has been evaluated averaging all the data collected. Table 4.24 reports these results.

The final uncertainty of the coefficients have been estimated propagating the error for the averaging-operation.

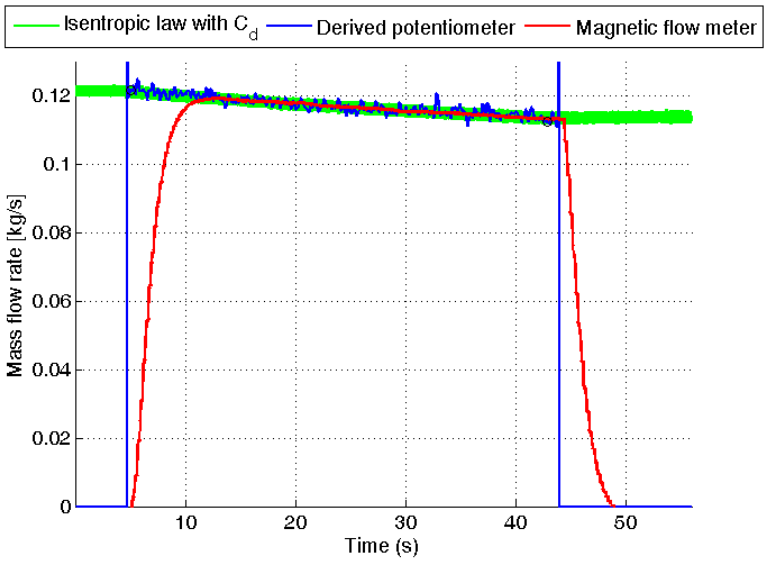

Figure 4.21: Cavitating venturi calibration: water mass flow rate for a 100% throttling level discharge; magnetic flow meter signal (red curve) is compared with linear potentiometer derivation (blue curve) and isentropic calculation with discharge coefficient (green curve)

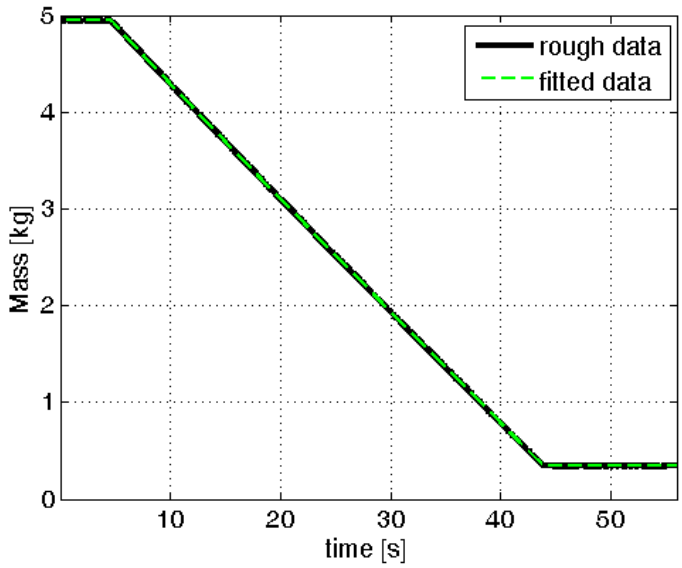

Figure 4.22: Cavitating venturi calibration: fitting of the linear potentiometer signal

Table 4.22: H2O feed line calibrations: discharge coefficients evaluation, ϕ1.1 mm orifice

ϕ1.1 **mm orifice**					
Mass flow rate [kg/s]	**Uncertainty [kg/s]**	**Pressure [bar]**	**Uncertainty [bar]**	C_d	**Uncertainty**
0.0617	0.0002	34.1	0.7	0.79	0.02
0.0923	0.0003	76.3	2.7	0.79	0.02
0.0920	0.0002	77.3	2.5	0.78	0.02
0.0924	0.0003	76.2	2.7	0.79	0.02
0.0621	0.0003	34.5	0.8	0.79	0.02
0.0622	0.0002	34.6	0.8	0.79	0.02
0.0603	0.0002	33.7	0.9	0.77	0.02
0.0608	0.0001	34.6	1.0	0.77	0.02
0.0902	0.0003	76.2	3.2	0.77	0.02

Table 4.23: H2O feed line calibrations: discharge coefficients evaluation, ϕ1.38 mm orifice

ϕ1.38 **mm orifice**					
Mass flow rate [kg/s]	**Uncertainty [kg/s]**	**Pressure [bar]**	**Uncertainty [bar]**	C_d	**Uncertainty**
0.0886	0.0002	24.9	1.8	0.84	0.03
0.0891	0.0002	24.9	2.1	0.84	0.04
0.1046	0.0002	34.6	2.7	0.84	0.04
0.1042	0.0002	34.6	2.1	0.84	0.03
0.1224	0.0002	47.6	3.7	0.84	0.03
0.1255	0.0002	50.4	3.3	0.84	0.03
0.1171	0.0002	43.6	5.2	0.84	0.05
0.1297	0.0003	54.3	1.9	0.83	0.02

Orifice	C_d	**Uncertainty**
ϕ1.1	0.781	0.006
ϕ1.38	0.838	0.012

Table 4.24: Water feed line calibration: final discharge coefficients

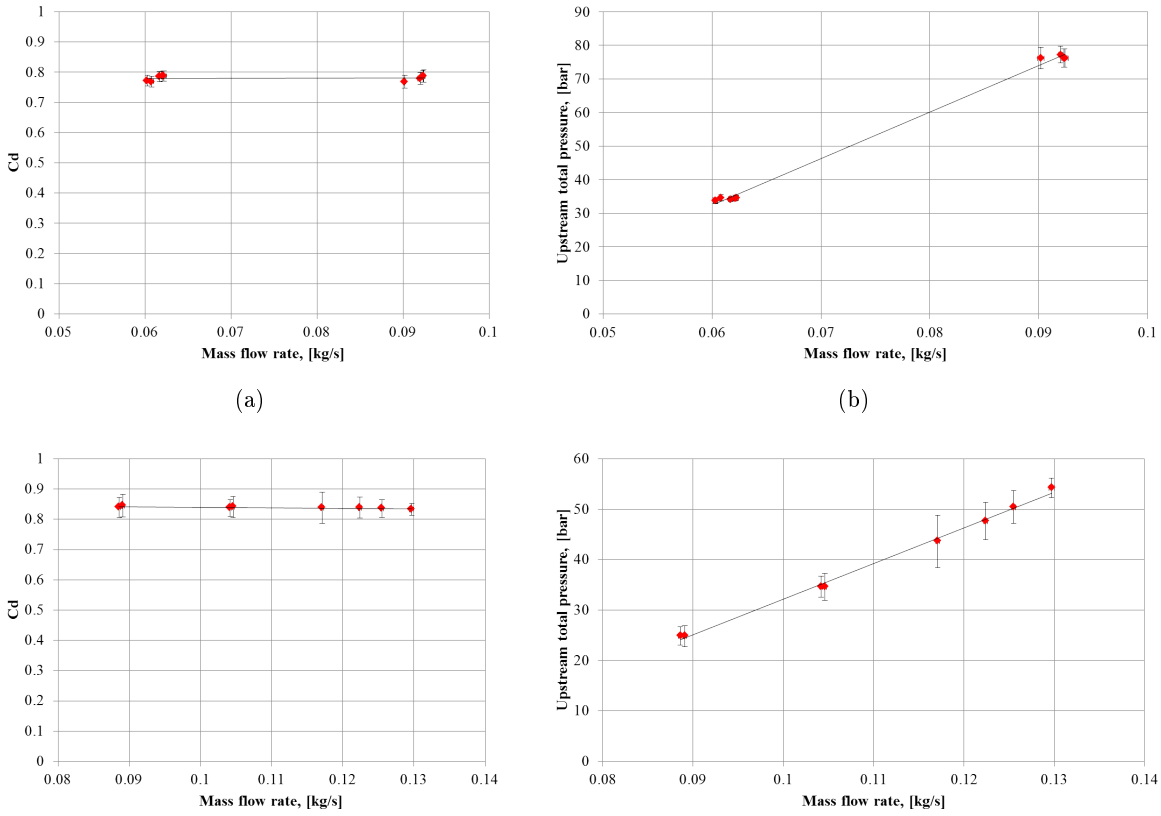

Figure 4.23: H2O GG feed line calibration: (a) and (c) show the discharge coefficient as a function of the mass flow rate, for the smaller and the larger venturi respectively; (b) and (d) show the correspondent upstream pressure required to produce the specific mass flow rate, for the smaller and the larger orifice respectively

Chapter 5

Test Campaign

5.1 Methodology

A step-by-step verification of each subsystem composing the whole assembly has been performed, in order to get its correct functioning; so the experimental activity has been structured in different phases, before performing the complete engine tests.

After the calibration of the feed lines, four main phases can be identified, which involved different subsystems of the whole assembly:

1. hybrid torch functioning;
2. hybrid torch plus gas generator coupled functioning;
3. hybrid torch plus gas generator optimization;
4. complete engine functioning and throttling.

For safety reasons, tests have been conducted with increasing mass flow rates and time lasting.

3 throttling levels have been tested:

- 50%,
- 75%,
- 100%.

For each level, at least 3 tests have been performed for reliability.

The following subsections illustrate the main outcomes of each phase above listed.

5.1.1 Phase 1: Hybrid Torch Functioning

The optimization of HT functioning is the result of a synergy between numerical investigation and experimental verification.

Hybrid torch has been individually tested for two main reasons:

1. to characterize its effective $\dot{r} \propto Gox$ correlation, and thus its mean OF ratio;

2. to evaluate its combustion efficiency, and thus the completeness of reactants turbulent mixing and reaction;

Moreover, preliminary tests of hybrid torch have been useful also to provide experimental data for the analytic model illustrated in section 4.2.1.

As already said, the role of the hybrid torch is to provide a heat flux to the gas generator, in order to:

- vaporize water, injected into GG chamber;
- heat up both oxygen and water vapor, and at the same time activate recombination processes for the HT combustion products, thus to obtain a oxygen-water based mixture (with some impurities, i.e. *CO2*), with a temperature around 650 °C.

In this perspective, the actual OF ratio of the hybrid torch is required to estimate the resulting GG mixture composition and temperature. On the other hand, combustion efficiency estimation is needed to evaluate how far is the real HT combustion from the ideal, and perfectly mixed condition.

Hybrid torch has been designed to work with a mean OF ratio as close as possible to the stoichiometric value (i.e. 3), since this value correspond to the maximum achievable flame temperature, and thus to the maximum thermal energy provided to the GG mixture.

According to this requirement, the diverging part of the HT nozzle is designed to recover pressure and to work in subsonic mode, so the thermal energy is preserved and not converted to kinetic energy. HT nozzle throat has been designed to guarantee pressure decoupling between HT and GG; this aspect has been found critical just during the ignition transient, when GG is still at ambient pressure and hybrid torch needs to increase its operating pressure in order to ignite properly.

HT combustion efficiency is critical too: as long as a high efficiency is guaranteed, an almost completely reacted mixture is expected to enter the gas generator chamber, at a temperature close to the perfect chemical equilibrium value; in this case an almost uniform dilution of HT hot combustion products with oxygen and water is expected to happen in GG. But, as soon as the efficiency decreases, a stratified flowfield is expected in HT chamber, which is typical of classical hybrids with axial injection. In this latter situation, not just recombination and heating up are expected to take place in GG, but also chemical reactions between unburnt reactants, localized where the local OF facilitates them; so the final mixture composition can be not perfectly reacted and mixed.

The very first tests performed on the hybrid torch were those at 50% throttling level, with design-length of HDPE grain.

The outcome of this phase is the actual length of the HDPE grain in order to obtain a mean OF ratio equal to 3.

5.1.2 Phase 2 and 3: Hybrid Torch and GG Coupled Functioning and Optimization

Respect to the HT design configuration, several changes have been required, once the hybrid torch had been tested in its coupled functioning with GG, in order to:

1. to increase the total thermal flux provided to GG mixture;

2. to enhance the combustion efficiency;

In fact, thermal dispersion has forced to increase the heat flux provided by the hybrid torch, to guarantee a high temperature mixture, and thus HTPB ignition. Moreover, hybrid torch combustion efficiency has been increased, in order to maximize the temperature of its combustion products, and thus to increase the effectiveness of GG mixture heating up.

These steps have been performed on the 50% throttling configuration, which has demonstrated to be the most demanding, in terms of HTPB ignition capability. Then the improvements made have been applied even to the other throttling configurations, in order to test the motor assembly in identical configurations and conditions.

The outcome of these phases is an optimized configuration of the hybrid torch in order to assure the right GG mixture temperature and composition.

5.1.3 Phase 4: Complete Engine Functioning and Throttling

As far as the whole assembly testing is concerned, 3 throttling levels have been tested: 50%, 75% and 100%. For each level, at least 3 tests have been performed for reliability.

The most important information obtained in this phase have been:

- regression rate as a function of specific mass flow rate;
- combustion efficiency;
- combustion stability, in terms of combustion chamber pressure oscillations;
- HTPB ignition capability and delay;
- nozzle throat erosion issues.

The main results of these four phases are reported in the following sections.

5.2 Phase 1: Results

Main hybrid torch preliminary results have been already shown in table 4.4, reported below for convenience (tab. 5.1). Figure 5.1 shows the corresponding geometrical configuration.

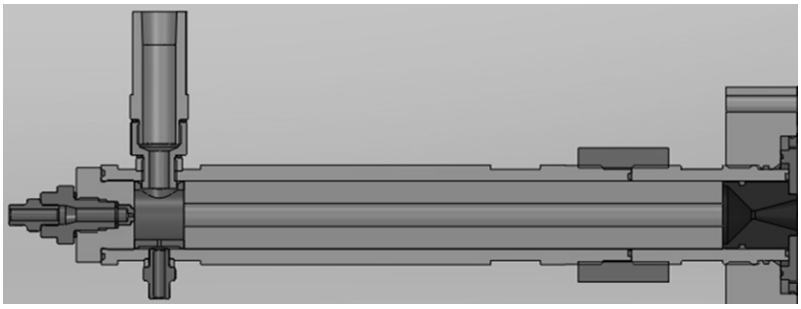

Figure 5.1: Hybrid torch preliminary tests: first configuration

As it can be seen from the data, HT functioning is extremely repeatable.

	HT #14	HT #15	HT #16	uncertainty [% RD]
oxidizer mean mass flow rate, [kg/s]	0.0194	0.0192	0.0192	<5.6
fuel mean mass flow rate, [kg/s]	0.0089	0.0088	0.0087	<5.5
mean chamber pressure, [bar]	22.3	22.4	22.3	<6.4[1]
mean characteristic velocity, [m/s]	1574	1581	1590	<6.4
efficiency, [%]	87	88	88	

Table 5.1: Hybrid torch preliminary test data

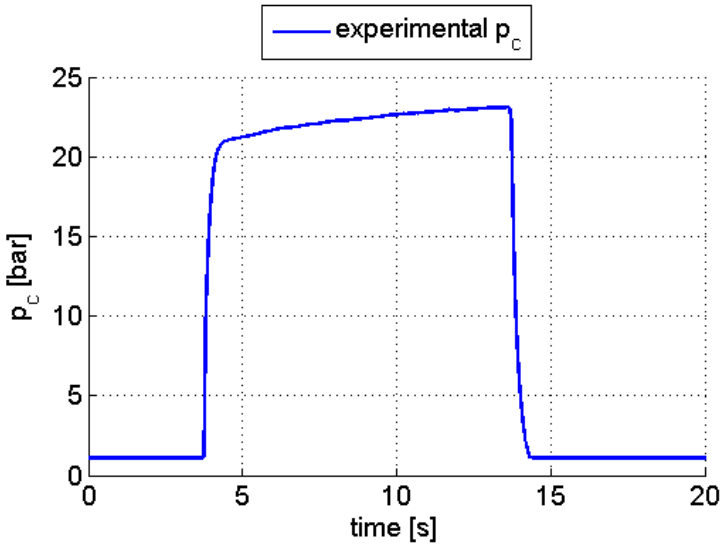

Figure 5.2: Hybrid torch preliminary tests: example of combustion chamber pressure (filtered)

Observing the typical combustion chamber pressure signal, reported in figure 5.2), it can be noted that fuel regression is slightly progressive. No nozzle erosion has been encountered.

Low combustion efficiency has been obtained; this can be justified by several factors: the injection is axial single hole, hybrid torch had neither post combustion chamber nor mixing devices, to enhance the mixing. For these tests the hybrid torch nozzle has worked with ambient pressure at the exit and so the flow exited the nozzle in supersonic condition to slightly re-compress at the outlet.

In this phase, experimental regression rate was found to be 24% higher than expected according to design prediction (see table 3.3), thus determining a OF value equal to about 2.3 instead of the desired ≈3; besides a minor flame temperature, the consequence of a fuel rich combustion is a major quantity of impurity introduced by CO2 in the GG mixture. Therefore the HDPE grain length has been reduced to set the hybrid torch to the desired

mean fuel flow rate; the new grain length has been estimated, taking advantage of the analytic model developed, and discussed in section 4.2.1.
Moreover, a post-combustion chamber has been added at the end of the grain, to mitigate the combustion inefficiency.

An additional modification has been introduced, regarding nozzle configuration: since the nozzle has to work choked at the throat but in subsonic mode downstream it, a less steep angle (5°instead of 15°) has been set for the diverging cone, in order to gently guide the flow without separation.
Figure 5.3 shows the HT second configuration schematic, as resulted from these changes.

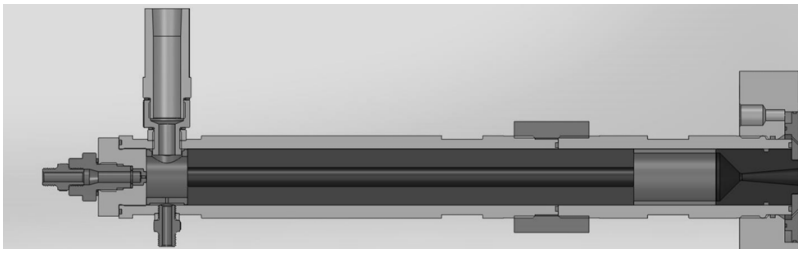

Figure 5.3: Hybrid torch preliminary tests: second configuration

This configuration has been adopted to start the following phase of HT-GG coupled functioning.

5.3 Phase 2: Results

HT-GG coupled functioning tests have been performed with a calibrated orifice, mounted downstream GG, in place of the vortex injector; this solution granted the gas generator to work at an operative pressure similar to the one expected to settle by CC combustion, in the whole engine testing.

The first tests performed on HT plus GG denoted a low temperature of the GG mixture, respect to the required and expected value. Two main causes explain this lower temperature:

1. heat losses towards the whole engine steel structure, and especially towards the gas generator chamber walls;

2. mixing and recombination process incompleteness inside GG.

It has been estimated that a margin of ≈15% was needed, respect to the predicted theoretical value of mixture temperature, to compensate these losses, and thus to assure HTPB ignition in a reasonable time; this could be achieved increasing the heat flux provided to the mixture. Thus, the heat flux coming from the hybrid torch combustion has been enhanced, increasing O2 flow rate, in order to obtain from CEA a theoretical mixture temperature at least 150 K higher than the required value ($\approx 923\,\mathrm{K}$).

[1] Uncertainty has been calculated considering the combustion chamber whole operative range, respect to the mean value calculated (see figure 5.2).

This solution has been effective to increase the mixture temperature. Thus the different mass flow rate contributions have been adjusted accordingly, respect to the design values, at each throttling level. The 0D analytic model described in chapter 4.1 has been used to estimate the mean regression rate of the hybrid torch, given a certain length of the grain. The final adjustment of mass flow rates has led to an average OF ratio for the hybrid torch equal to ≈2.8; this value has been considered acceptable, considering that a slightly fuel rich combustion is better in terms of nozzle erosion. Table 5.2 reports the adjusted mass flow rates.

Throttling level	$\dot{m}_{O2}$ **HT** **[kg/s]**	$\dot{m}_{HDPE}$ **[kg/s]**	$\dot{m}_{O2}$ **GG** **[kg/s]**	$\dot{m}_{H2O}$ **GG** **[kg/s]**
50 %	0.022	0.0079	0.069	0.063
75 %	0.035	0.0124	0.104	0.094
100 %	0.045	0.0158	0.139	0.125

Table 5.2: Mass flow rates at different throttling levels: design review

Once adapted the heat flux from the hybrid torch, a first test has been performed on the whole engine assembled.
HTPB was able to ignite, but after a time lag of 10.6 s: during this time range, GG oxidizer exits the CC nozzle unburnt, and so the motor behaves like a monopropellant thruster. This lag is due to several factors:

- incomplete mixing/heating up of the mixture produced in GG;
- gas generator walls absorb and waste heat towards the ambient;
- HTPB grain must be heated up to the pyrolysis temperature to permit ignition.

Figure 5.4 shows CC and GG pressure and temperature signals during this test: HTPB ignition can be recognized by the rapid rising of the pressure signal about 10 s after the hybrid torch ignition.

Temperature signal correspond to the thermocouple located in GG, close to the vortex injector.
It can be observed that the temperature signal is monotonically increasing during the test; two hypothesis can possibly explain this behavior.

1. Stratified flowfield is expected in HT chamber, without the mixer. In this situation, not just recombination and heating up are expected to take place in GG, but also chemical reactions between unburnt reactants, localized where the local OF facilitates them. So hot spots are expected to settle in this case, which make the temperature distribution inside GG nonuniform, and thus temperature measurement inside GG representative of a local not global condition.

2. With the proceeding of HT nozzle throat erosion, the focusing of the flame exiting the HT nozzle changes, and thus changes the forced convection, which the thermocouple is subjected to.

In the opinion of the author the temperature measurement is affected by a combination of these two aspects.

Figure 5.4 reports also the hybrid torch chamber pressure. A constant pressure decrease can be observed during the burning time: this is caused by HT nozzle throat erosion. When HTPB ignites and CC pressure increases to the operative level, HT nozzle throat is no longer choked, and HT-GG-CC work coupled. HT nozzle throat erosion is linked to combustion inefficiency: incomplete turbulent mixing of chemical species upstream the nozzle cause chemically reacting species at high temperature to attack graphite. Unburnt reactants are expected to enter GG; thus, chemical reactions with unreacted C2H4 take place in GG, where the local OF is suitable. In this case, GG temperature is expected to be nonuniform; moreover, locally it can exceed the value corresponding to GG ideal functioning, that is basically HT combustion products dilution and recombination. Finally, since the HT combustion is not complete, a less effective heat flux is provided by HT combustion products.

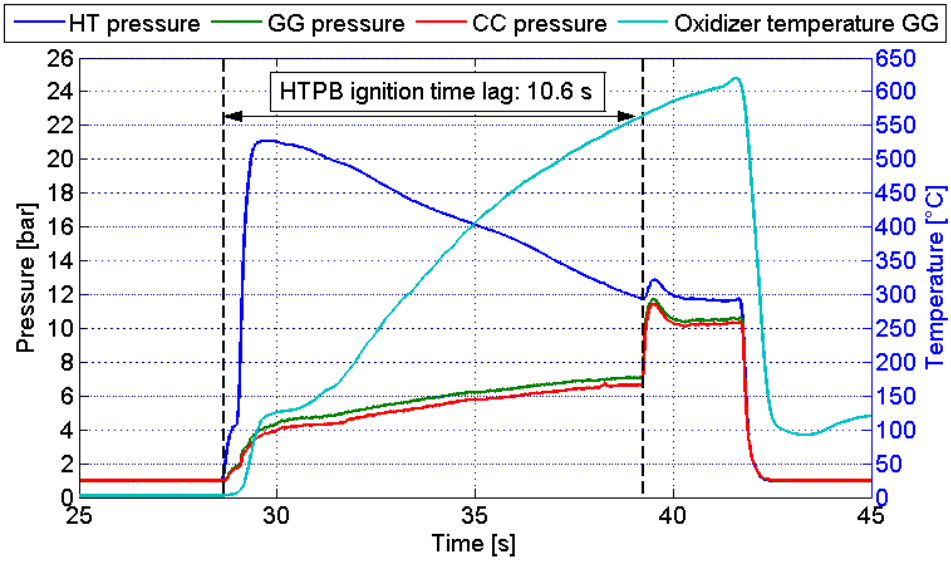

Figure 5.4: HTPB ignition, with improved HT heat flux: ignition takes place 10.6 s after HT ignition

5.4 Phase 3: Results

An additional modification has been introduced in the hybrid torch, to further mitigate the time lag in HTPB ignition. Combustion efficiency, and so product mixing at HT nozzle outlet, has been improved by adding an ablative mixing device inside the post-combustion chamber of the hybrid torch, in order to enhance the turbulent mixing. Several works, performed by UPD, have already demonstrated the effectiveness of such devices in increasing the motor performance [75], [12].

Figure 5.5 shows the corresponding HT configuration schematic. The ablative mixer design is confidential, so it has been hided.

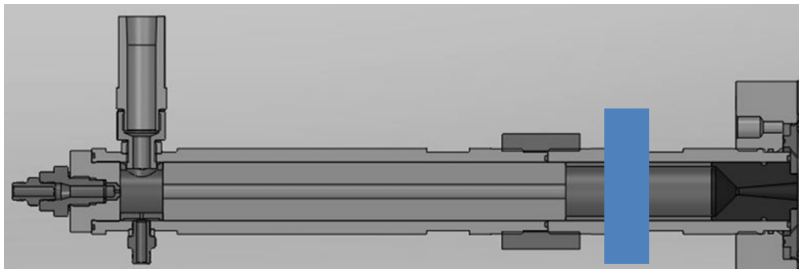

Figure 5.5: Hybrid torch optimization tests: final configuration; the mixer design if confidential, so it has been hided

This solution produced an efficiency improvement of 10% in HT combustion. The effectiveness of this change can be observed in figure 5.6.

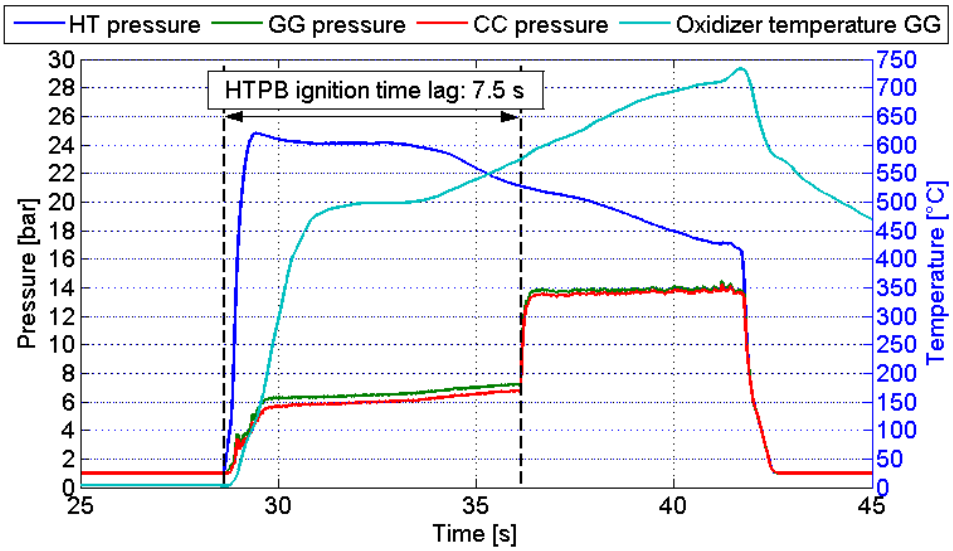

Figure 5.6: HTPB ignition, with improved HT combustion efficiency: ignition takes place 7.5 s after HT ignition

In this case, GG temperature rising is faster, and the mixture reaches higher temperatures. It takes however 7.5 s for the HTPB to ignite, after the beginning of the test.

The mixer is ablative; a low regression rate material has been chosen, to guarantee its lasting for a certain time. Mixer has been used to speed up the heating-up process of GG mixture, as long as the HTPB is not ignited.

Considering HT chamber pressure profile, a sudden change of trend can be observed, after approximately 6 s. This is due to the mixer complete consumption: as soon as the mixer is not present, combustion becomes inefficient, and so nozzle throat erosion is

observed. Chemical reactions start taking place in GG, as in the previous case, and this explains the temperature rising, as soon as the HT nozzle starts eroding.

It has to be noted that the mixer has already been totally consumed, once HTPB ignites; thus mixer does not introduce any further impurity in the oxidizer mixture, during CC combustion.

The test reported in figure 5.6 has a total duration of 13 s; thus 5.5 s of CC functioning are guaranteed.

It can be seen that in this case the thermocouple in GG measures a constant temperature while the mixer is working and the HT nozzle is not eroded; as soon as the nozzle throat starts eroding the temperature measurement changes, thus suggesting a change in the forced convection to the thermocouple.

5.4.1 Nozzle throat erosion

13 seconds of hybrid torch burning have been required, to provide a CC stable functioning of approximately 5/6 seconds, at 50 % throttling level.

The O2-HDPE combustion products reach a temperature up to 3600 K, so the hybrid torch nozzle is subjected for several seconds to extreme heating in an oxidizing ambient. As a consequence, nozzle throat erosion has been observed: in the worst case (no mixer included), nozzle throat diameter has changed from 5.5 mm at the beginning of the hot test to 8 mm at the end, thus the throat section resulting increased of about 21%, and the chamber pressure decreased of the same amount.

Several nozzle configurations have been designed and tested to find the best compromise between cost and HT performance: it has been observed that the hybrid torch performs better (higher regression rate) with high combustion chamber pressure (i.e. with small throat area nozzles), so it would be better to avoid or almost mitigate nozzle throat erosion.

Nozzle choking condition is mandatory just for the ignition phase of the hybrid torch, in order to guarantee its ignition; in fact, even a test with nozzle throat completely eroded has been tempted, but the hybrid torch failed to ignite: the dimension of the nozzle throat section prevented the hybrid torch from increasing its operating pressure during the ignition transient, when GG and CC were at ambient pressure.

The nozzle solutions tested are listed hereafter; figure 5.7 shows the correspondent CAD schematics.

1. stainless steel external housing, with an ablative (PE) insert for the throat;
2. stainless steel external housing, with a graphite insert for the throat;
3. graphite for the whole nozzle.

The first solution was effective in guaranteeing HT ignition, but PE consumption was very fast. A fast consumption is preferable, because it is expected a total consumption of the insert before HTPB ignites, and so no further impurities would have been introduced in the GG mixture. On the other hand, an insufficient thermal flux from the hybrid torch has been detected in this configuration. In fact, in this case, the hybrid torch worked most of the time coupled to the gas generator pressure (see figure 5.9a below); it has been observed that the lower is the operative pressure of the hybrid torch, on average, the lower

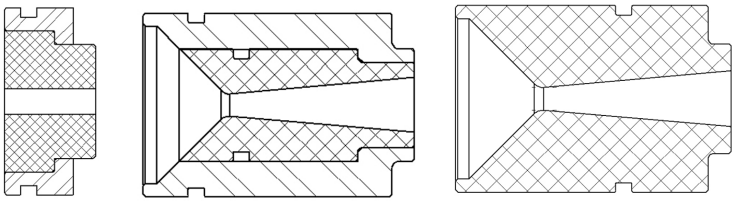

Figure 5.7: HT nozzle configurations investigated: stainless steel housing with PE insert (a), stainless steel housing with graphite insert (b) and entirely graphite (c)

is the mean fuel mass flow rate production, and thus the thermal flux provided to the gas generator. This aspect will be shown in a short while.

At this point, graphite has been adopted to build the nozzle, for its good thermal properties. Except for most sophisticated and expensive nozzle, whose throat is ceramic based, graphite is commonly used for short duration burns, because of its good compromise between costs and performance.
So the second solution had the aim of limiting the costs of raw material and manufacturing: the external housing was expected to always survive, while the insert would have been replaced when needed. According to experimental evidence, the nozzle insert should have been replaced after each test; moreover, a heavy erosion has been observed in the diverging part of the nozzle, close to the outlet: the bad thermal conductivity of stainless steel causes a strong overheating of the graphite, and thus its erosion to such an extent that the hot products lick the nozzle external housing. In this perspective there would be no convenience in adopting the second solution, respect to the third.

Finally the third solution has been selected, accepting to substitute the component after each test; costs have been mitigated by a stock purchase from a specialized seller.
Thanks to a thermal conductivity higher than the stainless steel, it is easier for a full graphite nozzle to drain heat flux; as a result, it takes a longer time for the nozzle to grow up its own temperature. This consideration, combined to the improvement in combustion efficiency due to the mixer in post-cc, has mitigated the chemical attack: nozzle throat diameter changed from 5 mm to 6.2 mm in 13 seconds hot tests.

As soon as the higher throttling level are considered, it is expected to detect a heavier erosion, since the thermal flux to the nozzle is increased.

Table 5.3 summarizes the most interesting results obtained during this investigation about nozzle erosion. Figure 5.9 reports the corresponding pressure signals.

As already mentioned, these tests confirmed a slight dependency of the resulting fuel mass flow rate from the operative pressure (see figure 5.8).
Referring to table 5.3, "spartan_23", "spartan_29" and "spartan_30" are characterized by the same nozzle configuration, but the last two tests have been performed with a thicker mixer, so its effect has lasted for more time; it can be seen that nozzle erosion starts earlier in "spartan_23" (fig. 5.9d) respect to "spartan_29" (fig. 5.9e) and "spartan_30" (fig. 5.9f). Also "spartan_29" and "spartan_30" behaved differently between each other: this is due to a different initial throat diameter, since in test "spartan_29" it was a 6% larger than in

"spartan_30".

Figure 5.8 reports the HDPE mean mass flow rate as a function of O2 mass flow rate for the cases just discussed.

Test case	**Nozzle**	**Mixer**	$\dot{m}_{O2}$ **HT, [kg/s]**	$\dot{m}_{HDPE}$**, [kg/s]**	ϕ_{th}**, [mm] before test**	ϕ_{th}**, [mm] after test**
spartan_20	PE insert	n	0.022±0.001	0.0070±0.0002	5.5±0.1	-
spartan_24	graphite	n	0.022±0.001	0.0075±0.0002	5.5±0.1	8±0.1
spartan_22	graphite insert	y	0.021±0.001	0.0078±0.0002	5.2±0.1	7±0.1
spartan_23	graphite	y	0.022±0.001	0.0079±0.0002	5.2±0.1	6.5±0.1
spartan_29	graphite	y	0.021±0.001	0.0082±0.0002	5±0.1	6±0.1
spartan_30	graphite	y	0.022±0.001	0.0085±0.0002	5±0.1	5.6±0.1

Table 5.3: HT nozzle configurations: mass flow rates and throat erosion comparison; all these tests had a burning time of 13 seconds

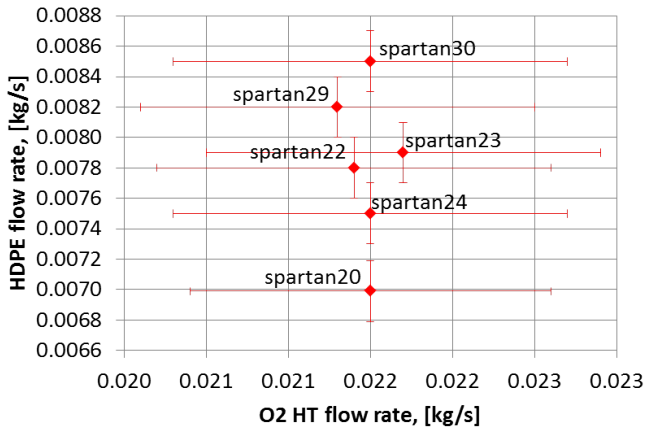

Figure 5.8: HDPE mass flow rate at different operating pressures

5.5 Phase 4: Results

5.5.1 50% Thrust Hot Tests

The third configuration of the hybrid torch, figure 5.5, has been adopted as the final one, for the whole throttling investigation. The hypothesis of making the mixing device thicker has been considered, in order to lengthen the working of HT at high efficiency; but this would probably have caused the mixer to be still present when HTPB had ignited, at 50% throttling level, thus introducing additional impurities in the GG mixture.

Figure 5.10 reports the typical pressure signal obtained by CC combustion. At 50% throttling level, the time lag before HTPB ignition is 7/8 s. Typically, the HT mixer

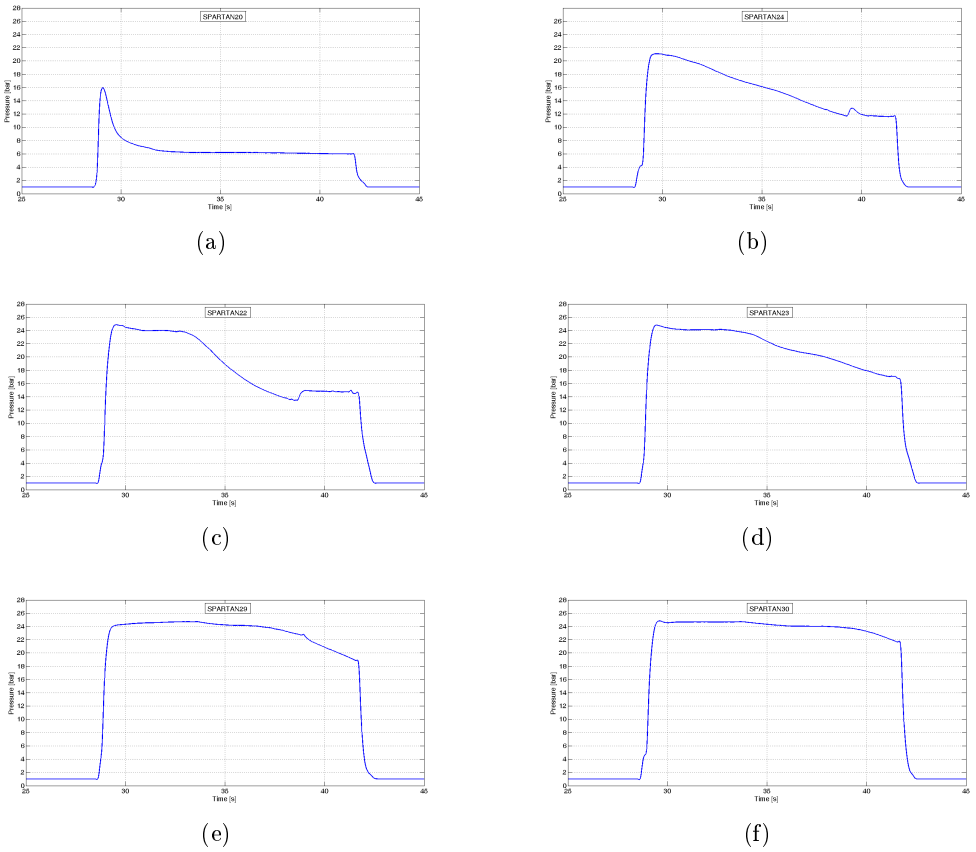

(a) (b) (c) (d) (e) (f)

Figure 5.9: 50% throttling tests: HT operating pressure comparison, as a function of nozzle and mixer behavior (see table 5.3 for details)

disappears about 2 s before, and then HT nozzle erosion begins (see figure 5.6 as an example), eventually causing the hybrid torch to work coupled with GG and CC pressure, in certain tests.

Referring to figure 5.10, red lines corresponds to 5% pressure oscillation bounds. Respect to these bounds, pressure oscillations detected are very limited, thus denoting a stable combustion. During HTPB burning, a slightly progressive burning can be observed: pressure slightly increase during time; typically a 3.5% increase has been observed respect to the initial value, after a 5.5 s burning.

No nozzle erosion has been detected for the CC nozzle (see table 5.6).

The 50% throttling tests have been the most unfavorable, in terms of HTPB ignition lag. Table 5.4 shows the burning times obtained for all the final tests performed at 50% throttling. Most of these tests have been performed for a 13 s total duration; the final test has been extended, in order to investigate a different oxidizer mean specific mass flow rate. The maximum burning time has been fixed in order to guarantee a residual grain web thickness of approximately 1 cm. It can be seen that the ignition lag is quite repeatable.

Fuel regression rate data for the same tests are reported in table 5.5 and plotted in

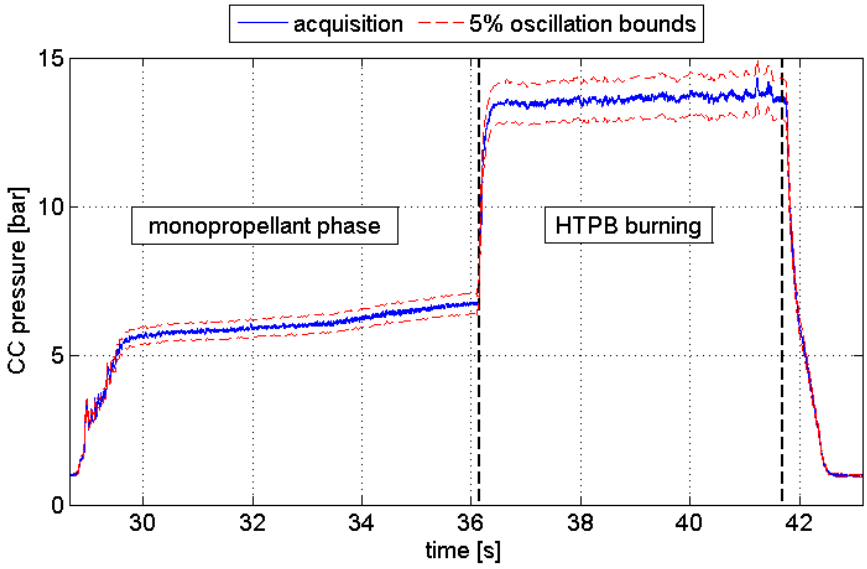

Figure 5.10: 50% throttling: typical pressure signal of the main combustion chamber

Test case	**HT burning time, [s]**	**CC ignition lag, [s]**	**CC burning time, [s]**
spartan_23	13±0.1	7.4	5.6±0.3
spartan_29	13±0.1	7.6	5.4±0.3
spartan_30	13±0.1	7.7	5.3±0.3
spartan_36	13±0.1	7.3	5.8±0.3
spartan_37	15±0.1	7.1	7.9±0.3

Table 5.4: 50% throttling: burning times and HTPB ignition delays

Test case	$\dot{m}_{ox}$ **CC, [kg/s]**	$\bar{\dot{m}}_{HTPB}$**, [kg/s]**	$\bar{O}$**F ratio**	$\bar{G}_{ox}$**, [kg/m^{2}s]**	$\bar{\dot{r}}$**, [mm/s]**
spartan_23	0.161±0.001	0.0342±0.0003	4.7±0.1	129±8	1.24±0.13
spartan_29	0.160±0.001	0.0365±0.0003	4.4±0.1	126±8	1.35±0.14
spartan_30	0.160±0.001	0.0377±0.0003	4.2±0.1	123±8	1.35±0.14
spartan_36	0.159±0.001	0.0391±0.0003	4.1±0.1	121±7	1.39±0.13
spartan_37	0.160±0.001	0.0347±0.0002	4.6±0.1	105±6	1.14±0.09

Table 5.5: 50% throttling: mass flow rates and HTPB regression rate

figure 5.11. Except for the last test listed, the mean oxidizer specific flow rate tested has been $120 \div 130\, kg/m^2 s$.

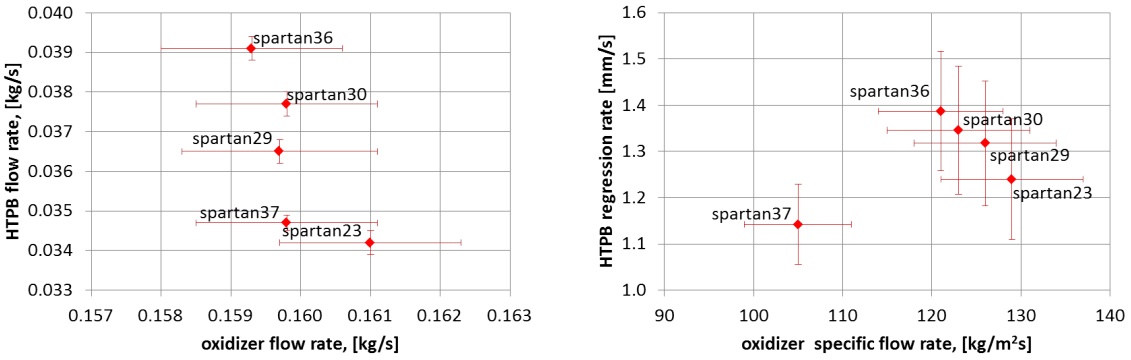

(a) (b)

Figure 5.11: 50% throttling tests: mass flow rates (a) and HTPB regression rate (b)

The experimental data have been compared with the theoretical prediction, provided by the regression rate law, eq. 3.3, with $a = 0.07$ and $n = 0.62$ [60]. The design prediction estimated a mean OF ratio equal to 4.2, and a mean regression rate equal to 1.35 mm/s for a 5.5 s burning time; the experimental evidence matches very well with this prediction. Regression rate is in any test greater than 1.1 mm/s. Such a value is certainly due the effectiveness of vortex injection in increasing the motor performance (i.e. the regression rate); in fact, the same motor tested with 90%HP-HTPB and axial injection would have produced a mean regression rate halved for the same burning duration (classical hybrid correlation: $0.04G_{ox}^{0}.56$, see ref. [21]).

Vortex injection confirmed also its usefulness in enhancing the combustion efficiency, as can be seen from table 5.6. Combustion efficiency is always greater than 93%.

Test case	**Mean post-cc pressure [bar]**	$\phi_{th,cc}$, **[mm] before test**	$\phi_{th,cc}$, **[mm] after test**	c^* **efficiency, [%]**
spartan_23	13.6±0.4	16.3±0.05	16.3±0.05	93.8±3.0
spartan_29	13.8±0.5	16.3±0.05	16.3±0.05	95.2±3.7
spartan_30	13.7±0.4	16.3±0.05	16.3±0.05	94.7±2.9
spartan_36	16.2±0.5	15±0.05	15±0.05	94.3±3.2
spartan_37	16.5±0.5	15±0.05	15±0.05	96.8±3.2

Table 5.6: 50% throttling: performances

Table 5.6 reports also the dimension of the CC nozzle throat diameter, before and after each test, to highlight any possible erosion. As previously said, at this throttling level, no damage has been observed in the nozzle, nor in the 5.5 s burns neither in the 7.9 s one. "spartan_36" and "spartan_37" have been performed with a different nozzle throat diameter, to evaluate any possible dependency of the motor performance from the operative

pressure. No relevant effects have been detected.

5.5.2 75% Thrust Hot Tests

As expected, at 75% throttling level, the time lag before HTPB ignition shortens: a typical value of 3/4 seconds have been observed. This is due to the increase of the heat flux toward the fuel grain surface, caused by the increase of the oxidizer mass flow rate.

Even the mixer consumption is faster: its effect lasts for about 2 s since the HT is ignited. So the mixer has already disappeared when HTPB ignites. Figure 5.12 reports the typical signals obtained for HT, GG, and CC at this throttling level.

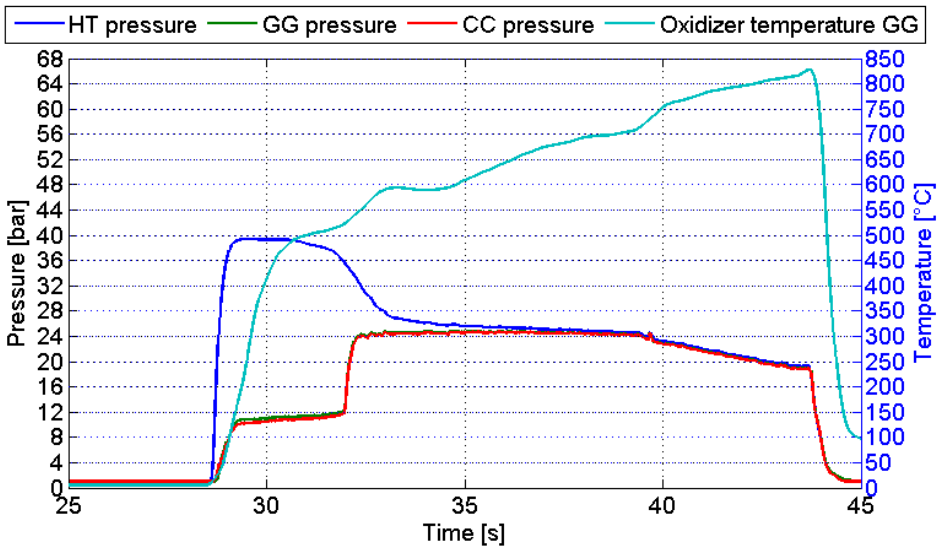

Figure 5.12: 75% throttling: HT, GG, and CC chamber pressure behavior; ignition takes place 3.5 s after HT ignition

Considering the pressure signal of the main combustion chamber, reported in figure 5.13, a stable signal is observed. In the last four seconds of burning, CC nozzle erosion can be detected by the sudden change in pressure trend.

Table 5.7 summarizes the typical burning time obtained at this throttling level. Even at this throttling level, a longer test has been performed finally.
The observed ignition delay in these cases is 3/4 seconds, respect to the 7/8 seconds proper of the 50% throttling level. The total burning time has been kept unchanged: thus for a 13 seconds burning of the hybrid torch, the CC burning has lasted for 9 seconds (except the last, longer, case).

The resulting fuel consumption data are reported in table 5.8 and then plotted in figure 5.14. On the other hand, combustion performances are reported in table 5.9.

A CC burning time of 9/10 s have determined mean oxidizer specific flow rate in the range $130 \div 140\, kg/m^2 s$.

The mean regression rate, resulting from a 9 seconds long burn, is higher than 1.4 mm/s. Even in this case, there is a good agreement between the experimental results

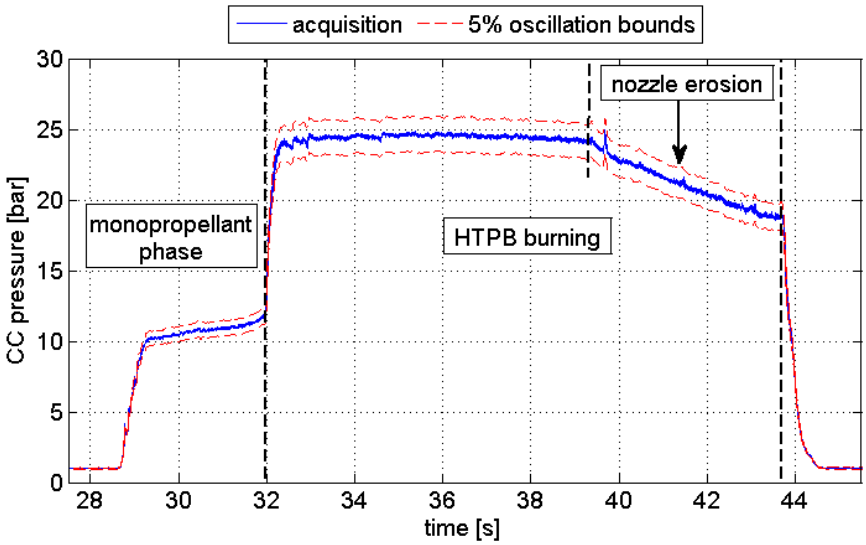

Figure 5.13: 75% throttling: typical pressure signal of the main combustion chamber

Test case	**HT burning time, [s]**	**CC ignition lag, [s]**	**CC burning time, [s]**
spartan_26	13±0.1	3.9	9.1±0.3
spartan_27	13±0.1	3.8	9.2±0.3
spartan_28	13±0.1	3.3	9.7±0.3
spartan_38	15±0.1	3.2	11.8±0.3

Table 5.7: 75% throttling: burning times and HTPB ignition delays

Test case	$\dot{m}_{ox}$ **CC, [kg/s]**	$\bar{\dot{m}}_{HTPB}$**, [kg/s]**	$\bar{OF}$ **ratio**	$\bar{G}_{ox}$**, [kg/m^{2}s]**	$\bar{\dot{r}}$**, [mm/s]**
spartan_26	0.243±0.002	0.0486±0.0004	5.0±0.1	136±7	1.58±0.08
spartan_27	0.242±0.002	0.0473±0.0004	5.1±0.1	140±7	1.46±0.08
spartan_28	0.242±0.002	0.0455±0.0004	5.3±0.1	137±7	1.39±0.07
spartan_38	0.237±0.005	0.0421±0.0003	5.6±0.1	123±6	1.24±0.06

Table 5.8: 75% throttling: mass flow rates and HTPB regression rate

and the theoretical prediction; the latter gives a mean OF ratio equal to 5.2 and a mean regression rate equal to 1.48 mm/s, in correspondence of a 9 s burn. If a CC burning time equal to the 50% level one had been considered, a mean regression rate equal to 1.66 mm/s would have been achieved, in correspondence of a mean specific oxidizer flow rate of 167 kg/m^2s.

Combustion efficiency is greater than 95%. The experimental characteristic velocity

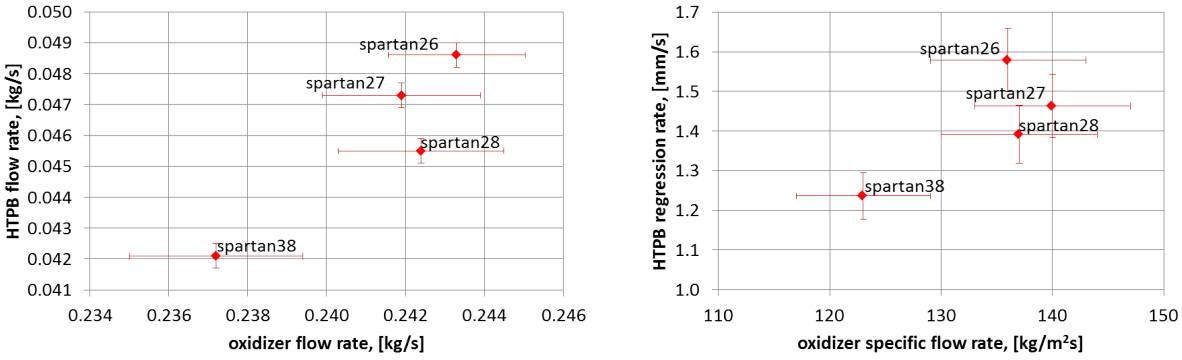

(a) (b)

Figure 5.14: 75% throttling tests: mass flow rates (a) and HTPB regression rate (b)

Test case	**Mean post-cc pressure [bar]**	$\phi_{th,cc}$, **[mm] before test**	$\phi_{th,cc}$, **[mm] after test**	c^* **efficiency, [%]**
spartan_ 26	18.6±0.5	17.3±0.05	18.0±0.05	95.5±2.8
spartan_ 27	16.7±0.5	18.0±0.05	19.0±0.05	95.8±3.1
spartan_ 28	21.2±0.5	16.3±0.05	16.5±0.05	97.5±2.6
spartan_ 38	24.4±0.6	15±0.05	17.2±0.05	97.6±3.0

Table 5.9: 75% throttling: performances

has been calculated excluding the nozzle throat erosion phase from the calculation of the mean operating pressure. This choice implicitly assumes that the combustion efficiency does not depend on the operating pressure.

As far as the nozzle throat erosion is concerned, a sort of aging has been observed: nozzles used several times tend to erode more easily, and this denotes a deterioration of graphite corrosion resistance. In fact, comparing test "spartan_28" with the previous two, a negligible nozzle erosion has been observed in this case, since the graphite insert of the CC nozzle had already been substituted. From test "spartan_38" a nozzle throat erosion of 0.27±0.03 mm/s has been estimated.

5.5.3 Full Thrust Hot Tests

Finally, at 100% throttling level, the time lag before HTPB ignition further reduces: a typical value of 2.5/3.5 seconds have been observed.

It has to be said that the "spartan_33" has to be considered a spurious test: in fact, in this case the water mass flow rate injected into the gas generator has been a 15% higher respect to "spartan_31" and "spartan_34". This difference has caused the mixture composition to be slightly different, and this can justify both the different HTPB ignition

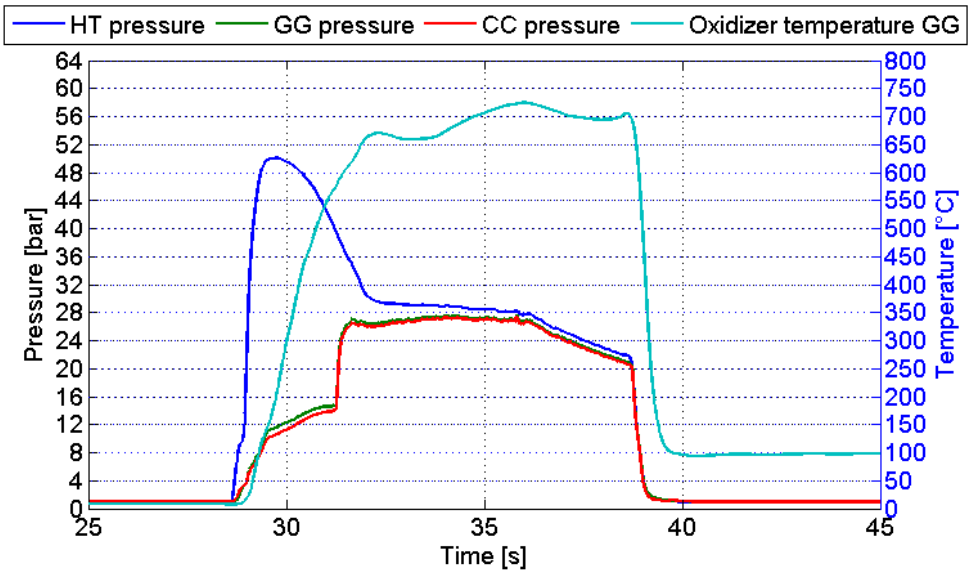

Figure 5.15: 100% throttling: HT, GG, and CC chamber pressure behavior; ignition takes place 2.5 s after HT ignition

lag and final performances.

At full thrust, the HT mixer consumption is almost immediate. Its effect can be barely recognized in the HT pressure signal, reported in figure 5.15.

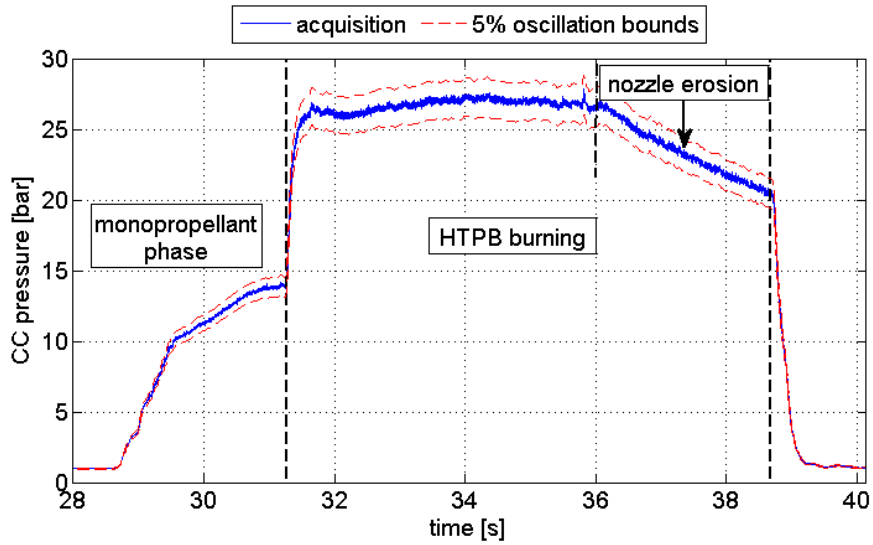

Figure 5.16: 100% throttling: typical pressure signal of the main combustion chamber

CC combustion keeps being stable, as can be seen in figure 5.16. In the last three

seconds of burning, CC nozzle erosion can be detected by the sudden change in pressure trend.

Table 5.10 summarizes the typical burning time obtained at this throttling level. A longer burning time test has not been performed at this level, basically in order to avoid heavier nozzle erosion.
The observed ignition delay in these cases is 2.5/3.5 seconds, respect to the 3/4 seconds proper of the 75% throttling level. The total burning time has been shortened, in order to limit the nozzle throat erosion effect and preserve 1 cm of grain web thickness, at least: thus for a 10 seconds burning of the hybrid torch, the CC burning has lasted for 7 seconds.

The resulting fuel consumption data are reported in table 5.11 and then plotted in figure 5.17. On the other hand, combustion performances are reported in table 5.12.

A CC burning time of 6.5/7.5 s have determined mean oxidizer specific flow rate in the range $175 \div 190\, kg/m^2 s$. "spartan_33" has been performed with a HTPB grain, whose initial port diameter was 39.5 mm, and this explains the mean value of its specific oxidizer flow rate.

Considering "spartan_31" and "spartan_34", the mean regression rate, resulting from a 7 seconds long burn, is higher than 1.6 mm/s. Even in this case, the experimental evidence is in good agreement with the theoretical prediction.

Combustion efficiency is greater than 97%. As for the 75% throttling, the experimental characteristic velocity has been calculated excluding the nozzle throat erosion phase from the calculation of the mean operating pressure.

"spartan_33" has been characterized by a minor fuel mass flow rate and a lower combustion efficiency, and this has been attributed to the difference in mixture composition, caused by a different setting of the water mass flow rate. For this reason, this test has not been considered in the final comparison between the different throttling levels.

Test case	**HT burning time, [s]**	**CC ignition lag, [s]**	**CC burning time, [s]**
spartan_31	10±0.1	2.6	7.4±0.3
spartan_33	10±0.1	3.5	6.5±0.3
spartan_34	10±0.1	2.9	7.1±0.3

Table 5.10: 100% throttling: burning times and HTPB ignition delays

Test case	$\dot{m}_{ox}$ **CC, [kg/s]**	$\bar{\dot{m}}_{HTPB}$**, [kg/s]**	$\bar{O}$**F ratio**	$\bar{G}_{ox}$**, [kg/m^{2}s]**	$\bar{\dot{r}}$**, [mm/s]**
spartan_31	0.308±0.003	0.0516±0.0005	6±0.1	185±10	1.63±0.10
spartan_33	0.327±0.003	0.0476±0.0005	6.9±0.1	175±9	1.42±0.11
spartan_34	0.312±0.003	0.0526±0.0005	5.9±0.1	190±10	1.67±0.11

Table 5.11: 100% throttling: mass flow rates and HTPB regression rate

As expected, CC nozzle throat erosion is much stronger; at 75% throttling level, it

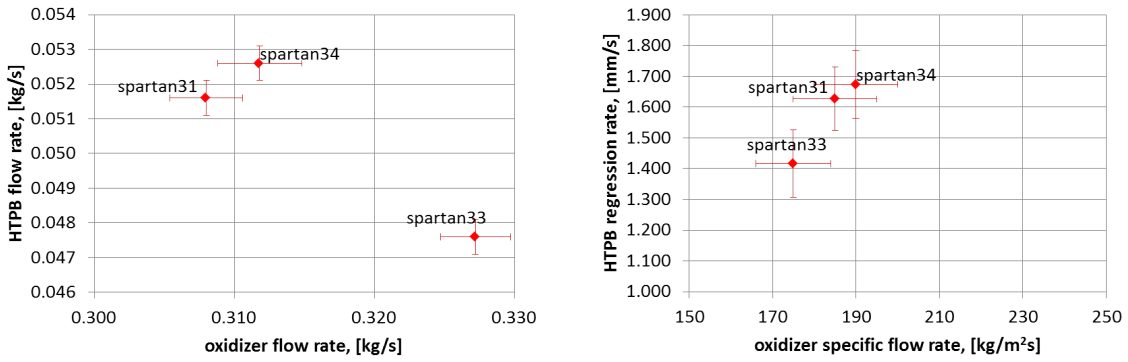

(a) (b)

Figure 5.17: 100% throttling tests: mass flow rates (a) and HTPB regression rate (b)

Test case	**Mean post-cc pressure [bar]**	$\phi_{th,cc}$, **[mm] before test**	$\phi_{th,cc}$, **[mm] after test**	c^* **efficiency, [%]**
spartan_31	26.7±1.2	16.3±0.05	19±0.05	97.5±4.5
spartan_33	19.5±0.5	19.0±0.05	21±0.05	93.1±2.1
spartan_34	28.6±1.0	16.0±0.05	19±0.05	98.2±3.9

Table 5.12: 100% throttling: performances

takes approximately 7.5 s for the nozzle to start eroding; this is the time required to the nozzle to increase its temperature up to a value where chemical attack is favored. At 100 % throttling, having the same throat diameter and assuming the combustion products temperature to be almost unchanged, the thermal flux at the nozzle throat is higher, as the total mass flow rate is higher; erosion becomes evident approximately 4 s after HTPB ignition. Referring to "spartan_31", for example, a nozzle throat erosion of 0.40±0.04 mm/s has been estimated, a 50% higher than the 75% throttling value.

5.5.4 General Comparison

Finally, a general comparison has been performed, between the different throttling levels.

First of all, HTPB ignition takes place always when the thermocouple inside GG reads 550 °C. This value is compatible with the indication provided by Nammo Raufoss AS, which foresaw a temperature of 490 °C [60].

As can be verified in tables 5.6, 5.9 and 5.12, combustion efficiency is in any case higher than 93%, thus suggesting the effectiveness of vortex injection as a valuable solution for high performing hybrids.

A slight dependence of combustion efficiency from operative OF ratio and total mass flow rate has been observed.

Figure 5.18 compares the experimental characteristic exhaust velocity, c_r^*, with the ideal one, c_t^*, as a function of the OF ratio. The optimal OF ratio for 88%H2O2-HTPB has been calculated by the thermochemical software, in frozen equilibrium conditions: ideal characteristic exhaust velocity, c_t^*, is maximized for OF equal to 6.4. The closer is the OF ratio to this value, the less evident is the difference in the resulting ideal c_t^*: thus the curve OF-c_t^* is very flattened, in proximity of the optimum OF. The highest real characteristic exhaust velocities, c_r^*, have been detected in correspondence of the closest OF ratios to the optimum: thus the maximum efficiency corresponds to the 100% throttling level, whose operative OF ratio is the closest to 6.4 (i.e. 5.9/6). Figure 5.19 reports the combustion efficiency, plotted as a function of OF ratio ((a)) and oxidizer mass flow rate ((b)). An almost linear increase of the efficiency can be noted as the OF gradually increases, and thus the oxidizer flow rate.

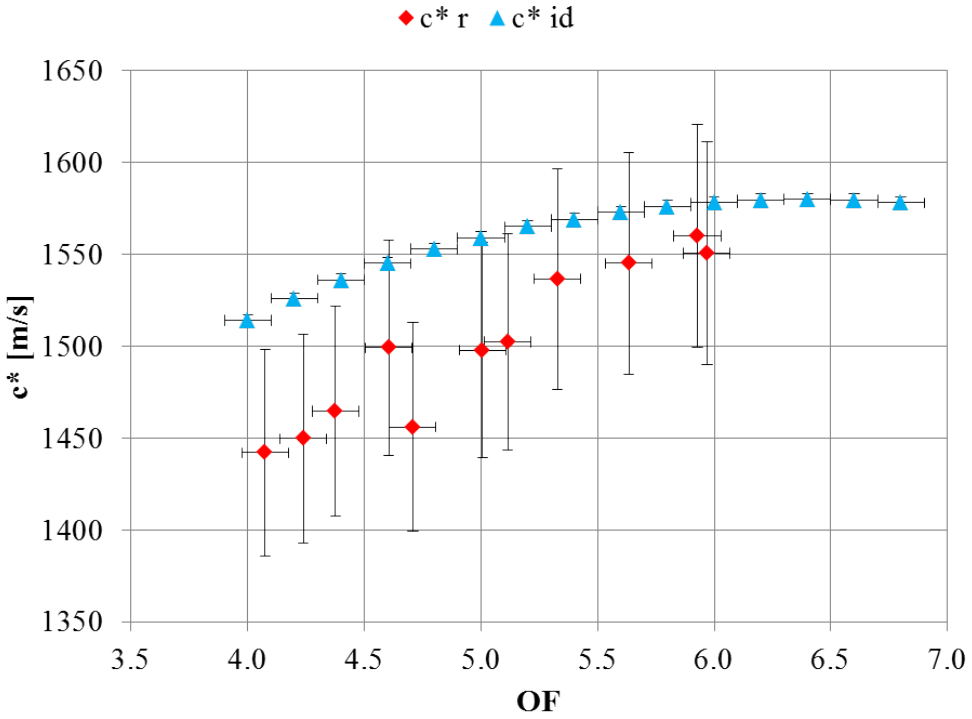

Figure 5.18: Theoretical versus ideal c^*, as a function of OF ratio

The oxidizer mixture composition has been evaluated according to the method described in section 4.3.5:

1. ideal composition, in hypothesis of perfect chemical equilibrium, and adiabatic outward process;

2. not-ideal composition, but adiabatic outward process.

The effect of a not-adiabatic process has been considered also, but resulting in negligible differences. For further details the reader is referred to section 4.3.5.

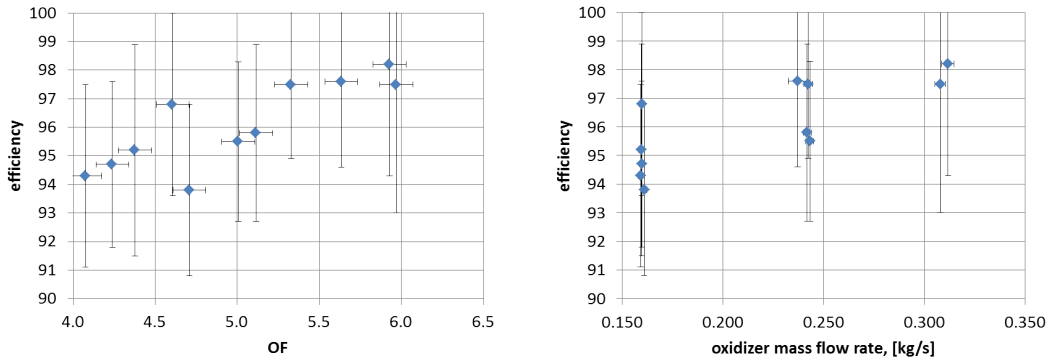

(a) (b)

Figure 5.19: Combustion efficiency as a function of: OF ratio (a) and oxidizer mass flow rate (b) for all the tests performed

Table 5.13 and 5.14 report respectively the chemical equilibrium mixture composition and the chemical no-equilibrium mixture composition, while figure 5.20 plots all these data together. It is opinion of the author that these two composition can be considered as a lower and upper bound, and the actual mixture composition is expected to lie besides these two extreme conditions.

Table 5.13: GG mixture composition in hypothesis of chemical equilibrium

Test	**Throttling level**	**Mass fractions, equilibrium**		
		CO2, eq.	**H2O, eq.**	**O2, eq.**
spartan_ 23	50%	0.15	0.45	0.40
spartan_ 29	50%	0.16	0.45	0.39
spartan_ 30	50%	0.17	0.45	0.38
spartan_ 36	50%	0.16	0.44	0.40
spartan_ 37	50%	0.16	0.44	0.40
spartan_ 26	75%	0.17	0.45	0.39
spartan_ 27	75%	0.16	0.45	0.39
spartan_ 28	75%	0.17	0.45	0.39
spartan_ 38	75%	0.17	0.45	0.39
spartan_ 31	100%	0.15	0.43	0.42
spartan_ 34	100%	0.15	0.42	0.42

Finally table 5.15 compares the O2 mass fraction, resulting from the two mixture compositions evaluated, with the reference O2 mass fraction, correspondent to 87.5%H2O2 in dissociated condition.

As a last step, the experimental regression rate obtained for HTPB at different specific mass flow rates has been compared with the reference curve $a\,G_{ox}^{n}$, constructed with $a = 0.07$ and $n = 0.62$ [60]. Figure 5.21 shows this comparison. A good correspondence can be

Table 5.14: GG mixture composition in hypothesis of chemical no-equilibrium

Test	Throttling level	Mass fractions no-equilibrium			
		CO2, n.eq.	**H2O, n.eq.**	**O2, n.eq.**	**C2H4, n.eq.**
spartan_23	50%	0.10	0.42	0.46	0.01
spartan_29	50%	0.11	0.43	0.45	0.02
spartan_30	50%	0.11	0.43	0.44	0.02
spartan_36	50%	0.11	0.42	0.45	0.02
spartan_37	50%	0.11	0.42	0.46	0.02
spartan_26	75%	0.12	0.43	0.44	0.01
spartan_27	75%	0.12	0.43	0.44	0.01
spartan_28	75%	0.12	0.43	0.43	0.02
spartan_38	75%	0.12	0.43	0.44	0.01
spartan_31	100%	0.11	0.42	0.46	0.01
spartan_34	100%	0.12	0.41	0.46	0.01

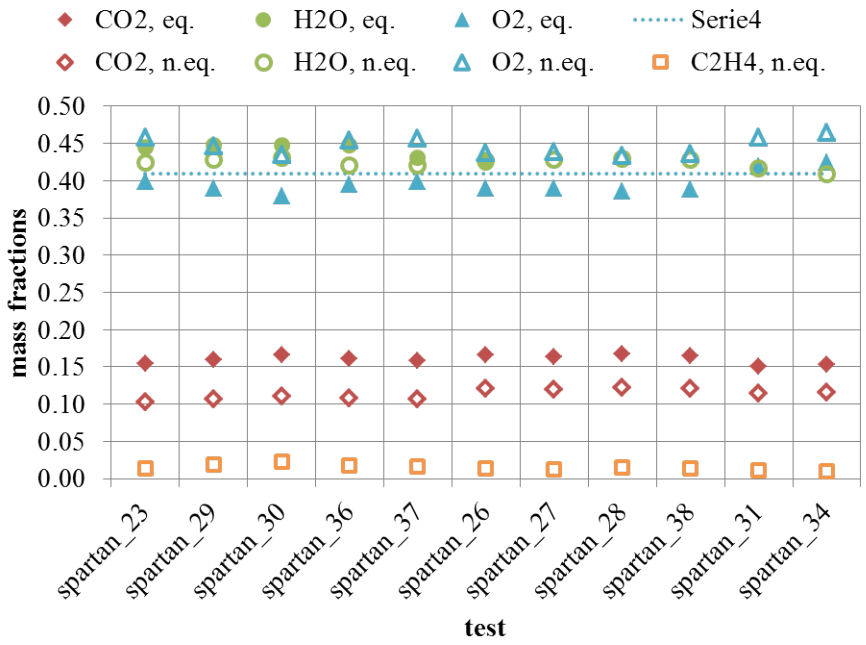

Figure 5.20: Ideal (*eq.*) versus not-ideal (*n.eq.*) GG mixture composition

noticed. The best fit in terms of R^2 has also been calculated; it provides a slight correction of the a coefficient, that is $a = 0.065$, which is a 7% lower than the reference value. In figure, both the reference curve and the "corrected" curve.

Thus it can be concluded that the solution adopted to simulate the combustion behavior of 87.5%H2O2-HTPB is representative of the real case.

Table 5.15: O2 mass fraction: comparison between the actual values estimated for the equilibrium and no-equilibrium mixture composition, respect to the reference value, *O2 mf, ref*, correspondent to dissociated 87.5%H2O2

Test	Throttling level	O2 mf, ref	Error, equilibrium	Error, no-equilibrium
spartan_23	50%		-3%	12%
spartan_29	50%		-5%	9%
spartan_30	50%		-8%	6%
spartan_36	50%		-4%	11%
spartan_37	50%		-3%	11%
spartan_26	75%	0.41	-5%	7%
spartan_27	75%		-5%	7%
spartan_28	75%		-6%	6%
spartan_38	75%		-5%	6%
spartan_31	100%		2%	12%
spartan_34	100%		3%	13%

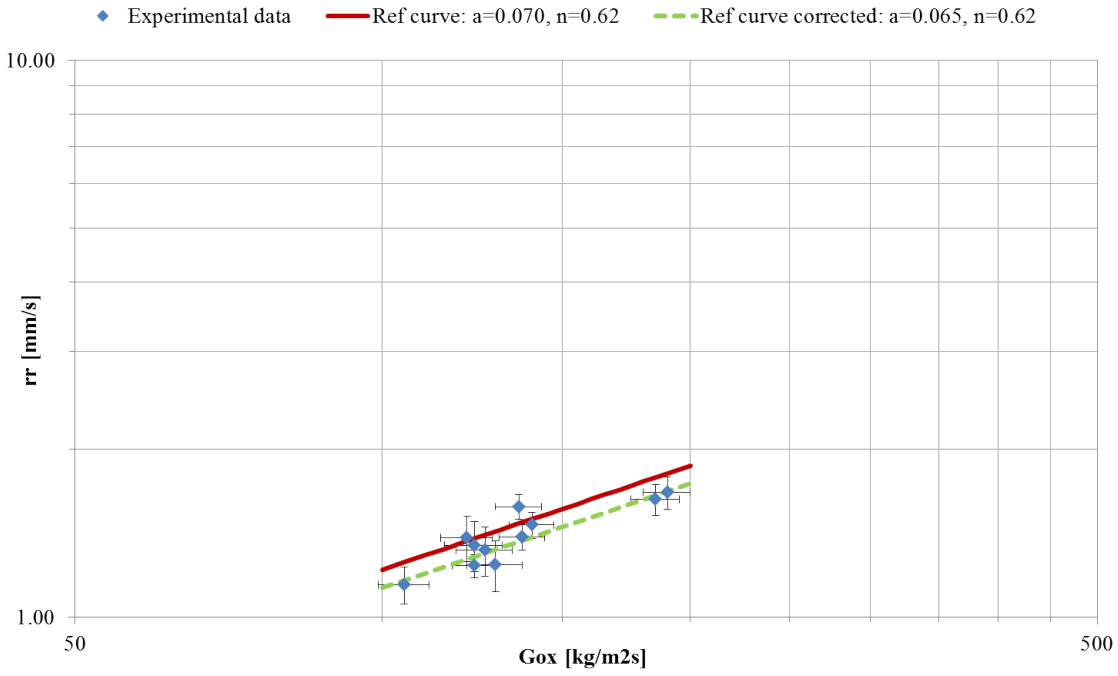

Figure 5.21: Experimental data versus reference curve comparison

5.6 Experimental Tests Summary

Table 5.16 summarizes all the experimental activities performed and just described.

System/ subsystem	**Test type**	**Objective**	**N°tests**
O_2^{GG} *feed line* O_2^{HT} *feed line*	Cold discharges at different upstream pressure levels	• Pressure regulators calibration • Sonic orifices calibration	43
H_2O^{GG} *feed line*	Cold discharges at different upstream pressure levels	• Pressurization method selection • Cavitating venturi calibration	22
HT	Hot tests at different throttling levels and configurations	• Ignition verification • O2-HDPE $\dot{r}$ evaluation • c^* efficiency estimation	16
HT & GG	Hot tests with different HT configurations	• Mixture optimization	14
HT & GG & CC	Hot tests at different throttling levels	• Ignition assessment • Performance evaluation • Throttling functioning	15

Table 5.16: Summary of the experimental activities conducted

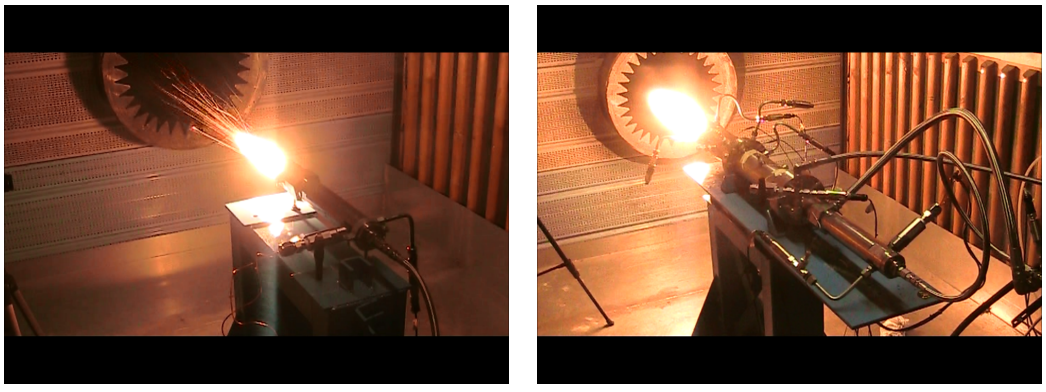

(a) (b)

Figure 5.22: Frame extrapolated from a high speed movie (420 fps) of the hybrid torch testing ((a)) and the complete engine hot test, at 50% throttling ratio

Chapter 6

Conclusions

This work has been focused on the investigation of a high performing throttleable hybrid motor, conceived for soft-landing applications.
The main purpose of the research has been to develop and characterize a motor in the 1kN-class, with characteristics like: high performance at different operative conditions, both in terms of regression rate and combustion efficiency enhancement, safety and reliability.

This research has been part of the EU FP7 SPARTAN project, aimed at developing a soft-lander demonstrator for planetary exploration; in this framework, the University of Padova has been responsible of customizing a several numerical tool (analytic and CFD models) to accurately simulate the hybrid motor functioning, thus supporting design and testing phases. A dedicated experimental setup has been designed, to perform experimental tests in order to validate the numerical results.

The preliminary design guidelines of the motor have been defined according to the requirements of the SPARTAN consortium.

The motor considered burns HTPB as fuel and 87.5%H2O2. Fuel ignition is accomplished thanks to the hot gases resulting from the oxidizer decomposition through a catalyst.

The doctoral research has been conducted combining several tools in synergy: analytic models, CFD simulations and experimental tests. The analytic models have supported the comprehension of the physical processes involved. The numerical simulations have been useful tools both to provide indications for final design purposes and to investigate in detail aspects of the internal ballistic of the motor, which were difficult to be observed in experimental tests. Finally, experimental tests have been conducted to validate the numerical prediction and assess the achievement of the desired and expected results.

As a first step a deep numerical investigation has been performed about vortex injection.

First of all, the physical characteristics of the flowfield produced by vortex injection have been investigated, considering a motor configuration already developed and tested at UPD. In this phase, CFD simulations have been combined with the forced vortex analytic model; this model describes exactly the vortex flowfield of the oxidizer, when no fuel mass addition, no chemical reactions and no isentropic acceleration are considered. As soon as these contributions are considered, the flowfield deviates quantitatively from the analytic modeling, but the same qualitative trends are respected.

Thanks to this numerical results, it has been observed that, respect to axial injection,

the vortex injection produces a strong helical flow that enhances the turbulence level in the combustion chamber, and thus the combustion efficiency; the hot products are mixed with the central cold core and this allows for fresh oxidizer to reach the flame. Moreover centrifugal forces push the flame near the wall enhancing the heat flux and thus the regression rate. This evidence has confirmed that the vortex injection can a suitable solution to enhance the combustion efficiency of hybrid motors.

In a second phase, the preliminary design of the motor produced within SPARTAN has been simulated to predict its performance and its sensitivity to some changes in the vortex configuration, the chamber internal geometry, and the operative conditions: varying the swirl number, w/out an axial injection component at the inlet, w/out pre/post combustion chambers, changing port size and the oxidizer mass flow. Thanks to these numerical results, a high combustion efficiency was expected to be observed in the experimental tests at different throttling levels.

Then experimental tests of the motor have been performed to evaluate the actual performance at different throttling levels.

In order to overcome the issues related to handle and store hydrogen peroxide in high concentration, a safe and reliable experimental test-bed has been designed, based on the adoption of a gas generator to simulate high concentration hydrogen peroxide in dissociated conditions, as it would be passing through a catalyst. The gas generator has been integrated with the hybrid motor, in order to inject the mixture produced inside the gas generator as oxidizer into the combustion chamber of the hybrid motor.

An intense preliminary experimental phase has been required to optimize the functioning of each subsystem, and in particular of the gas generator. Moreover a complete diagnostic system has been defined and installed, in order to have a full and accurate monitoring of the interesting parameters.

Finally, the hybrid motor has been tested at three different fixed throttling levels: full thrust, 75% thrust and 50% thrust.

Fuel ignition has been achieved at each throttling level, and it has been observed that the ignition delay depends on the throttling level: lower throttling levels, and thus oxidizer fluxes, denote a longer delay. After ignition, a stable combustion has been observed in all the tests.

The experiments have shown a motor with combustion efficiency above 93% at each throttling level. As expected, throttling down causes the OF ratio to shift from the design value and thus a lower efficiency is resulted in these cases.

For oxidizer fluxes between 100 and 200 kg/m2/s a regression rate between 1.1 and 1.7 mm/s has been obtained.

Nozzle throat erosion has been encountered, mainly at full thrust, but also at 75%, with a slighter entity. 50% thrust tests have not shown any erosion.

The experimental results have been compared with the reference regression rate law, proper of 87.5%H2O2-HTPB: a really satisfying correspondence have been demonstrated.

Thus this work has demonstrated the vortex injection effectiveness in enhancing the combustion efficiency of a throttleable hybrid rocket motor.

Moreover, it can be concluded that the gas generator adopted to simulate the combustion behavior of 87.5%H2O2-HTPB is an extremely safe solution, surely representative of the real case. It has been demonstrated that a versatile and flexible gas generator can be

realized without the need for liquid fuels (as hydrogen for example), and this represent an additional safety feature.

A possible future work regarding the use of this experimental test-bed, is to study the dynamic throttling response of the hybrid motor.

Appendix

Temperature Measurement Devices Survey

Thermocouples, Overview

[76] Their functioning is based on the thermoelectric effect. Two dissimilar conductors contact each other at one or more spots: a voltage is produced when the temperature of one of the spots differs from the reference temperature at other parts of the circuit. Referring to 6.1, the relevant junction is called the hot spot (H); the other ends of the two conductors (CA and CB) can be linked to other portions of conductors to extend the length of the cables or introduce compensation effects; usually these extensions are copper made and their corresponding junctions with the main conductors represent the reference (or cold) spot. If the latter is kept at a known and stable temperature, the temperature at H location can be deduced from the output voltage (see eq. 6.1):

$$e.m.f. = \epsilon \nabla T = \epsilon (T_H - T_C) \tag{6.1}$$

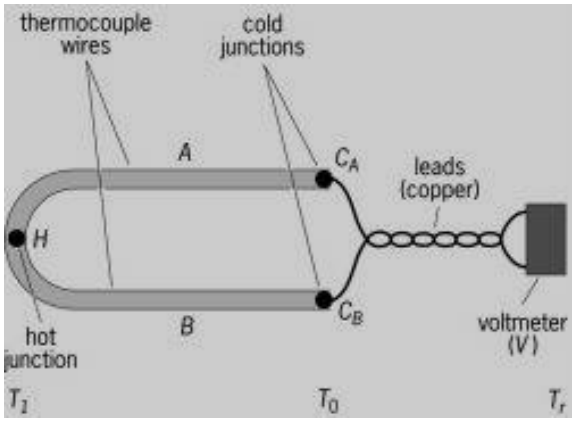

Figure 6.1: Schematization of a thermocouple

The wide use of thermocouples in industrial and scientific applications is due to the convenience of an electric output. However, the output voltage is typically not a linear function of the temperature except in a reduced operative range. For this reason the output voltage is tabulated as a function of the hot junction temperature, for each type of

thermocouple during a calibration phase. These tables refer to a reference junction kept constantly at °C thanks to an ice bath. For common industrial applications, temperature variations regarding the reference junction are measured by a thermistor, mounted as close as possible to the junction itself: an *e.m.f.* is generated, proportional to the temperature variations, in order to compensate them.

Types, Materials, Applications The choice of materials to be used as conductors in a thermocouple is driven by factors as:

- operative range;
- quality of the signal;
- linearity;
- repeatability.

Type International denomination	Conductors	Temperature Operative Range, °C (regardless of probe diameter and insulating materials)	
		Continuum Use	Short Duration
R	Pt-13% Rh(+) Pt(-)	[0,+1600]	[0,+1700]
S	Pt-10% Rh(+) Pt(-)	[0,+1500]	[0,+1700]
B	Pt-30% Rh(+) Pt-6%(-)	[+100,+1600]	[0,+1800]
K	Ni-Cr(+) Ni-Al(-)	[0,+1100]	[-180,+1300]
T	Cu(+) Cu-Ni(-)	[-185,+300]	[-250,+400]
J	Fe(+) Cu-Ni(-)	[+20,+700]	[-180,+800]
E	Ni-Cr(+) Cu-Ni(-)	[0,+800]	[-40,+900]
N	Ni-Cr-Si(+) Ni-Si(-)	[0,+1150]	[-270,+1300]

Table 6.1: Types of commonly used thermocouples and their operative ranges

Thermocouples can be divided into two main categories:

1. precious metals based (mainly platinum with platinum-rhodium alloy), which generally tends to be the most stable but the most expensive too, with a total operative range of about [0,+2000] °C; however their signal is weaker than that of other types;
2. common metals based which have a more limited operative range of about [0,+1200] °C.

Eight are the most commonly used types of thermocouples. Table 6.1 summarizes them and reports their temperature operative range; the first three types correspond to the precious metals based category while the others to the common metals based one.

Selection of the alloys combination is driven by cost, availability, convenience, melting point, chemical properties, stability, and output. Different types are best suited for different applications. They are usually selected on the basis of the temperature range and sensitivity needed. Thermocouples with low sensitivities (B, R, and S types) have correspondingly lower resolutions. Other selection criteria include the chemical inertness of the thermocouple material and whether it is magnetic or not. The maximum operative temperature indicated in table 6.1 is not an absolute limit: in real applications, it has to be commensurate with: conductors' diameters, environmental conditions, lifetime required for the thermocouple.

Figure 6.2 reports the typical curves of *e.m.f* as a function of temperature for the thermocouple types indicated in table 6.1.

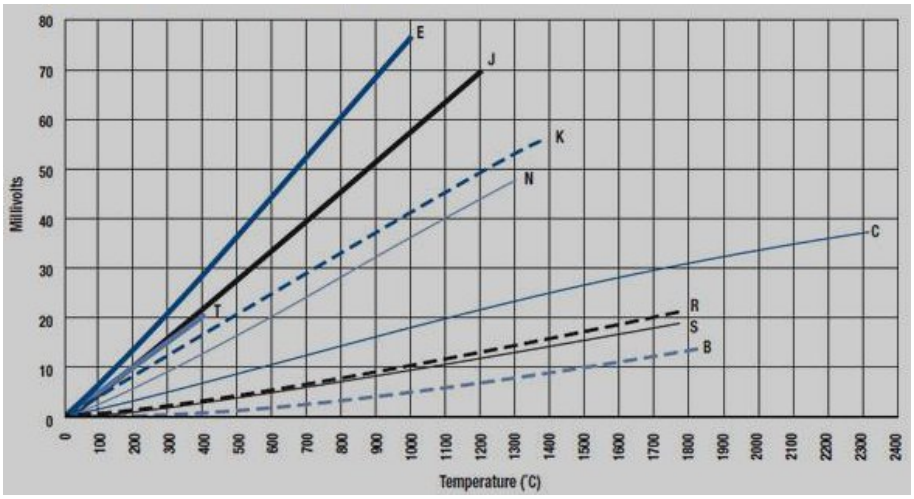

Figure 6.2: Thermocouple *e.m.f* as a function of temperature for the most used types

Types B, R, and S thermocouples use platinum or a platinum-rhodium alloy for each conductor. These are among the most stable thermocouples, but have lower sensitivity than other types, approximately 10 μV/°C. They are usually used only for high temperature measurements due to their high cost and low sensitivity.
Type K (chromel 90% nickel and 10% chromium-alumel 95% nickel, 2% manganese, 2% aluminum and 1% silicon) is the most common general purpose thermocouple with a sensitivity of approximately 41 μV/°C. It is inexpensive and a wide variety of probes are available in its temperature operative range. It can be used in oxidizing ambient but above 800 °C, the oxidation causes thermal drift and loss in calibration.
Type T is extremely repeatable in the range [-200,200] °C (±0.1 °C).
Type J has a more restricted range than type K, but higher sensitivity of about 50 μV/°C. In reducing ambient it can be safely used while in oxidizing ambient, its degradation above 550 °C is fast.
Type E has a high output (68 μV/°C). Additionally, it is non-magnetic.
Type N thermocouples main characteristics are: stability and oxidation resistance. Sensitivity is about 39μV/°C at 900 °C, slightly lower compared to type K. This type of thermocouples overcomes the three principal causes of thermoelectric instability in the

standard base-metal thermoelement materials:

1. A gradual and generally cumulative drift in thermal *e.m.f.* on long exposure at elevated temperatures. This is observed in all base-metal thermoelement materials and is mainly due to composition changes caused by oxidation, carburization, or neutron irradiation that can produce transmutation in nuclear reactor environments. In the case of type K thermocouples, manganese and aluminum atoms from the KN (negative) wire migrate to the KP (positive) wire, resulting in a down-scale drift due to chemical contamination. This effect is cumulative and irreversible.

2. A short-term cyclic change (hysteresis) in thermal *e.m.f.* on heating in the temperature range ca. [250,650] °C, which occurs in all base-metal thermoelement materials but especially in type K. This kind of *e.m.f.* instability is associated with structural changes such as magnetic short range order in the metallurgical composition.

3. A time-independent perturbation in thermal *e.m.f.* in specific temperature ranges. This is due to composition-dependent magnetic transformations that perturb the thermal *e.m.f.* in type K thermocouples in the range [25,225] °C, and in type J above 730 °C.

Nicrosil and Nisil thermocouple alloys show greatly enhanced thermoelectric stability relative to the other standard base-metal thermocouple alloys, because their compositions substantially reduces the thermoelectric instabilities described above. This is achieved primarily by increasing component solute concentrations (chromium and silicon) in a base of nickel above those required to cause a transition from internal to external modes of oxidation, and by selecting solutes (silicon and magnesium) that preferentially oxidize to form a diffusion-barrier, and hence oxidation-inhibiting films. Table 6.2 describes the main metrological characteristics of the eight types of thermocouples.

Thermocouples can also be insulated.
The most widespread kind of insulation is the mineral one (MI) with metallic sheath (MIMS). The metallic sheath contains an insulating mineral powder extremely compressed (usually manganese oxide), which protects the conductors of the thermocouple. This kind of thermocouples can stand temperatures up to about 1200 °C in chemically hostile conditions; they are well integrated, compact, hermetically isolated, self-protected but flexible, which make them easy to mount in many different applications. Moreover they are quite accurate and stable in time, with a satisfying insulating resistance. Depending on the specific application, the sheath can be made of steel, stainless steel, alloys such as Inconel.

Resistance Thermometers, Overview

[76] An electric conductor is characterized by a resistance which is function of the operative temperature; this is mainly due to electrons diffusion and vibrations of the crystal lattice. So, starting from the measurement of the resistance, it is possible to determine the temperature. The advantage of this kind of relation is its absoluteness: respect to the thermocouples, a reference junction is not required here; moreover, the instrument can be connected to the acquisition system with standard copper cables with no particular requirements or restrictions. An important requirement for a conductor to be used as a

Type	Sensitivity, with ref. junction at 0°C, [μV/°C]			Tolerances on temperature reading, [°C]			
	100 °C	500 °C	1000 °C	Parameter	1st class	2nd class	3rd class
R	8	10	11	*T range*	[0,+1100]	[0,+600]	-
				Tolerance	±1.0	±1.5	
S	7	10	11	*T range*	[+1100,+1600]	[+600,+1600]	
				Tolerance	$\pm[1+0.003(t-1100)]$	±0.0025|t|	
B	1	5	9				
K	42	43	39	*T range*	[-40,+375]	[-40,+333]	[-167,+40]
				Tolerance	±1.5	±2.5	±2.5
				T range	[+375,+1000]	[+333,+1200]	[-200,-167]
				Tolerance	±0.004|t|	±0.0075|t|	±0.015|t|
T	46	-	-	*T range*	[-40,+125]	[-40,+133]	[-67,+40]
				Tolerance	±0.5	±1.0	±1.0
				T range	[+125,+350]	[+133,+350]	[-200,-67]
				Tolerance	±0.004|t|	±0.0075|t|	±0.015|t|
J	54	56	-	*T range*	[-40,+375]	[-40,+333]	[-167,+40]
				Tolerance	±1.5	±2.5	±2.5
				T range	[+375,+750]	[+333,+900]	[-200,-167]
				Tolerance	±0.004|t|	±0.0075|t|	±0.015|t|
E	68	81	-	*T range*	[-40,+375]	[-40,+333]	[-167,+40]
				Tolerance	±1.5	±2.5	±2.5
				T range	[+375,+800]	[+333,+900]	[-200,-167]
				Tolerance	±0.004|t|	±0.0075|t|	±0.015|t|
N	30	38	38	*T range*	[-40,+375]	[-40,+333]	[-167,+40]
				Tolerance	±1.5	±2.5	±2.5
				T range	[+375,+1000]	[+333,+1200]	[-200,-167]
				Tolerance	±0.004|t|	±0.0075|t|	±0.015|t|

Table 6.2: Types of commonly used thermocouples and their operative ranges

resistance thermometer is that its physical and chemical composition is stable and well known: impurities and flaws in the crystal lattice produce changes in the resistance, which could be function of temperature. The sensor must be pure and insulated from contamination; these aspects make the manufacturing trickier. Nowadays the most commonly used material for such a sensor is platinum. The relation between resistance and temperature is described as follows:

$$\begin{cases} \frac{R_t}{R_0} = 1 + At + Bt^2 \quad for\, t > 0°C \\ \frac{R_t}{R_0} = 1 + At + Bt^2 + Ct^3(t-100) \quad for\, t < 0°C \end{cases} \tag{6.2}$$

where A, B, C are constant coefficients determined by calibration and tabulated.

Measurement of resistance requires a small current to be passed through the device under test. This causes resistive heating, causing significant loss of accuracy if manufacturers' limits are not respected, or the design does not properly consider the heat path. The effect is minimized if the thermal contact between the filament and the case and between the case and the environment are maximized. Mechanical strain on the resistance thermometer can also cause inaccuracy. Because of the low nominal resistance of RTDs, measurement accuracy can be drastically affected by lead wire resistance. For example, lead wires with a resistance of 1 Ω connected to a 100 Ω platinum RTD cause a 1% measurement error. The problem can be solved modifying the electric circuit of power supply and data acquisition.

Materials Common RTD sensing element can be made of platinum, copper or nickel. Nickel elements have a sensitivity to temperature changes but a limited temperature range because the amount of change in resistance per degree of change in temperature becomes very non-linear at temperatures over 300 °C; moreover the resistance-temperature relationship is quite complex.
Copper has a very linear resistance-temperature relationship and it is cheaper, however copper oxidizes at moderate temperatures and cannot be used over 150 °C.
Platinum is the best metal for RTDs. Platinum is a noble metal and has the most stable resistance-temperature relationship over the largest temperature range; this relation is simple and well known. Moreover its resistivity is 6 times that of copper, a high purity can be achieved and it can be wrought in a very reproducible manner. On the other hand it can be contaminated with other materials, especially if heated up, so the materials for the mounting strip and the casing must be selected carefully. The unique properties of platinum make it the material of choice for temperature standards over the range of [-272.5,961.78] °C. The advantages of platinum resistance thermometers include:

- high accuracy;
- low drift;
- wide operating range;
- suitability for precision applications.

RTDs in industrial applications are rarely used above 660 °C. At temperatures above 660 °C it becomes increasingly difficult to prevent the platinum from becoming contaminated by impurities from the metal sheath of the thermometer. This is why laboratory standard thermometers replace the metal sheath with a glass construction. At very low temperatures, say below -270 °C, because there are very few phonons, the resistance of an RTD is mainly determined by impurities and boundary scattering and thus basically independent of temperature. As a result, the sensitivity of the RTD is essentially zero and therefore not useful.

Thermocouples versus Resistance Thermometers Comparison

Several factors influence the choice of the sensor to be used for a specific application:

- Temperature operative range;
- Maximum temperature expected; Response time;
- Accuracy;
- Stability;
- Mechanical resistance;
- Sensitivity;
- Lifetime desired;

- Chemical and physical properties of the environment to be measured;
- Cost.

Table 6.3 sums up qualitatively the main differences between thermocouples and resistance thermometers performances. These reported are general guidelines that can be modified in specific cases.

Thermocouple	**Parameter**	**Resistance thermometer**
-	Accuracy	+
[-200,+2000] °C	Temperature range	[-200,+650] °C
-	Cost	+
On top of sensor	Sensitivity	Along the stem
+	Response speed	-
Possible miniaturization	Dimensions	
Needed	Reference temperature	Not needed
Suitable	Surface temperature measurement	Not suitable
More tolerated	Vibrations	Less tolerated
Not needed	Power supply	Needed
Not present	Self-heating	Present
Less satisfying	Stability in time	More satisfying
+	Robustness	-
Same material as the conductor	Cables	Standard copper

Table 6.3: Thermocouples versus resistance thermometers

The lifetime of a thermocouple with standard metals can hardly be estimated; it depends on:

- Operating temperature;
- Probe diameter;
- Working cycles.

As a rough estimation, it is better to re-calibrate a thermocouple after 6 months/1 year. The main problem associated with these factors is the oxidation. Some practical rules to be taken into account are:

- Each 50 °C increase in operative temperature over the 500 °C halves thermocouple lifetime;
- Doubling the probe diameter, thermocouple lifetime is doubled or tripled;
- Cyclic variations of operating temperature, especially in the range [20,500] °C halves sensor lifetime respect to the same sensor operating at constant temperature.

The choice of the insulation type and the thermocouple is critical to avoid corrosion problems, whatever would be the operative environment.

Sensor Mounting Rules Three rules must be followed:

1. The heat transfer has to be maximized; in case of fluids, this means installing the probe where the flow is maximum and possibly normal to the flow direction;

2. Heat transfer from and to the sensor along the mounting support and the lead wires has to be minimized: this means immersing the sensor deeply into the fluid and adopting recesses of supports with high thermal resistance in the axial direction (for example, thin stainless steel);

3. Insertion effects can be produced to the environment by the presence of the sensor, especially in surface temperature measurements.

Response Time The control parameter when considering a temperature sensor's response time is its actual thermal diffusivity, $D = k/(c\rho)$, where k is the thermal conductivity, c is the specific heat capacity and ρ is the density. This expression basically represents the propagation speed of a temperature change inside a medium. The ideal sensor in terms of readiness has to be composed by a material with high thermal conductivity, low specific heat capacity and low density. Manufacturing constraints limit the achievable performances. However there are some tricks to increase the performances:

- To limit as much as possible the thermal resistance between the probe and the environment to be measured;

- To reduce as much as possible the length of the sensor (and so the mass which the heat is dissipated through;

- To adopt the smallest probe, compatibly with the other constraints (i.e. operative temperature, chemical composition of the environment to be measured and so on).

Thermocouple Theoretical Model

The simplest and most commonly used model to describe the dynamic behavior of a thermocouple is that of a first-order instrument. It can be deduced starting from a thermal balance between the absorbed heat from the mixture q_g and the wasted heat outwards q_o; considering a positive step function input, imposed to the thermocouples by a hot gases flux:

$$m_t c_t \frac{dT_t}{dt} = \underbrace{\frac{T_g - T_t}{R_i}}_{q_g} + \underbrace{\frac{T_o - T_t}{R_o}}_{q_o} \tag{6.3}$$

where the subscript t refers to the thermocouple, g to the gaseous mixture, i to the gas generator ambient and o to the unperturbed ambient outside the gas generator; thus R_i and R_o represents respectively the thermal resistance between thermocouple and hot mixture and thermal resistance between thermocouple and outside ambient.
The thermal dissipation outward could be considered as a combination between conduction through the house fittings of the thermocouple, conduction through the thermocouple itself

and convection towards the unperturbed air outside the gas generator; thus R_e could be seen as an equivalent resistance.

Neglecting any insertion effect locally produced by the thermocouple on the mixture (and thus $T_{meas} = T_g$), assuming a constant temperature both for the mixture (i.e. hypothesis of a step input) and the outside ambient, eq. 6.3 can be rewritten as:

$$\underbrace{m_t c_t R_i}_{\tau_1} \frac{dT'_t}{dt} + T'_t \underbrace{\frac{R_i + R_o}{R_o}}_{1/K} = 1 \tag{6.4}$$

where $T'_t = \frac{T_t - T_o}{T_g - T_o}$ is a dimensionless quantity.

Finally it results:

$$K\tau_1 \frac{dT'_t}{dt} + T'_t = K \tag{6.5}$$

which is the typical dynamic equation for a first order instrument with a static gain K and a response time $\tau = K\tau_1$.

The steady response of the instrument is [68]:

$$g_{os}(t)_I = K(1 - e^{-\frac{t}{\tau}}) \tag{6.6}$$

The transfer function is:

$$W(s)_I = \frac{K}{\tau s + 1} \tag{6.7}$$

If $R_c/R_o \to \infty$ then $K \to 1$, so maximizing the thermal insulation between the instrument and the environment and at the same time minimizing the resistance between the instrument and the mixture, the temperature measured by the thermocouple at steady state will be closer to the actual value of the mixture.

Considering a MIMS thermocouple, a first order model is not satisfying to correctly represent the instrument response in the first instants. A second order modeling is required to fit properly the sensor behavior along the entire response time: it can be considered as the metallic sheath introduces a loading effect in the correct measurement of the temperature. So the gases' temperature is filtered by the response of the metallic sheath.
In this case, the system is described by the following:

$$\begin{cases} m_t c_t \frac{dT_t}{dt} = \underbrace{\frac{T_s - T_t}{R_s}}_{q_s} + \underbrace{\frac{T_o - T_t}{R_o}}_{q_o} \\ m_s c_s \frac{dT_s}{dt} = \underbrace{\frac{T_t - T_s}{R_s}}_{q_s} + \underbrace{\frac{T_g - T_s}{R_i}}_{q_i} \end{cases} \tag{6.8}$$

where the subscript s is referred to the metallic sheath of the thermocouple, and thus q_s expresses the thermal flux between the metallic sheath and the sensing element located inside.

Deriving T_s from the first equation in 6.8 and substituting it into the second equation in 6.8, after some passages, it gets to the following:

$$\underbrace{\overbrace{m_s c_s R_s m_t c_t R_i}^{\tau_1\tau_2}}_{a_2}\frac{d^2T_t}{dt^2}+\underbrace{\left(\overbrace{R_i m_t c_t}^{\tau_1\frac{R_i}{R_s}}+\overbrace{R_s m_t c_t}^{\tau_1}+\overbrace{R_i m_s c_s}^{\tau_2}+\overbrace{R_s m_s c_s\frac{R_i}{R_o}}^{\tau_2\frac{R_s}{R_o}}\right)}_{a_1}\frac{dT_t}{dt}+ \\ +\underbrace{\overbrace{\left(\frac{R_i+R_s+R_o}{R_o}\right)}^{\frac{1}{K}}}_{a_0}T_t=\left(\frac{R_i+R_s}{R_o}\right)T_o+T_g \tag{6.9}$$

Subtracting the quantity $a_0 T_o$ from both side of the equation and dividing both members for $(T_g - To)$, equation 6.9 becomes:

$$\underbrace{K\tau_1\tau_2}_{\tau_3\tau_4}\frac{d^2T_t^*}{dt^2}+\underbrace{K\left(\tau_1+\tau_2+\tau_1\frac{R_i}{R_s}+\tau_2\frac{R_s}{R_e}\right)}_{\tau_3+\tau_4}\frac{dT_t^*}{dt}+T_t^*=K \tag{6.10}$$

where $T_t^*=\frac{T_t-T_o}{T_g-T_o}$ is a dimensionless quantity.

On stationary regime $\left(\frac{d^2T_t^*}{dt^2}=\frac{dT_t^*}{dt}=0\right)$, $T_t^*\to K$; a thermal gradient settles between the actual mixture temperature and the read one by the thermocouple, due both to thermal dispersion outwards and to the insertion effect produced by the metallic sheath.

The smallest is the value of R_s, the closest is the instrument behavior to the first order model described previously.

The steady response of the instrument in this case results [68]:

$$g_{os}(t)_{II}=K\left[1+\frac{1}{\tau_3-\tau_4}\left(\tau_4 e^{-\frac{t}{\tau_4}}-\tau_3 e^{-\frac{t}{\tau_3}}\right)\right] \tag{6.11}$$

The transfer function is:

$$W(s)_{II}=\frac{K}{(\tau_3 s+1)(\tau_4 s+1)} \tag{6.12}$$

Bibliography

[1] Sutton, G. P., Biblarz, O.: *Rocket Propulsion Elements*, 7th edition, John Wiley and Sons, New York.

[2] Barato, F.,: *Numerical and Experimental Investigation of Hybrid Rocket Motors Transient Behavior*, PhD dissertation, Padova University, Center of Studies and Activities for Space (CISAS), Padova, Italy, 2013.

[3] Chiaverini, M. J.:*Review of Solid-Fuel Regression Rate Behavior in Classical and Nonclassical Hybrid Rocket Motors*, edited by M. J. Chiaverini, and K. K. Kuo, Vol. 218, Progress in Astronautics and Aeronautics, AIAA, Reston, VA, 2007.

[4] Parissenti G., et al.: *Throttleable Hybrid Engine for Planetary Soft Landing*, 4th European Conference for Aerospace Science (EUCASS), St. Petersburg, Russia, July 2011.

[5] Ronningen, J. E., Husdal, J.: *Test Results from Small-Scale Hybrid Rocket Testing*, AAAF-ESA-CNES Space Propulsion 2012, 7-10 May 2012, Bordeaux, France.

[6] Ronningen, J. E., Husdal, J., Berger, M., Vesteras, R., Raudsandmoen, G.: *Nammo Hybrid Rocket Propulsion TRL Improvement Program*, 48th AIAA/ASME/SAE/ASEE Joint Propulsion Conference and Exhibit, 29 July-01 August 2012, Atlanta, Georgia.

[7] Bellomo, N., Barato, F., Faenza, M., Lazzarin, M., Bettella, A. and Pavarin, D.: *Numerical and Experimental Investigation on Vortex Injection in Hybrid Rocket Motors*, 47th AIAA/ASME/SAE/ASEE Joint Propulsion Conference and Exhibit, AIAA-2011-5675, 31 July-03 August 2011, San Diego, California, USA.

[8] Bellomo, N., Barato, F., Faenza, M., Bettella, A., Pavarin, D., Selmo, A.: *The "Vortex Reloaded" Project: Experimental Investigation on Fully Tangential Vortex Injection in N2O-Paraffin Hybrid Motors*, 48th AIAA/ASME/SAE/ASEE Joint Propulsion Conference and Exhibit, 29 July-01 August 2012, Atlanta, Georgia.

[9] Grosse, M.: *Effect of a Diaphragm on Performance and Regression of a Laboratory Scale Hybrid Rocket Motor Using Nitrous Oxide and Paraffin*, 45th AIAA/ASME/SAE/ASEE Joint Propulsion Conference and Exhibit, 2009, Denver, Colorado.

[10] Bettella, A., Lazzarin, M., Bellomo, N., Barato, F., Pavarin, D.: *Testing and CFD Simulation of Diaphragm Hybrid Rocket Motors*, 47th AIAA/ASME/SAE/ASEE Joint Propulsion Conference and Exhibit, 01-03 August 2011, San Diego, California.

[11] Barato, F., Faenza, M., Bellomo, N., Lazzarin, M., Bettella, A., Pavarin, D.: *Numerical Simulations of an H2O2 Vortex Hybrid Rocket Motor*, AAAF-ESA-CNES Space Propulsion 2012, 7-10 May 2012, Bordeaux, France.

[12] Bellomo, N., Barato, F., Faenza, M., Bettella, A., Pavarin, D.: *The "Vortex Reloaded" Project: Numerical Investigation on Fully Tangential Vortex Injection in N2O-Paraffin Hybrid Motors*, 48th AIAA/ASME/SAE/ASEE Joint Propulsion Conference and Exhibit, 29 July-01 August 2012, Atlanta, Georgia.

[13] Faenza, M., Englaro, A., Lazzarin, M., Bettella, A., Pavarin, D.: *Advanced CFD Investigation for Predicting Regression Rate in Hybrid Rockets*, 49th AIAA/ASME/SAE/ASEE Joint Propulsion Conference and Exhibit, 15-17 July 2013, San JosÃ©, California.

[14] Heister, S., Wernimonth, E.: *Hydrogen Peroxide, Hydroxyl Ammonium Nitrate, and Other Storable Oxidizers*, Fundamentals of Hybrid Rocket Combustion and Propulsion, Vol. 218, Progress in Astronautics and Aeronautics, 2007.

[15] Pugibet, M., Moutet, H.: *On the Use of Hydrogen Peroxide as Oxidizer in Hybrid Systems*, La Reserche Aerospatiale, No.132, 1969, pp. 15-31 (translation NASA TTF-13034, 1970).

[16] Moore, G. E., Berman, K.: *A Solid-Liquid Rocket Propellant System*, Jet Propulsion, Vol 26, No. 11, 1956.

[17] Moore, G. E., Berman, K.: *A Solid-Liquid Rocket Propellant System*, Jet Propulsion, Vol. 26, No. 11, November 1956, pp. 965-968.

[18] Moore, G. E., Cooper, F. M.: *Propellant System*, U.S. Patent 2791883, 1957.

[19] Tsohas, J., Appel, B., Rettenmaier, A., Walker, M., Heister, S.t D.: *Development and Launch of Purdue Hybrid Rocket Technology Demonstrator*, 45th AIAA/ASME/SAE/ASEE Joint Propulsion Conference and Exhibit, 2009, Denver, Colorado.

[20] Lengellè, G.:*Solid-Fuel Pyrolysis Pehnomena and Regression Rate*, Fundamentals of Hybrid Rocket Combustion and Propulsion, edited by M. J. Chiaverini, and K. K. Kuo, Vol. 218, Progress in Astronautics and Aeronautics, AIAA, Reston, VA, 2007.

[21] Cai, G., Zeng, P., Li, X., Tian, H., Yu, N.: *Scale Effect of Fuel Regression Rate in Hybrid Rocket Motor*, Aerospace Science and Technology, Vol. 24, Issue 1, Pages 141-146, Elsevier, January-February 2013.

[22] Bonifacio, S., Festa, G., Russo Sorge, A.: *Novel Structured Catalysts for Hydrogen Peroxide Decomposition in Monopropellant and Hybrid Rockets*, Journal of Propulsion and Power, Vol. 29, No. 5, September 2013.

[23] Jubb, D., Merrifield, J.: *The Development of the Hybrid Rocket for Bloodhound SSC*, press release from http://www.bloodhoundssc.com, 2012.

[24] *http://www.bloodhoundssc.com*, Bloodhound SSC Project website.

[25] Yuasa, S., Shimada, O., Imamura, T., Tamura, T., Yamamoto, K.: *A Technique for Improving the Performance of Hybrid Rocket Engines*, AIAA 99-2322, 35th AIAA/ASME/ SAE/ASEE Joint Propulsion Conference and Exhibit, Los Angeles, California, USA, 20-24 June 1999.

[26] Yuasa, S., Yamamoto, K., Hachiya, H., Kitagawa, K., Oowada, Y.: *Development of a Small Sounding Hybrid Rocket with a Swirling-Oxidizer-Type Engine*, AIAA 2001-3537, 37th Joint Propulsion Conference and Exhibit, Salt Lake City, Utah, USA, 8-11 July, 2001.

[27] Pucci, J.: *The Effects of Swirl Injector Design on Hybrid Flame-Holding Combustion Instability*, Arizona State University, 38th AIAA/ASME/SAE/ASEE Joint Propulsion Conference and Exhibit, 7-10 July 2002, Indianapolis, Indiana.

[28] Masugi, M., Ide, T., Yuasa, S., Sakurai, T., Shiraishi, N., Shimada. T.: *Visualization of Flames in Combustion Chamber of Swirling-Oxidizer-Flow-Type Hybrid Rocket Engines*, 46th AIAA/ASME/SAE/ASEE Joint Propulsion Conference and Exhibit, 25-28 July 2010, Nashville, Tennessee, USA.

[29] Myre, D. D., Canton P., Cowart J. S., Jones C. C.: *Exhaust Gas Analysis of a Vortex Oxidizer Injection Hybrid Rocket Motor*, 46th AIAA/ASME/SAE/ASEE Joint Propulsion Conference and Exhibit, 25-28 July 2010, Nashville, Tennessee, USA.

[30] Faenza, M.: *Experimental Characterization of Oxidizer Injectors for Hybrid Rockets Propulsion System*, Master thesis, University of Padova, Mechanical Engineering Department, Padova, Italy, Oct. 2010.

[31] Lee, C., Na, Y., Lee, G.: *The Enhancement of Regression Rate of Hybrid Rocket Fuel by Helical Grain Configuration and Swirl Flow.* 41st AIAA/ASME/SAE/ASEE Joint Propulsion Conference and Exhibit, 10-13 July 2005, Tucson, Arizona.

[32] Majdalani, J.: *Vortex Injection in Hybrid Rockets*, Fundamentals of Hybrid Rocket Combustion and Propulsion, edited by M. J. Chiaverini, and K. K. Kuo, Vol. 218, Progress in Astronautics and Aeronautics, AIAA, Reston, VA, 2007.

[33] Duban, P.: *The LEX rocket probe (LEX small rocket probe for in-flight testing of ONERA studies of hybrid propulsion, discussing design and program)*, L'Aeronautique et L'Astronautique, 1968, pp. 47-54.

[34] Franklin B. Mead, J., Bornhorst, B. R.: *Certification Tests of a Hybrid Propulsion System for the Sandpiper Target Missile*, AFRPL-TR- 69 -73 , 1969.

[35] Jones, R. A.: *Hybrid Propulsion System for an Advanced Rocket-Powered Target Missile*, Quarterly Technical Report, UTC 2220-QTR2, 1967.

[36] Penn, C. D., Branigan, J. E.: *Preliminary Flight Rating Tests of the HAST Propulsion System*, AFRPL-TR-15-5, 1975.

[37] *AQM-81A Firebolt*, Tactical Air Command Technical Report, Langley AFB VA, 1983.

[38] Boardman, T. A., Carpenter, R. L., Goldberg, B. E., and Shaeffer, C. W.: *Development and Testing of 11- and 24-inch Hybrid Motors under the Joint Government/Industry IR&D Program*, AIAA Paper 93-2552 , 1993.

[39] Carpenter, R. L., Boardman, T. A., Claflin, S. E., Harwell, R. J.: *Hybrid Propulsion for Launch Vehicle Boosters: A Program Status Update*, 31st AIAA/ASME/SAE/ASEE Joint Propulsion Conference and Exhibit, San Diego CA, July 10-12, 1995.

[40] Arves, J., Gnau, M., Joiner, K., Kearney, D., McNeal, C., and Murbach, M.: *Overview of the Hybrid Sounding Rocket (HYSR) Project*, AIAA 2003-5199 , 2003.

[41] Austin, B. L. Jr., Heister, S. D., Dambach, E. M., Meyer, S. E., Wernimont, E. J., Variable Thrust: *Multiple Start Hybrid Motor Solutions for Missile and Space Applications*, 46th AIAA/ASME/SAE/ASEE Joint Propulsion Conference and Exhibit, 25-28 July 2010, Nashville, Tennessee.

[42] Peterson, Z. W.: *Closed-Loop Thrust and Pressure Profile Throttling of a Nitrous Oxide/Hydroxyl-Terminated Polybutadiene Hybrid Rocket Motor*, Mester Thesis, Utah State University, Department of Aerospace Engineering, 2012.

[43] Karabeyoglu, M., A., Cantwell, B., Stevens, J.: *Evaluation of Homologous Series of Normal-Alkanes as Hybrid Rocket Fuels*, 41st AIAA/ASME/SAE/ASEE Joint Propulsion Conference and Exhibit, 10-13 July 2005, Tucson, Arizona

[44] Barato, F., Bellomo, N., Lazzarin, M., Moretto, F., Bettella, A., Pavarin, D.: *Numerical Modeling of Paraffin-Based Fuels Behavior*, 48th AIAA/ASME/SAE/ASEE Joint Propulsion Conference and Exhibit, 29 July-01 August 2012, Atlanta, Georgia.

[45] National Institute of Standards and Technology, US Department of Commerce: *NIST Chemistry WebBook*, webbook.nist.gov/chemistry, 2011.

[46] Lazzarin, M., Faenza, M., Barato, F., Bellomo, N., Bettella, A., Pavarin, D., Grosse, M.: *CFD Simulation of a Hybrid Rocket Motor with Liquid Injection*, 47th AIAA/ASME/SAE/ASEE Joint Propulsion Conference and Exhibit, 01-03 August 2011, San Diego, California.

[47] Karabeyoglu, M. A.: *Transient Combustion in Hybrid Rockets*, PhD dissertation, Stanford University, Dept. of Aeronautics and Astronautics, Stanford, CA, Aug. 1998.

[48] Bellomo, N., Barato, F., Faenza, M., Lazzarin, M., Bettella, A., and Pavarin, D.: *Numerical and Experimental Investigation of Unidirectional Vortex Injection in Hybrid Rocket Engines*, Journal of Propulsion and Power, Vol. 29, No. 5 (2013), pp. 1097-1113.

[49] Bellomo, N.,: *Analysis of Variable Thrust Hybrid Propulsion for Formation Flight Satellites*, PhD dissertation, Padova University, Center of Studies and Activities for Space (CISAS), Padova, Italy, 2012.

[50] Lazzarin, M., Bellomo, N., Faenza, M., Barato, F., Rondini, D., et al.: *Numerical Investigation of Hybrid Motors for the EU FP7 SPARTAN Program*, 48th AIAA/ASME/SAE/ASEE Joint Propulsion Conference and Exhibit, 29 July-01 August 2012, Atlanta, Georgia.

[51] Knuth, W. H., Chiaverini, M. J., Sauer, J. A., and Gramer, D. J.: *Solid-Fuel Regression Rate Behavior of Vortex Hybrid Rocket Engines*, Journal of Propulsion and Power, Vol. 18, No. 3, 2002, pp. 600-609.

[52] Karabeyoglu, M. A., Cantwell, B. J., Zilliac, G.: *Development of Scalable Space-Time Averaged Regression Rate Expressions for Hybrid Rockets*, 41st AIAA/ASME/SAE/ASEE Joint Propulsion Conference and Exhibit, 10-13 July 2005, Tucson, Arizona.

[53] Chiaverini, M. J., Serin, N., Johnson, D. K., Lu, Y., Kuo, K. K., Risha, G. A.: *Regression Rate Behavior of Hybrid Rocket Solid Fuels*, Journal of Propulsion and Power, Vol. 16, No. 1, January-February 2000.

[54] Cai, G., Zeng, P., Li, X., Tian, H., Yu, N.: *Scale Effect of Fuel Regression Rate in Hybrid Rocket Motor*, Aerospace Science and Technology, Vol. 24, Issue 1, Pages 141-146, Elsevier, January-February 2013.

[55] Lazzarin, M., Barato, F.: *CFD Simulation of Regression Rate in Hybrid Rockets*, AAAF-ESA-CNES Space Propulsion 2012, 7-10 May 2012, Bordeaux, France.

[56] Carmicino, C., Russo Sorge, A.: *Role of Injection in Hybrid Rockets Regression Rate*, Journal of Propulsion and Power, Vol. 21, No. 4, AIAA, July-August 2005.

[57] Carmicino, C., Russo Sorge, A.: *Influence of a Conical Axial Injector on Hybrid Rocket Performance*, Journal of Propulsion and Power, Vol. 22, No. 5, AIAA, September-October 2006.

[58] Schumb, W. C., Satterfield, C. N., Wntworth, R. L.: *Hydrogen Peroxide*, Reinhold Publishing Corporation, 1955.

[59] Zilliac, G., Karabeyoglu, M. A.: *Hybrid Rocket Fuel Regression Rate Data and Modeling*, 42nd AIAA/ASME/SAE/ASEE Joint Propulsion Conference and Exhibit, 2006, Sacramento, California.

[60] Personal communications between UPD researchers and Jan-Erik Ronningen from NAMMO Raufoss AS.

[61] Ghassemi,H., Fasih, H. F.: *Application of small size cavitating venturi as flow controller and flow meter*, Flow Measurement and Instrumentation, Volume 22, Issue 5, October 2011, Pages 406-412, Elsevier.

[62] Majumdar, A.: *Numerical Modeling of Cavitating Venturi - a Flow Control Element of Propulsion System*, thermal & Fluid Analysis Workshop 2002, Univeristy of Houston Clear Lake Campus, Houston (TX).

[63] Carmicino, C.: *Alcuni Aspetti della Balistica Interna di un Endoreattore a Propellenti Ibridi e del Comportamento di Ugelli a Spina Troncata*, PhD Thesis, Aerospace Engineering, University of Napoli, 2002.

[64] Altman, D., Humble, R.: *Space Propulsion Analysis and Design*, McGraw-Hill, 1995.

[65] Bonacina, C., Cavallini, A., Mattarolo, L.: *Trasmissione del Calore*, ed. Cleup, Padova, 1992.

[66] Zellnik, H., Churchill, S. W.: *Convective Heat Transfer from High-temperature Air Inside a Tube*, A.I.Ch.E. Journal, Vol. 4, No. 1, pages 37-42, 1958.

[67] MatWeb, Material Property Data: *www.matweb.com.*

[68] Doebelin, E. O.: *Measurement Systems Application and Design* , ed. 6.1, McGraw-Hill, 1989.

[69] *Evaluation of Measurement Data - Guide to the Expression of Uncertainty in Measurement*, International Organization for Standardization (ISO), 1995.

[70] Kline, S. J., McClintock, F. A.: *Describing Uncertainties in Single-Sample Experiments*, Mechanical Engineering, Vol. 75, Jan. 1953.

[71] Ferrante, I.: *Incertezze delle Misure Fisiche*, lectures from Physics Laboratory class, Department of Physics, University of Pisa, 2013.

[72] *Water, Density and Specific Weight*, Engineeringtoolbox.com, 2011.

[73] Cavallini, A., Mattarolo, L.: *Termodinamica Applicata*, ed. cleup, 1992.

[74] Zarko, V., Kuo, K. K.: *Critical Review of Methods for Regression Rate Measurements of Condensed Phase Systems*, International Journal of Energetic Materials and Chemical Propulsion, Volume 3, Issue 1-6, 1994.

[75] N. Bellomo, M. Lazzarin, F. Barato, and M. Grosse: *Numerical investigation of the effect of a diaphragm on the performance of a hybrid rocket motor*, 46th AIAA/ASME/SAE/ASEE Joint Propulsion Conference, 25-28 July 2010, Nashville, Tennessee.

[76] TC Misure e Controlli s.r.l.: *Compendio di Termometria, Termocoppie e Termoresistenze*, 4th ed., TC Misure e Controlli s.r.l., Torino.

Acknowledgments

Ringrazio Daniele per essere un capo che si pone alla pari, con cui si può scherzare. Di lui continuo ad apprezzare la mente brillante e l'entusiasmo per le sfide impossibili.

Ringrazio Fede, perché a lui devo molto di quello che so ed è sicuramente anche merito suo se assomiglio di più a un Ingegnere. Ma lo ringrazio prima di tutto per essere stato un vero amico.

Ringrazio Cesco, per essere l'esperto scientifico che ha sempre la risposta giusta per risolvere ogni dubbio.

Ringrazio Nic di essere un precisino.

Ringrazio Marta, che insieme a me porta avanti la causa femminista nel laboratorio di propulsione del CISAS.

Ringrazio poi tutti gli altri colleghi: Marco e Bros in primis, Frasso, Frenky, Fabio, Davide, Albe, Sgara, Scapin e Selmo. Ognuno di loro ha contribuito a rendere le giornate di lavoro spensierate.

Infine mi permetto un ringraziamento non professionale, ma preziosissimo. Ringrazio la mia famiglia e Andrea, per avermi dato fiducia e sostegno. La loro presenza ha reso tutto meno difficile.